WESTERN UNIVERSITY
caspian

e-ISSN 3105-4293
p-ISSN 3105-4285

Journal of Nanotechnology and Innovative Materials

Vol2, №2, 2026



Baku - 2026

Western Caspian University

e-ISSN 3105-4293
p-ISSN 3105-4285

Journal of Nanotechnology and Innovative Materials

Vol 2, No 2, 2026

DOI:10.54414/VWTT8467

© Western Caspian University, 2026

https://jnim.wcu.edu.az/

Editor-in-Chief:

Prof. Dr. Hussein Baghirov

Western Caspian University, Azerbaijan

Scopus Link Scholar Link

Associate Editors:

Dr. Shirong Huang

Technische Universität Dresden, Germany

Scopus Link Scholar Link

Assoc. Prof. Baseem Khan

Center for Research on Microgrids, Huanjiang Laboratory, China

Scopus Link Scholar Link

Editorial Board

Prof. Dr. Jakub D. Rybka

Adam Mickiewicz University, Poland

Scopus Link Scholar Link

Prof. Dr. Ma Jianguo

East China University of Technology, China

Scopus Link

Prof. Dr. Ferhan Tumer

Kyrgyz-Turkish Manas University, Kyrgyzstan

Scopus Link Scholar Link

Prof. Dr. Subash Gopinath

Universiti Malaysia Perlis, Malaysia

Scopus Link Scholar Link

Prof. Dr. Adil M. Allahverdiyev

Scientific Research Institute of Medical Prevention named after V. Akhundov, Azerbaijan

Scopus Link Scholar Link

Prof. Dr. Shengliang Zhong

Jiangxi Normal University, China

Scopus Link

Prof. Dr. Yusif Aliyev

Azerbaijan State Pedagogical University, Azerbaijan

Scopus Link Scholar Link

Assoc. Prof. Ümit Ağbulut

Yildiz Technical University, Turkiye

Scopus Link Scholar Link

Assoc. Prof. Carlos Cava

Federal University of Technology Parana, Brazil

Scopus Link Scholar Link

Assoc. Prof. Emrah Madenci

Necmettin Erbakan University, Turkiye

Scopus Link Scholar Link

Assoc. Prof. Ruslan V. Kryvobok

National Technical University "Kharkiv Polytechnic Institute", Ukraine

Scopus Link Scholar Link

Assoc. Prof. Deepthi Jayan K.

Rajagiri School of Engineering & Technology, India

Scopus Link Scholar Link

Assoc. Prof. Yasin Onuralp Özkılıç

Necmettin Erbakan University, Turkiye

Scopus Link Scholar Link

Assoc. Prof. M.I. Sayyed

Isra University Amman, Jordan

Scopus Link Scholar Link

Assoc. Prof. Saltanat Aghayeva

Western Caspian University, Azerbaijan

Scopus Link Scholar Link

Assoc. Prof. Ghodrat Mahmoudi

University of Maragheh, Iran

Scopus Link Scholar Link

Assist. Prof. Lekshmi M.S.

Rajagiri School of Engineering & Technology, India

Scopus Link Scholar Link

Dr. Buhari Dogan

INTI International University, Malaysia

Scopus Link Scholar Link

Dr. Depeng Qiu

Jiangxi Academy of Science, China

Scopus Link Scholar Link

Dr. Rashid Iqbal

The Islamia University of Bahawalpur, Pakistan

Scopus Link Scholar Link

Dr. Faisal Mukhtar

Universiti Sains Malaysia, Malaysia

Scopus Link Scholar Link

Dr. Abhinav Kumar

Ural Federal University, Russia

Scopus Link

Dr. Ramiz Huseynov

Institute of Physics, Ministry of Science and Education, Azerbaijan

Scopus Link Scholar Link

Dr. Durdana Rustamova

Western Caspian University, Azerbaijan

Scopus Link Scholar Link

Dr. Naila Guliyeva

Western Caspian University, Azerbaijan

Scopus Link Scholar Link

CONTENTS

Nanoparticle-Based Adsorbents for the Removal of Heavy Metals and Organic Pollutants: Recent Advances and Future Prospects
Khadija-Tul-Kubra, Fiza Saleem, Shafaqat Ali, and Rashid Iqbal 6

Structural phase transitions and control of superionic transport in copper and silver chalcogenides
Yusif. I. Aliyev, O. R. Babayeva[1], and S. R. Azimova 19

Dependence of electrical resistance of polypropylene–mineral filler composites on temperature and ionizing radiation
Durdana F. Rustamova, Sayyara A. Nabieva, and Medine F. Nabili 28

Nanoengineered Material Architecture for Improved Durability and Sealing of Bidirectional Two-Way Ball Valves in Waxy Particle-Laden Oil Pipelines
Tatyana Huseynova 36

Conceptual Architecture of a Multi-Sensor Real-Time Monitoring System for Biomechanical Analysis of Intramuscular Injections
Elnare F. Firdus and Atakishi T. Tarlan 49

Investigation of the Thermal and Dielectric Properties of $MnFe_2O_4$ Nanoparticles
Aynure F. Gochuyeva 59

https://doi.org/10.54414/KNZF5082

Journal of Nanotechnology and Innovative Materials

Research Article

Nanoparticle-Based Adsorbents for the Removal of Heavy Metals and Organic Pollutants: Recent Advances and Future Prospects

Khadija-Tul-Kubra[1], Fiza Saleem[1], Shafaqat Ali[1]*, and Rashid Iqbal[2, 3]

[1]Department of Environmental Sciences, Government College University, Faisalabad 38000, Pakistan.
[2]Department of Agronomy, Faculty of Agriculture and Environment, The Islamia University of Bahawalpur, Bahawalpur 63100, Pakistan.
[3]Department of Life Sciences, Western Caspian University, Baku, Azerbaijan.

Received: 22.07.2026 Accepted: 31.08.2026 Published: 12.10.2026
https://doi.org/10.54414/UHWF6122

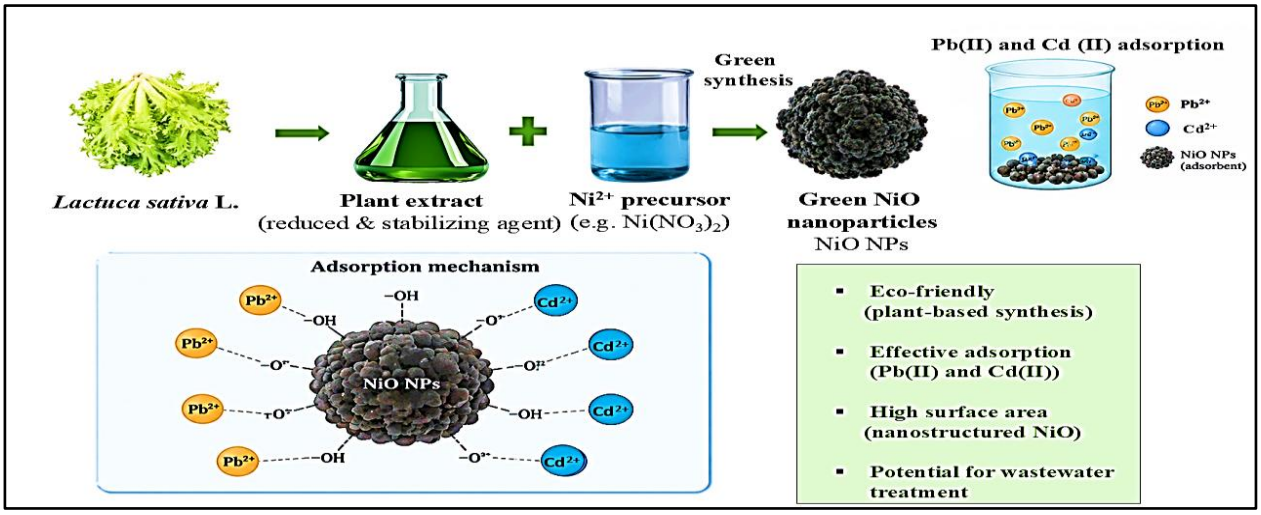
Copyright: © 2026 by the authors. Licensee: Journal of Nanotechnology and Innovative Materials, Western Caspian University, Baku, Azerbaijan. This article is an open-access article distributed under the terms and conditions of the Creative Commons Attribution 4.0 International License (CC BY 4.0).

Abstract

The growing emissions of heavy metals and organic contaminants from industries, agriculture, mining, and households have presented great challenges for water and wastewater treatment. The use of adsorbents based on nanoparticles has become attractive compared with traditional adsorbents owing to their large surface area, variable surface chemistry, numerous active sites, and feasibility of magnetic separation. This review article critically evaluates recent developments in metal oxide nanoparticles, carbonaceous nanomaterials, magnetic nanoparticles, and nanocomposites in the adsorption of heavy metals and organic contaminants from aqueous solutions. Some recent findings have shown high adsorption capacity with 897.0, 437.5, and 354.3 mg g^{-1} for Pb^{2+}, Cu^{2+}, and Cd^{2+}, respectivelyThe adsorption capacity of GO-ZrATMP was found to be 373, 320, and 281 mg g^{-1} for Pb^{2+}, Cd^{2+}, and Hg^{2+} ions, whereas that of modified graphene oxide was 370.0, 136.2, and 109.6 mg g^{-1} for Hg^{2+}, Cr (VI), and Pb^{2+} ions, respectively. In the case of organic pollutants, the adsorption capacities of IDA-GO@Fe_3O_4 were 437.10 mg g^{-1} for methylene blue, while those of MgFe-LDH·Fe_3O_4 and sugarcane-bagasse cellulose/GO were 153.2 and 143.29 mg g^{-1} for diclofenac and atrazine, respectively. Important mechanisms involved in adsorption include surface complexation, electrostatic interactions, ion exchange, chemisorption, and physisorption. Although laboratory efficiency is extremely high, issues like agglomeration, leaching, toxicity, regeneration, reproducibility, affordability, and scalability persist.

Keywords: Nanoadsorbents, Heavy metals, Organic pollutants, Nanocomposites, Wastewater treatment

Graphical Abstract



1. Introduction

Industrialization, urbanization, mining, agriculture, and chemical industries have resulted in increasing pollution with inorganic and organic pollutants, leading to ongoing water quality issues[1]. Inorganic pollutants, including Pb, Cd, Cr, Hg, As, Ni, Cu, and Zn, are major pollutants owing to their toxicity, persistence, resistance to degradation, and bioaccumulation [2]. Biodegradable pollutants are easily biodegradable, unlike heavy metals, which are not easily degraded by biological activities [3]. Polluted waters in the mining industry, metal industry, electroplating, and manufacturing contain multiple types of heavy metal ions[1]. Organic pollutants in industrial wastewater include dyes, drugs, pesticides, phenolic compounds, etc.[4].

These two together add complexities to the process of treatment as the chemicals vary in composition, charge, solubility, and attraction to treatment material [2]. Industrial wastewaters contain many synthetic dyes, which pose a risk to aquatic ecosystems due to their stability and resistance to biological treatment [5]. Thus, there is a need for treatment materials that can deal with various types of pollutants under complicated aqueous conditions [6].

Traditional approaches to wastewater treatment might be efficient in dealing with certain contaminants; however, their efficacy may be limited by complicated pollutant mixtures and low contaminant concentrations [6]. Adsorption technology has been attracting more interest because of its efficiency and universal applicability [2]. The efficiency of the adsorption process depends largely on the characteristics of the adsorbent material, such as its surface properties, functional groups, porosity, and active sites [6].

Adsorbents developed using nanoparticles have evolved as superior materials owing to the increased surface area offered by the tiny particles[5]. Metal oxides, zero-valent metals, carbon nanomaterials, graphene oxide materials, magnetic nanoparticles, MOFs, and nanocomposites have thus been explored for heavy metal removal and organic pollutants [2]. Surface functionalization can further increase the interaction between the pollutant and adsorbent, increasing selectivity and adsorption efficiency[7]while magnetic nanocomposites make adsorbent separation easy after treatment[8].

Nanocomposites can utilize the properties of various materials, which enhances their surface function and pollutant removal capabilities [4]. Nonetheless, the problems of nanoparticle aggregation, difficulty in recovery, leaching, regeneration, and environmental safety continue to pose serious challenges (18). Therefore, future research on nanoadsorbents must consider their adsorption efficiency, as well as their regeneration, recyclability, stability, safety, and scalability[2]. This paper analyzes current trends in nanoparticle-based adsorbents that are used to remove heavy metals and organic contaminants from water and wastewater through metal oxides, magnetic nanoparticles, carbon-based materials, graphene-based materials, MOFs, and multifunctional nanocomposites[2].

Emphasis is made on adsorption processes such as electrostatic, ion exchange, surface complexation, chemisorption, physisorption, and functional group interactions [5]. Comparison of their efficiency is based on the type of pollutant, adsorption capacity, operation parameters, kinetics, isotherms, and regeneration ability [6]. Nanocomposite fabrication, stability, leaching, toxicity, regeneration, practical application in real wastewaters, economic viability, and scale-up aspects are further considered in this review [1], [8]. Finally, future research aspects are outlined in terms of sustainable synthesis, multifunctional nanoadsorbents, real wastewater applications, recyclability, and environmentally friendly nanomaterials [2].

2. Nanoparticle-Based Adsorbents

2.1 Metal Oxide Nanoparticles

Metal oxide nanoparticles offer great promise as adsorbents because the small size of these particles allows them to have highly reactive surfaces that enable high interaction with contaminants present in the solution [9]. MnO_2 nanoparticles present a good choice for removing metals because of their ability to interact effectively with dissolved metal ions even in acidic environments [10]. In a study carried out on acid mine drainage, ε-MnO_2 was found to adsorb 172.14 mg g^{-1} Pb^{2+} at pH 2 [10].

Moreover, the same investigation showed that Pb^{2+} adsorption was accomplished by ion-exchange reactions linked with the dissolution and surface complexation processes related to Mn^{2+}. It demonstrated how adsorption may include not only the surface reaction but also the dissolution process [10]. Another MnO_2-based material was synthesized through the synthesis of MnO_2 and Fe_3O_4 in alginate/carboxymethyl-cellulose beads, thus obtaining a magnetic adsorbent suitable for selective removal of Tl(I) ions [11]. These MnO_2-doped magnetic beads provided an adsorption capacity of 38.8 mg g^{-1} of Tl(I) ions and close to 100% removal efficiency of Tl(I) with high selectivity towards the competing ions [11]. Metal oxides can be combined with naturally available biomass to unite the nanoscale reactivity of metal oxides with the features of renewable matrices [12]. In particular, MnO_2-functionalized Salicornia europaea biomass proved its ability to have a breakthrough adsorption capacity of 251.16 mg g^{-1} for Pb^{2+} [12].

2.2 Carbon-Based Nanomaterials

There are a variety of carbon-based nanomaterials such as graphene oxide (GO), reduced graphene oxide (rGO), carbon nanotubes (CNTs), and carbon nanofibers (CNFs) that have been extensively studied as adsorbents due to their high specific surface area and modifiable surface properties [13]. The presence of oxygenated groups in graphene oxide creates active sites for interaction with metal ions and organic pollutants present in aqueous media. It was observed that graphene oxide nanosheets effectively removed pharmaceutical compounds from aqueous solutions [14]. The adsorption capacity of graphene-based nanomaterials can be improved through surface modification; violuric acid-functionalized reduced graphene oxide was highly effective in removing Hg^{2+}, Pb^{2+} , and As^{3+} [15].

Carbon nanotubes also offer additional adsorption sites on account of their graphitic surfaces, which may be oxidized chemically to create functional groups that improve binding interactions with metal ions. In a study carried out by Li et al. (2024), it was established that oxidized multiwalled carbon nanotubes offered improved adsorption of Pb(II) and Cd(II).

Carbon nanofibers may also be used as substrates for biological and chemical functionalization; this is evidenced in a study where an Enterococcus faecalis/CNF composite was able to attain an adsorption capacity of 255 mg g^{-1} for As (III) [16].

2.3 Magnetic Nanoparticles

Magnetic nanoparticles such as those based on Fe_3O_4 are promising adsorbents because the magnetic separation technique enables the separation of the adsorbent from the treated wastewater without traditional filtration or centrifugation [17]. The surface modification of magnetic nanoparticles can increase the affinity towards the targeted contaminant; for instance, the functionalization of Fe_3O_4-based nanomaterials resulted in the efficient removal of heavy metals via the interaction with surface functional groups [17]. The magnetic adsorbents may be coupled with carbonaceous material to merge the high capacity of carbon with the convenience of magnetic separation. The magnetic carbon nanocomposite synthesized from carbon obtained from biomass had a high efficiency in the removal of Pb, Cu, and Cr (VI) ions and could retain its performance

even after multiple reuse [18]. Moreover, magnetic carbon was examined for the removal of pharmaceutical waste, and the synthesis of magnetic iron oxide nanoparticles in the activated carbon allowed adsorption and magnetic separation/regeneration of the adsorbate [19].

2.4 Nanocomposites

Nanocomposites involve the combination of two or more materials to achieve complementary physicochemical property in a bid to overcome the challenges related to individual nanoadsorbents [20]. The use of Fe_3O_4/graphene oxide/chitosan nanocomposites that combine the adsorption properties of GO and chitosan together with the magnetic separation properties of Fe_3O_4 resulted in a maximum Pb(II) adsorption capacity of 63.45 mg g^{-1} [17]. Other nanocomposites that have been used for the simultaneous removal of Ni^{2+} and Cd^{2+} ions using GO-CuO nanocomposites achieved removal efficiencies of approximately 89.6% and 97.1%, respectively (Table 1), when the system was optimized through batch experiments. A tertiary magnetic nanocomposite of GO that contains chitosan or polyaniline has also been used for the simultaneous adsorption of Cr(VI) and Pb(II) ions, where the polyaniline-based nanocomposite was able to achieve adsorption capacities of 111.7 mg g^{-1} for Cr(VI) and 118.44 mg g^{-1} for Pb(II) [18]. Hydrogel beads composed of graphene oxide, magnetic iron oxide (Fe_3O_4), MOFs, and alginate have been developed to achieve the removal of various pharmaceutical contaminants along with magnetic separation and regeneration [21].

Table 1. Representative nanoadsorbents for heavy-metal removal and their adsorption performance.

Nanoadsorbent category	Materials	Functional feature	Target pollutant(s)	Applications	Main advantage	Reference
Metal oxide	Hollow mesoporous MnO_2	Hollow mesoporous structure with abundant adsorption sites	Pb^{2+}, Cu^{2+}, Cd^{2+}	qmax = 897.0, 437.5 and 354.3 mg g^{-1} for Pb, Cu and Cd, respectively	High heavy-metal uptake and structural stability	[9]
Metal oxide	Green Fe_3O_4/iron oxide NPs	Plant-mediated synthesis; magnetic iron-oxide surface	Cd^{2+}, Ni^{2+}	Cd^{2+}: 78 and 74 mg g^{-1}; Ni^{2+}: 64.8 and 80 mg g^{-1} for the two plant-derived materials	Green synthesis and magnetic recovery potential	[22]
Metal oxide	Green NiO NPs	Plant-extract-mediated NiO synthesis	Pb^{2+}	99.99% removal under optimized conditions; qmax = 60.13 mg g^{-1}	High Pb removal and green preparation	[23]
Magnetic nanomaterial	$CoFe_2O_4$@SiO_2 –NH_2	Magnetic ferrite core with silica and amino functionalization	Pb^{2+}, Cu^{2+}, Zn^{2+}	qmax = 254.453, 277.008 and 258.398 mg g^{-1} for Pb, Cu and Zn	Magnetic separation plus amino-metal coordination	[24]
Carbon-based nanomaterial	GO–Zr–ATMP composite	GO surface modified with Zr and phosphonate groups	Pb^{2+}, Cd^{2+}, Hg^{2+}	qmax = 373, 320 and 281 mg g^{-1}, respectively	High capacity and simultaneous multi-metal separation	[25]
Chitosan-based magnetic nanocomposite	TPP-CMN	Fe_3O_4 coated with chitosan and modified with TPP	Cd^{2+}, Co^{2+}, Cu^{2+}, Pb^{2+}	qmax = 91.75, 93.00, 87.25 and 99.96 mg g^{-1}, respectively	Magnetic recovery and surface functionalizatio n	[26]
Chitosan-based magnetic nanocomposite	V-CMN	Chitosan/Fe_3O_4 modified with vanillin	Cd^{2+}, Co^{2+}, Cu^{2+}, Pb^{2+}	qmax = 92.5, 94.0, 88.75 and 99.89 mg g^{-1}, respectively	Magnetic separation and chemical modification	[26]

Nanoadsorbent category	Materials	Functional feature	Target pollutant(s)	Applications	Main advantage	Reference
Hybrid ion-exchange nanoadsorbent	HFO-embedded ion-exchange resin	Hydrous ferric oxide nanoparticles embedded within ion-exchange resin	Cr(VI), Cd^{2+}, Pb^{2+}	Applied to acidic mine-drainage-related metal removal	Combines nanoparticle adsorption with ion exchange	[27]

3. Synthesis and Characterization

3.1 Conventional and Green Synthesis

Conventional approaches for synthesizing nanoparticles include co-precipitation, sol-gel, hydrothermal, and chemical reduction approaches. They provide excellent control over the size, shape, and composition of nanoparticles [28]. The co-precipitation method is commonly used to synthesize magnetic iron oxide-based nanoadsorbents. Co-precipitation is achieved by the precipitation of metal ions under alkaline conditions [28]. The sol-gel process allows for a controlled synthesis of the metal-oxide networks via hydrolysis and condensation reactions. The sol-gel process can yield homogeneous and crystalline nanoparticles upon heating [29]. In the hydrothermal synthesis approach, high temperature and pressure are employed to enhance the crystallinity and morphology of nanoparticles. This approach is ideal for synthesizing metal oxides with high structural integrity [30]. However, conventional synthesis approaches can be limited by toxic reagents and high energy requirements. This has stimulated research into environmentally friendly approaches to nanoparticle synthesis [31].

Green synthesis makes use of plant extracts, algae, microorganisms, or compounds derived from biomass as the reducing and stabilizing agents. This process will be able to minimize the use of dangerous chemicals while fabricating the nanoparticles [32]. Plant extracts consist of polyphenols, flavonoids, proteins, and various phytochemicals that can play a part in nanoparticle fabrication. In addition, they may act as capping agents on the surfaces of nanoparticles [33]. For instance, Prosopis farcta extract was used to fabricate Fe_3O_4 nanoparticles for methylene blue adsorption. The nanoparticles were fabricated in a plant-mediated process and exhibited good dye-removal capability [33]. Furthermore, green synthesis is applicable in the case of ZnO nanoparticles using the Nauclea latifolia fruit extract. The nanoparticles exhibited a crystalline size around 14.4 nm and significant methyl green removal capability [34]. Agricultural wastes can serve as another sustainable source of nanoparticle production. As an example, palm-petiole extract was employed in zero-valent iron nanoparticle fabrication for Cr(VI) removal [35]. Hence, green synthesis could be used to cut down chemical consumption by transforming natural biological materials into nanoadsorbent materials. But reproducibility and scalability still remain issues [36].

3.2 Physicochemical Characterization

The physicochemical characterization provides information on structure, morphology, surface chemistry, and stability of the synthesized nanoadsorbents. Several techniques are needed [37]. X-ray diffraction (XRD) shows the crystalline phases and provides information on the crystallite size. It is used to confirm the synthesis of nanoparticles [34]. Fourier-transform infrared spectroscopy (FTIR) helps to identify the surface functional groups. Any change in FTIR bands after adsorption might point to the participation of certain groups in the pollutant adsorption [38]. Scanning electron microscopy (SEM) gives information on the surface morphology and agglomeration. Transmission electron microscopy (TEM) gives more detailed information on the size and shape of particles [33]. Energy-dispersive X-ray spectroscopy (EDS) shows the chemical composition of the nanomaterials. It confirms the presence of certain elements in the synthesized nanocomposites [38]. Brunauer–Emmett–Teller (BET) gives the values of the specific surface area and pore characteristics. A greater accessible surface area might give additional adsorption sites for pollutants [34].

The determination of the zeta potential allows one to determine the electrical charge of the surfaces and helps elucidate the electrostatic forces between adsorbates and adsorbents [37]. Vibrating sample magnetometry (VSM) is necessary for magnetic nanoadsorbents. This technique determines the magnetic properties of nanoadsorbents and assesses magnetic separation after purification (3). The determination of optical properties and formation of nanoparticles can be performed using UV–Visible spectroscopy. This

method is also helpful for assessing the concentration dependence of some nanomaterials [29]. The thermal analysis gives information about the stability and decomposition of organic compounds in nanocomposites, which is needed when polymeric or biomass materials are introduced in nanoadsorbents [36]. Overall, the methods of XRD, FTIR, SEM/TEM, EDS, BET, zeta-potential, and magnetic properties give a complete description of the properties of nanoadsorbents and their relation to the material properties and adsorption efficiency [39].

4. Adsorption Mechanisms

4.1 Surface Complexation

Surface complexation happens through the reaction of pollutants with reactive sites on the surface of an adsorbent [40]. The surfaces of metal oxides can offer hydroxyl groups to interact with metal ions in solution [41]. Such interactions can result in either inner- or outer-sphere surface complexation [42]. Surface complexation is heavily influenced by the pH level because the process of protonation affects the sites on the surface [40]. The spectroscopic methods include XPS and X-ray adsorption spectroscopy [42].

4.2 Electrostatic Interaction

Attraction of oppositely charged pollutants and surfaces leads to electrostatic interaction [43]. It implies that positively charged ions can be attracted by the negatively charged adsorption surfaces [43]. Electrostatic interaction is especially relevant in cases of ionic pollutants since the charge of ionic pollutants is responsible for adsorption [44].

4.3 Ion Exchange

The ion exchange method comprises exchanging exchangeable ions in an adsorbent with pollutant ions in solution [27]. It ensures charge balance and transfers the desired ion into the adsorbent phase (68). This technique is significant in materials with exchangeable ions, both anions and cations, such as ion exchange resins and layered materials [27]. Ion exchange may take place at the same time as electrostatic interactions and surface complexation [46].

4.4 Chemisorption and Physisorption

Adsorption may take place by way of physical and chemical bonds formed between pollutants and adsorbent surfaces [47]. The process of physisorption usually takes place by means of weaker bonds like van der Waals interactions and hydrogen bonding [48]. In chemisorption, stronger bonds, which include chemical bonding, are involved [47]. Covalent bonding or ionic bonding can lead to chemisorption on functionalized nanomaterials [49]. Both mechanisms can occur simultaneously depending on surface chemistry and pollutant properties [50].

5. Heavy Metal Removal

5.1: Pb, Cd, Cr and Hg

Among the most concerning heavy metal pollutants in terms of toxicity and their bioaccumulation and environmental persistence include lead (Pb), cadmium (Cd), chromium (Cr), and mercury (Hg) [51]. The potential applications of nanoparticle-based adsorbents in treating such metals are very high due to the large surface area and numerous active sites on the surface, which allow interaction with metal ions [25]. Thus, the graphene oxide-zirconium hybrid composite demonstrated maximum adsorption of Pb(II), Cd(II), and Hg(II) of 373, 320, and 281 mg g^{-1}, correspondingly [25]. Likewise, chemically and green-synthesized zinc oxide nanoparticles proved to be highly effective in the removal of different metals from wastewater, both synthetic and industrial. Modified graphene oxide with amino, hydrazino, and thiol groups showed affinity to Hg(II), Cr(VI), and Pb(II), with the maximum adsorption of 370.0, 136.2, and 109.6 mg g^{-1}, correspondingly [19].

5.2 As, Ni, Cu and Zn

Another group of pollutants, such as arsenic (As), nickel (Ni), copper (Cu), and zinc (Zn), which are commonly found in industrial and polluted water, also needs to be efficiently removed due to their toxicity and possible impacts on the environment [52]. Magnetite-embedded graphene oxide obtained from spent batteries removed 98% of As(III) ions at pH 7 during 20 min, with a maximum adsorption capacity of 50.2 mg g^{-1} [53]. Mesoporous magnetic carbon composites containing La-Fe and Zr-Fe phases had the maximum adsorption

capacity for As(III) of 116.25 and 109.89 mg g^{-1} and for As(V) – 166.67 and 144.93 mg g^{-1}, respectively [54]. As for Ni and Zn ions, surface-modified natural zeolite showed highly improved uptake capacity, reaching removal of 86.67% and 88.49%, respectively, while Cu ions were removed with an efficiency of 99.96% in multielement solutions [55]. Moreover, sodium trititanate nanorods were effectively utilized for the removal of Cr(VI), Cu(II), and Ni(II) ions from real electroplating wastewater [56].

6. Organic Pollutant Removal

6.1 Dyes and Pharmaceuticals

Synthetic dyes are persistent contaminants of the wastewater streams due to their stability and resistance to conventional treatments. Nanocomposites based on magnetism allow for effective adsorption and easy separation following the treatment process [57]. In addition, carbon ferrite-based nanomaterials could be used for pharmaceutical residue removal due to surface interaction and magnetic recovery properties [58].

A composite of iminodiacetic acid-modified graphene oxide and Fe_3O_4 was synthesized by Abdolmaleki et al. (2024) for the removal of MB and MO. The highest adsorption capacities were found to be 437.10 mg g^{-1} and 165.65 mg g^{-1} for MB and MO, respectively. Electrostatic interaction, hydrogen bond formation, and π and π-π interactions played important roles in MB/MO adsorption. The MB adsorption capacity was maintained during five cycles. Moreover, Iuliano et al. (2024) have studied FLG/Fe_3O_4/Ag@PAA nanocomposite for MB removal from water solutions.

Pharmaceutical sorption has also benefited from hybrid magnetic nanoparticles. Mg,Fe-LDH·Fe_3O_4 nanocomposites attained the maximum sorption capacity of 153.2 and 143.2 mg g^{-1} at pH 7.5 for diclofenac. The FTIR and XRD findings showed that electrostatic and complex formation were the mechanisms of sorption [58]. In addition, a PANI/GO/MOF-Fe_3O_4 nanocomposite was designed to adsorb methyl orange and naproxen sodium simultaneously [59].

6.2 Pesticides and Emerging Pollutants

The pesticides may continue to exist in aquatic ecosystems due to their extensive use and stability [60]. Composites using graphene oxide offer functional surfaces for pesticide adsorption and can be fabricated from biomass in agriculture. Kuppusamy et al. (2024) have developed the sugarcane-bagasse-cellulose/graphene oxide nanocomposite for atrazine removal and found the highest adsorption capacity to be 143.29 mg g^{-1}. Clay composites modified with LDH have also been used in the removal of atrazine and 4-chloro-2-methylphenoxyacetic acid (MCP). The LDH@Mt composite has demonstrated adsorption capacities of 8.19 mg g^{-1} and 90.9 mg g^{-1} for atrazine and MCP, respectively [60].

Organic emerging contaminants include drugs, antibiotics, and other biologically active chemicals commonly found in water systems. These need the use of adsorbents that have appropriate surface chemistry and a sufficient number of interaction sites (Table 2). It was found that Mg, Fe-LDH·Fe_3O_4 nanocomposites had successful adsorption capacity of diclofenac to the extent of 153.2 and 143.2 mg g^{-1} at a pH of 7.5. The stability of these nanoparticles remained even after three regeneration cycles [58].

Table 2. Recent nanoparticles used as adsorbents for organic pollutants.

Pollutant	Nanoadsorbent	Removal performance	Reference
Methylene blue	IDA-GO@Fe_3O_4	437.10 mg g^{-1}	[57]
Methylene blue	FLG/Fe_3O_4/Ag@PAA	141.60 mg g^{-1}; 98%	[61]
Diclofenac	Mg, Fe-LDH·Fe_3O_4	153.2 mg g^{-1}	[58]
Atrazine	Sugarcane-bagasse cellulose/GO	143.29 mg g^{-1}	[62]
Atrazine + MCP	LDH-modified clay	Composite-dependent	[60]
Methyl orange	PANI/GO/MOF-Fe_3O_4	239.78 mg g^{-1}	[59]

Pollutant	Nanoadsorbent	Removal performance	Reference
Naproxen sodium	PANI/GO/MOF-Fe_3O_4	40.64 mg g^{-1}	[59]

7. Multifunctional Nanocomposites

7.1 Multi-Pollutant Removal

The presence of more than one pollutant in real wastewater samples is common; thus, the development of multifunctional nanocomposites that incorporate various removal mechanisms is being pursued. Wang et al. (2024b) prepared Fe_3O_4/P(NIPAM-co-MAA)/Ag–TiO_2 that can remove a mixture of basic fuchsin and ciprofloxacin. It adsorbed the organic dye and photodegraded the antibiotic ciprofloxacin using visible light. According to Chandra et al. (2023), chitosan-based magnetic nano-sorbents were found to be capable of removing Cd, Co, Cu, and Pb ions from industrial wastewater. Hybrid materials also help in achieving selectivity in metal ion removal. For instance, GO-ZrATMP displayed maximum adsorption capacities for Pb^{2+}, Cd^{2+}, and Hg^{2+} as 373, 320, and 281 mg g^{-1}, respectively. This material was also examined in real wastewater [25].

HFO-containing ion exchange resins were developed for Cr(VI), Cd(II), and Pb(II) remediation and performed well both in simulated and natural acid mine drainage [27]

7.2 Applications to Real Wastewater Samples

Lab solutions yield valuable information about sorbents' performance, yet may not always be reflective of real wastewater characteristics. Thus, Chandra et al. (2023) tested magnetic chitosan nano-sorbents in real wastewater samples collected from textile-dyeing and footwear factories. The sorbents exhibited good contaminant removal capacity despite being subjected to untreated wastewater. GO-ZrATMP was tested on real wastewater samples as well and proved to have good prospects for heavy metal elimination [25].

In real wastewater samples, there may be other ions and organic substances that hinder the adsorption process. Therefore, future research efforts should concentrate more on the complex composition of wastewater instead of synthetic solutions. Multifunctional Fe_3O_4/P(NIPAM-co-MAA)/Ag-TiO_2 nanocomposites illustrate the approach to combine adsorption and photocatalysis processes in mixed contamination conditions [63]. Furthermore, magnetic separation could make nanocomposite collection much easier [58].

8. Regeneration and Environmental Safety

8.1 Regeneration and Reusability

Regeneration is vital for minimizing the amount of adsorbent needed and minimizing costs. Chitosan nano-adsorbents with magnetic properties preserved more than 75% of their adsorption efficiency after four cycles of recycling for different heavy metals [26]. Similarly, green-synthesized NiO nanoparticles preserved Pb^{2+} removal efficiency up to five times, which is another piece of evidence of reusability [64].

The other advantage of using magnetic nanocomposites is that they can easily be separated with the help of an external magnetic field. Mg, Fe-LDH·Fe_3O_4 preserved its structure and magnetic efficiency after three cycles of regeneration [58]. Likewise, HFO-based hybrid ion-exchange resins can also be regenerated with the help of NaCl to recover Cd and Pb [65].

8.2 Leaching and Toxicity

Environmental safety of the nanoparticles should be assessed before their wide use. Metal ions can be released from nanocomposites during treatment and regeneration processes. Therefore, HFO hybrid resin systems were examined for possible metal release and regeneration characteristics during wastewater treatment [16]. Additionally, the potential metal release of magnetic LDH/Fe3O4 during pharmaceutical adsorption was studied [58].

9. Challenges and Future Prospects

9.1 Scale-up and Sustainability

Despite excellent laboratory results, scale-up of nanoadsorbents faces difficulties. Expensive synthesis, aggregation, regeneration problems, and separation may prevent practical application. Current literature points to the fact that new adsorbents have to be studied for their economic and ecological viability and not only for their adsorption ability (54). The use of green synthesis involving biomass extracts and waste materials can lower the use of chemicals and make this technology sustainable. One example of this synthesis method is green NiO synthesis with the use of Lactuca sativa [23].

Tests in real wastewater should become the norm of nanoadsorbent investigation. A complex matrix can affect the adsorption process due to competitive adsorption or changes in pH or ionic strength. Application of chitosan-based magnetic nanoadsorbents has already been demonstrated in the case of real wastewater of textile and footwear industries [26]. Real wastewater tests were also successfully performed in the case of GO-ZrATMP [25].

9.2 AI-Assisted Design and Future Directions

AI and machine learning algorithms have the potential to optimize the design of new adsorbents. These techniques help connect material characteristics and operation parameters with adsorption performance. New studies indicate that AI-assisted material design is one of the trends in adsorption technologies for wastewater purification [64].

Nanoadsorbents of the future must have high capacity, selectivity, magnetic separation, and regeneration abilities. Nanomaterials might also be designed to perform adsorption and photocatalytic degradation processes at once. The Fe_3O_4/P(NIPAM-co-MAA)/Ag-TiO_2 composite shows this approach through its dye adsorption and antibiotic photodegradation capabilities [63].

10. Conclusion

Adsorbents based on nanoparticles have proved themselves to be efficient materials for the treatment of various heavy metals and organic pollutants present in polluted water. High surface area, adjustable surface chemistry, and numerous active sites can be helpful for the better adsorption of pollutants in comparison with some conventional adsorbents. Modern research proves the viability of metal oxides, carbon-based nanomaterials, magnetic nanoparticles, and multifunctional nanocomposites for the purification of Pb, Cd, Cr, Hg, As, Ni, Cu, Zn, dyes, drugs, and pesticides.

The adsorption efficiency is greatly influenced by the surface characteristics and features of pollutants. Such mechanisms as surface complexation, electrostatic interactions, ion exchange, chemisorption, and physical adsorption can function independently or jointly. The functionalization increases the number of active sites and their selectivity, whereas the presence of magnetic components helps in the recovery of the adsorbents.

Green synthesis offers a way forward to more sustainable manufacture of nanoadsorbents. Plant extracts, biomass, and other renewable sources will ensure lower usage of toxic materials as well as help achieve valorization of waste. Nonetheless, reproducibility, stability of particles, aggregation, and scale-up still pose certain challenges. Hence, future studies should focus on the evaluation of not only adsorption capacities but also regeneration efficiencies, material stability, nanoparticle leaching, toxicity, and lifecycle impacts.

Validation on real wastewater is especially crucial because of the presence of competing ions, organic substances, variable pH values, and pollutant mixtures that may affect adsorption efficiency. That is why researchers should pay much attention to continuous systems, industrial effluents, repeated regeneration, and long-term operation. Economic evaluation is equally crucial for determining the practical application of advanced nanoadsorbents

Nanoadsorbents for future research should be designed as multifunctional, recyclable, and environmentally friendly materials that can purify water from multiple impurities. Adsorption combined with photocatalysis, magnetization, eco-friendly methods of material fabrication, and computer-aided materials design may increase the efficiency of the process. Artificial intelligence and machine learning technologies can assist in

predicting the performance of the adsorption process and optimizing the material properties and operational parameters. Thus, nanoadsorbents seem to be a promising technology for wastewater purification. However, further successful implementation will require balancing several aspects.

Conflict of Interest

The authors declare that they have no conflict of interest.

Author Contributions

Khadija-Tul-Kubra, Conceptualization, literature search, data collection and analysis, manuscript drafting, and visualization. Fiza Saleem, Literature analysis, manuscript review, and writing review and editing. Shafaqat Ali and Rashid Iqbal, supervision, critical evaluation, and writing review and editing.

Data Availability

No new data were generated or analyzed in this review article. All information discussed in this article was obtained from previously published literature.

AI-assisted writing

AI-assisted tools were used during the preparation of this manuscript for limited language editing and improvement of clarity. The authors reviewed, verified, and approved all content and remain responsible for the accuracy and integrity of the manuscript.

References

[1] Feisal NA, Kamaludin NH, Ahmad MA, Ibrahim TN. A comprehensive review of nanomaterials for efficient heavy metal ions removal in water treatment. Journal of Water Process Engineering. 2024 Jul 1;64:105566.

[2] Al-Amrani WA, Onaizi SA. Adsorptive removal of heavy metals from wastewater using emerging nanostructured materials: A state-of-the-art review. Separation and Purification Technology. 2024 Sep 6;343:127018.

[3] Sheraz N, Shah A, Haleem A, Iftikhar FJ. Comprehensive assessment of carbon-, biomaterial-and inorganic-based adsorbents for the removal of the most hazardous heavy metal ions from wastewater. RSC advances. 2024 Apr 9;14(16):11284-310.

[4] Mehta P, Chelike DK, Rathore RK. Adsorption-based approaches for exploring nanoparticle effectiveness in wastewater treatment. ChemistrySelect. 2024 Jul 3;9(25):e202400959.

[5] Karnwal A, Malik T. Nano-revolution in heavy metal removal: engineered nanomaterials for cleaner water. Frontiers in Environmental Science. 2024 May 6;12:1393694.

[6] Ismail UM, Vohra MS, Onaizi SA. Adsorptive removal of heavy metals from aqueous solutions: Progress of adsorbents development and their effectiveness. Environmental Research. 2024 Jun 15;251:118562.

[7] Siddeeg SM, Tahoon MA, Alsaiari NS, Shabbir M, Rebah FB. Application of functionalized nanomaterials as effective adsorbents for the removal of heavy metals from wastewater: a review. Current Analytical Chemistry. 2021 Jan 1;17(1):4-22.

[8] Youssif MM, El-Attar HG, Hessel V, Wojnicki M. Recent developments in the adsorption of heavy metal ions from aqueous solutions using various nanomaterials. Materials. 2024 Oct 22;17(21):5141.

[9] Zhang H, Zhang Y, Pan Y, Wang F, Sun Y, Wang S, Wang Z, Wu A, Zhang Y. Efficient removal of heavy metal ions from wastewater and fixation of heavy metals in soil by manganese dioxide nanosorbents with tailored hollow mesoporous structure. Chemical Engineering Journal. 2023 Mar 1;459:141583.

[10] Yang Y, Wang Y, Xue C, Lin Y, Lee JF, Yi X, Dang Z. Efficient removal of heavy metals from acid mine drainage by ε-MnO2 adsorption. Journal of Cleaner Production. 2024 May 1;452:141936.

[11] Gong D, Yang P, Zhao J, Jia X. Selective removal of thallium from water by MnO2-doped magnetic beads: performance and mechanism study. Journal of Environmental Management. 2024 Feb 27;353:120147.

[12] Akar T, Alim S, Meltem G, Sayin F, Akar ST. A novel sustainable and eco-friendly biosourced hybrid sorbent for toxic Pb2+ decontamination: Nano metal oxide functionalized salt-tolerant plant biomass. Journal of Cleaner Production. 2024 Feb 1;439:140838
[13] Li X, Cui Y, Du W, Cui W, Huo L, Liu H. Adsorption kinetics and mechanism of Pb (II) and Cd (II) adsorption in water through oxidized multiwalled carbon nanotubes. Applied Sciences. 2024 Feb 21;14(5):1745.
[14] Mkilima T, Jexembayeva A, Konkanov M, Bertleuova A, Tlegenov R, Maksat A, Mukyshev A, Zharkenov Y. Utilizing banana peel-derived graphene oxide nanosheets for adsorptive removal of pharmaceuticals from wastewater. Case Studies in Chemical and Environmental Engineering. 2024 Dec 1;10:100893.
[15] Kumar P, Das S. Efficient adsorption of toxic heavy metal ions on the surface engineered violuric acid-reduced graphene oxide nanomaterial. ACS Applied Engineering Materials. 2023 May 17;1(5):1343-55.
[16] Rind IK, Sarı A, Tuzen M, Lanjwani MF, Karaman I, Saleh TA. Bacteria immobilized onto carbon nanofiber as a composite for effective removal of arsenic from wastewater. Materials Science and Engineering: B. 2023 Nov 1;297:116809.
[17] Vo LQ, Vu AT, Le TD, Huynh CD, Tran HV. Fe3O4/graphene oxide/chitosan nanocomposite: a smart nanosorbent for lead (II) ion removal from contaminated water. ACS omega. 2024 Apr 3;9(15):17506
[18] Manzoor Q, Farrukh MA, Qamar MT, Sajid A, Aldossari SA, Manikandan A, Iqbal M. Polymer-assisted synthesis of ternary magnetic graphene oxide nanocomposite for the adsorptive removal of Cr (VI) and Pb (II) ions. Heliyon. 2024 Aug 15;10(15).
[19] Bakry AM, Alamier WM, Abdallah AB, El-Reash YG, El-Shall MS, Awad FS. Enhanced performance of amine and thiol chemically modified graphene oxide for effective removal of Hg (II), Pb (II), and Cr (VI) from aqueous solution. Applied Water Science. 2024 Aug;14(8):179.
[20] Mahar I, Mahar FK, Mahar N, Memon AA, Pirzado AA, Khatri Z, Thebo KH, Ali A. Fabrication and characterization of MXene/carbon composite-based nanofibers (MXene/CNFs) membrane: An efficient adsorbent material for removal of Pb+ 2 and As+ 3 ions from water. Chemical Engineering Research and Design. 2023 Mar 1;191:462-71
[21] Karimi S, Namazi H. Efficient adsorptive removal of used drugs during the COVID-19 pandemic from contaminated water by magnetic graphene oxide/MIL-88 metal-organic framework/alginate hydrogel beads. Chemosphere. 2024 Mar 1;352:141397.
[22] Mohamed A, Atta RR, Kotp AA, Abo El-Ela FI, Abd El-Raheem H, Farghali A, Alkhalifah DH, Hozzein WN, Mahmoud R. Green synthesis and characterization of iron oxide nanoparticles for the removal of heavy metals (Cd2+ and Ni2+) from aqueous solutions with Antimicrobial Investigation. Scientific Reports. 2023 May 4;13(1):7227.
[23] Sardi A, Reksamunandar RP, Maulida Z, Arsa DA, Lubis SS, Nisah K. Green synthesis of NiO nanoparticles using a Cd hyperaccumulator (Lactuca sativa L.) and its application as a Pb (II) and Cu (II) adsorbent. Environmental Nanotechnology, Monitoring & Management. 2024 May 1;21:100910.
[24] Saleem MU, Hussain H, Shukrullah S, Yasin Naz M, Irfan M, Rahman S, Ghanim AA. Study of kinetics and the working mechanism of silica-coated amino-functionalized CoFe2O4 ferrite nanoparticles to treat wastewater for heavy metals. ACS omega. 2024 Jan 23;9(3):3507-24.
[25] Patel M, Lanakapati H, Maheria K. Efficient removal of Pb2+, Cd2+, and Hg2+ from wastewater using advanced graphene oxide-zirconium hybrid composite. ACS Applied Engineering Materials. 2024 May 30;2(6):1542-60.
[26] Chandra D, Molla MT, Bashar MA, Islam MS, Ahsan MS. Chitosan-based nano-sorbents: synthesis, surface modification, characterisation and application in Cd (II), Co (II), Cu (II) and Pb (II) ions removal from wastewater. Scientific Reports. 2023 Apr 13;13(1):6050.
[27] Sodzidzi Z, Phiri Z, Nure JF, Msagati TA, De Kock LA. Adsorption of toxic metals using hydrous ferric oxide nanoparticles embedded in hybrid ion-exchange resins. Materials. 2024 Mar 1;17(5):1168.
[28] Osman H, Uğurlu M, Vaizoğullar Aİ, Atasoy M, Chaudhary AJ. Statistical modeling and optimization of heavy metals (Pb and Cd) adsorption from aqueous solution by synthesis of Fe3O4/SiO2/PAM: isotherm, kinetics, and thermodynamic. Polymer Bulletin. 2024 Nov;81(16):14513-45.
[29] Ahmadi S, Izanloo C. Biosynthesis of iron oxide nanoparticles at different temperatures and its application for the removal of Zinc by plant mediated nanoparticle, as an eco-friendly nanoadsorbent. Results in chemistry.2023 Dec 1;6:101192.

[30] Açıkgöz M, Rahmanberdyyev N, Başkan G. Olive leaf extract-assisted preparation of nanoferrite for adsorptive removal of cationic dye. Materials Chemistry and Physics. 2024 Sep 1;323:129662.
[31] Irshad MA, Sattar S, Al-Huqail AA, Alghanem SM, Nawaz R, Ain NU, Hussaini KM, Abeed AH. Green synthesis and characterization of silver and copper nanoparticles and their use as an effective adsorbent for chromium removal and recovery from wastewater. Environmental Science and Pollution Research. 2023 Nov;30(52):112575-90.
[32] Şahin M, Arslan Y, Tomul F, Akgül F, Akgül R. Green synthesis of metal nanoparticles from Codium macroalgae for wastewater pollutants removal by adsorption. CLEAN–Soil, Air, Water. 2024 May;52(5):2300187.
[33] Mohammadpour A, Karami N, Zabihi R, Fazeliyan E, Abbasi A, Karimi S, de Farias MB, Vieira MG, Shahsavani E, Khaneghah AM. Green synthesis, characterization, and application of Fe3O4 nanoparticles for methylene blue removal: RSM optimization, kinetic, isothermal studies, and molecular simulation. Environmental Research. 2023 May 15;225:115507.
[34] Abegunde SM, Adebayo MA, Olasehinde EF. Green synthesis of ZnO nanoparticles and its application for methyl green dye adsorption. Green Energy and Resources. 2024 Jun 1;2(2):100073.
[35] Tesnim D, Hédi BA, Ridha D, Cid-Samamed A. Green low-cost synthesis of zero-valent iron nanoparticles from Palm Petiole Extract for Cr (VI) removal from water. Environmental Science and Pollution Research. 2024 Jul;31(31):44272-88.
[36] Sharma P, Prakash J, Kaushal R. Eco-friendly synthesis of amino and carboxyl-functionalized silica nanoparticles for enhanced adsorption of water pollutants. Hybrid Advances. 2024 Aug 1;6:100209.
[37] Ferenj AE, Kabtamu DM, Assen AH, Gedda G, Muhabie AA, Berrada M, Girma WM. Hagenia abyssinica-biomediated synthesis of a magnetic Fe3O4/NiO nanoadsorbent for adsorption of lead from wastewater. ACS omega. 2024 Feb 2;9(6):6803.
[38] Irshad MA, Latif M, Nasim I, Nawaz R, Zahoor AF, Al-Mutairi AA, Al-Hussain SA, Irfan A, Zaki ME. Efficient chromium removal from leather industrial wastewater in batch experimental study: Green synthesis and characterization of zinc oxide nanoparticles using Ficus benghalensis extracts. Ecotoxicology and Environmental Safety. 2024 Aug 1;281:116616.
[39] Chen D, Chen J, Zhou W, Sawut A. Preparation of the New Magnetic Nanoadsorbent Fe3O4@ SiO2-yl-VP and Study on the Adsorption Properties of Hg (II) and Pb (II) in Water. Magnetochemistry. 2024 Dec 13;10(12):105.
[40] Takeda N, Fukushi K, Okuyama A, Takahashi Y. Solid–liquid partitioning and speciation of Pb (II) and Cd (II) on goethite under high pH conditions, as examined by subnanomolar heavy metal analysis, X-ray absorption spectroscopy, and surface complexation modeling. Chemosphere. 2024 Sep 1;363:142766.
[41] Piasecki W, Lament K. Application of surface complexation modeling to investigate the mechanism of Cu2+ adsorption on TiO2, Al2O3, and SiO2 under high surface coverage. Molecules. 2024 Nov 26;29(23):5595.
[42] Ishag A, Zhu W, Yue Y, Hou R, Zhang B, Sun Y. Synergistic removal of U (VI), Pb (II), and HA on nZVI/MoS2 composites investigated by batch, spectroscopic, and modeling techniques. Industrial & Engineering Chemistry Research. 2024 Jun 18;63(26):11453-62.
[43] Kocik EM, Kim A, Aiken ML, Smith L, Kim CS. Sulfate enhances the adsorption and retention of Cu (II) and Zn (II) to dispersed and aggregated iron oxyhydroxide nanoparticles. Applied Geochemistry. 2024 Feb 1;162:105929.
[44] Hamidon TS, Garba ZN, Zango ZU, Hussin MH. Biopolymer-based beads for the adsorptive removal of organic pollutants from wastewater: Current state and future perspectives. International Journal of Biological Macromolecules. 2024 Jun 1;269:131759.
[45] Zhao S, Li Q, Tang Z, Yang Y, Wu J, Gao P, Qian Y, Chen J, Xue G. Simultaneous removal of Cr, Cu, Zn, and Cd by nano zero-valent iron modified sludge biochar in high salinity wastewater. Separation and Purification Technology. 2024 Nov 11;347:127560.
[46] Chen H, Xiao R, Huang D, Deng R, Li R, Chen Y, Zhou W. Three kinds of apatite adsorbents prepared by co-precipitation for Pb (II) and Cd (II) removal from wastewater: Performance, competitive effects and mechanisms. Journal of Molecular Liquids. 2024 Apr 15;400:124478.
[47] Jain G, Bhattacharyya P, Mandal MK, Chaudhuri RG, Chakrabarti S. pH-dependent adsorption of the sulfamethoxazole antibiotic on HKUST-1@ CNS nanocomposite corroborating efficiency, mechanistic, and kinetic studies. New Journal of Chemistry. 2024 Jan 22;48(4):1781-91.

[48] Alkhaldi H, Alharthi S, Alharthi S, AlGhamdi HA, AlZahrani YM, Mahmoud SA, Amin LG, Al-Shaalan NH, Boraie WE, Attia MS, Al-Gahtany SA. Sustainable polymeric adsorbents for adsorption-based water remediation and pathogen deactivation: a review. RSC advances. 2024 Oct 21;14(45):33143-90.
[49] Elmorsi ET, Lai EP. Desorption of pharmaceutical hydrochlorides from transition metal oxide nanoparticles–investigation by capillary electrophoresis. RSC advances. 2024 Dec 19;14(54):39890-901.
[50] Dhaouadi F, Aouaini F, Basha B, Bonilla-Petriciolet A, Georgin J, Lamine AB. Evaluation and analysis of the adsorption mechanism of three emerging pharmaceutical pollutants on a phosphorised carbon-based adsorbent: Application of advanced analytical models to overcome the limitation of classical models. Heliyon. 2024 Jul 30;10(14).
[51] Sheraz N, Shah A, Haleem A, Iftikhar FJ. Comprehensive assessment of carbon-, biomaterial-and inorganic-based adsorbents for the removal of the most hazardous heavy metal ions from wastewater. RSC advances. 2024 Apr 9;14(16):11284-310.
[52] Ahmaruzzaman M. Magnetic nanocomposites for removal of arsenic from water. Asian Journal of Water, Environment and Pollution. 2024 Feb 6;21(1):11-6.
[53] Hossain MS, Yasmin S, Kabir MH. Cost-effective synthesis of magnetic graphene oxide nanocomposite from waste battery for the removal of arsenic from aqueous solutions: adsorption mechanism with DFT calculation. Journal of Saudi Chemical Society. 2024 May;28(3):101873.
[54] Govarthanan M, Mythili R, Kim W. Magnetic mesoporous carbon as excellent adsorptive material for arsenic removal from aqueous environment. Journal of Industrial and Engineering Chemistry. 2024 Sep 25;137:132-43.
[55] Faustino B, Cobo DM, Vequizo R, Candidato Jr R. Enhanced heavy metal adsorption capacity of surface-functionalized Philippine natural zeolite in simulated wastewater. Open Ceramics. 2024 Jun 1;18:100612.
[56] Faustino B, Cobo DM, Vequizo R, Candidato Jr R. Enhanced heavy metal adsorption capacity of surface-functionalized Philippine natural zeolite in simulated wastewater. Open Ceramics. 2024 Jun 1;18:100612.
[57] Abdolmaleki A, Mohamadi Z, Bazyar Z. A simple, efficient, and rapid method for dye removal from wastewater using an IDA-GO@ Fe3O4 magnetic nanocomposite. RSC advances. 2024 Sep 2;14(38):2784351.
[58] Hubetska T, Demchenko V, Kobylinska N. Surface engineering: binary Mg, Fe-LDH· x Fe3O4 nanocomposites for improved magnetic solid-phase extraction of pharmaceuticals from aqueous solution. Materials Advances. 2024 Oct 14;5(20):8145-63.
[59] Hussain E, Shahadat M, Ahtesham A, Ibrahim MN. Synthesis, characterization, and applications of ambi-functional PANI/GO/MOF-Fe3O4 magnetic nanocomposite for removing industrial dye and emerging contaminant. Separation and Purification Technology. 2024 Dec 24;351:128052.
[60] Wang Y, Cheng L, Liu X, Ding J, Zhang N, Li Z, Zhao M, Meng F, Meng Z. Removal of pesticides by layered double hydroxide modified different clay minerals and site energy analysis. Chemical Engineering Science. 2024 Apr 5;287:119803.
[61] Iuliano M, Cirillo C, Astorga EN, Sarno M. A new nanocomposite as adsorbent and catalyst for enhanced removal of methylene blue. Surfaces and Interfaces. 2024 Aug 1;51:104582.
[62] Kuppusamy B, Gopalakrishnan S, Natesan S, Rajamohan N, Rajasimman M, Yusuf M, Kamyab H. Valorization of sugarcane bagasse cellulose to synthesize novel graphene oxide-based composite for remediation of atrazine–Optimization studies. Journal of Environmental Chemical Engineering. 2024 Jun 1;12(3):112767.
[63] Wang J, Licciardello N, Sgarzi M, Cuniberti G. Multifunctional polymer-based nanocomposites for synergistic adsorption and photocatalytic degradation of mixed pollutants in water. Nanoscale Advances. 2024 Mar 12;6(6):1653-60.
[64] Ferenji AE, Hassen YE, Mekuria SL, Girma WM. Biogenic mediated green synthesis of NiO nanoparticles for adsorptive removal of lead from aqueous solution. Heliyon. 2024 Jun 15;10(11).
[65] Sodzidzi Z, Phiri Z, Nure JF, Msagati TA, De Kock LA. Adsorption of toxic metals using hydrous ferric oxide nanoparticles embedded in hybrid ion-exchange resins. Materials. 2024 Mar 1;17(5):1168.

Journal of Nanotechnology and Innovative Materials

Review Article

Structural phase transitions and control of superionic transport in copper and silver chalcogenides

Yusif. I. Aliyev[1,2], Ophelya. R. Babayeva[1], and Sevinc. R. Azimova[3]

[1]Azerbaijan State Pedagogical University, Baku, Azerbaijan
[2]Western Caspian University, 31 Istiglaliyyat Street, Baku, Azerbaijan.
[3]Institute of Physics, Ministry of Science and Education of the Republic of Azerbaijan, Baku, Azerbaijan

Received: 27.07.2026 Accepted: 26.09.2026 Published: 12.10.2026
https://doi.org/10.54414/BJSA1833

Copyright: © 2026 by the authors. Licensee: Journal of Nanotechnology and Innovative Materials, Western Caspian University, Baku, Azerbaijan. This article is an open-access article distributed under the terms and conditions of the Creative Commons Attribution 4.0 International License (CC BY 4.0).

Abstract

Chalcogenides of copper and silver have been proposed as prospective thermoelectrics due to their low thermal conductivity, strong anharmonicity, polymorphism with temperature dependence, and liquid-like mobility of the cation in the high-temperature phases. The current review analyzes published data concerning high-temperature X-ray diffraction, differential thermal analysis, and ab initio investigations of Cu2Se, Ag2S, AgCuS, AgCuSe, Cu4Se1.5Te0.5, and Cu4Te1.5Se0.5 in a unified comparative way. Three key factors determining their functional behavior are outlined: disordering of the Cu+/Ag+ sublattice within a relatively intact anion framework; transitions from lower-symmetry structures to higher-symmetry cubic modifications; and the impact of substitutions of cations and anions on transition temperatures and properties of the carrier–phonon interaction. Characteristic temperatures are given as 407 K for the orthorhombic-cubic transition in Cu2Se, about 450 K for the acanthite-argentite transition in Ag2S, and 930 K for the Cmcm-Fm$\bar{3}$m transition in AgCuS. The phenomena of structural transformations and thermal events in the Cu–Se–Te materials cover a wider temperature regime and need to be interpreted on a case-by-case basis. Thermodynamics and kinetics of the phenomenological framework link free energy, ion site occupation, correlation of diffusion, and transport. This framework has not been parameterized based on data obtained for specific materials and does not provide new experimental or ab initio information. Structure mapping, concurrent analysis of the structure and calorimetry, transport properties study, and operando mobility studies have been suggested for phase control and stability assessment.

Keywords: copper and silver chalcogenides; superionic conduction; structural phase transitions; cation disorder; thermoelectric materials; solid solutions; high-temperature X-ray diffraction; phase stability

1. Introduction

Conversion of thermal energy into electrical energy without any mechanical energy is the physical principle on which thermoelectric generators work. They operate without noise, have no moving parts, and can be designed for particular purposes. Performance of materials is measured in terms of the dimensionless parameter $zT=S^2\sigma T/\kappa$, where S is the Seebeck coefficient, σ is the electrical conductivity, T is the absolute temperature, and κ is the total thermal conductivity. The interrelation between these properties makes it hard to decrease thermal conductivity without decreasing electrical conductivity. Copper and silver chalcogenides have a unique property that is determined by their crystal structure: while a rigid anion sublattice serves as the periodic medium for the electron flow, mobile cations in the high-temperature phase serve as the medium for phonon scattering [1], [2], [3], [4].

Cu2Se is a prototypical example of a phonon-liquid/electron-crystal system. Recent works have considered the significant variation of electrical and thermal transport properties near the phase transition of this compound, along with high zT values and the issues associated with cation movement and device reliability [3], [4], [5], [6]. The Ag2S and Ag2Se systems are of special importance for low-temperature thermoelectric

applications and flexible and wearable devices [7], [8], [9], [10]. Ternary compounds such as AgCuS and AgCuSe can be considered model systems for understanding the competition between the two cations in their site preference for the same anion framework. Cu-Se-Te solid solutions can be used to study the impact of anion size and bond polarizability on phase stability [11], [12], [13], [14], [15], [16].

Nonetheless, such materials are frequently considered as distinct classes of materials. This review attempts to consolidate the previous studies conducted by the author and other recent studies in order to reveal common structural motifs and to develop a general phase engineering approach to functional chalcogenides. Special emphasis is placed on the differences between structural transitions, predicted ion dynamics, and observed transport phenomena.

2. Materials and methods

The present research is a structured comparative analysis of already existing scientific results and not experimental work. The data set includes high-temperature X-ray diffraction (XRD) investigation of Cu2Se in the range 290 – 1000 K [11] XRD and differential thermal analysis (DTA) of AgCuS [12], Density functional theory (DFT) study of the electronic structures of Ag2S and Ag2Se [13], reversible dissociation and combination reaction in the Ag-Cu-Se system [14], polymorphism in AgCuSe0.5(S,Te)0.5 compounds [15] and DTA and XRD of Cu4Se1.5Te0.5 and Cu4Te1.5Se0.5 systems [16], [17]. The general structural information is provided by the comparative study on cation and anion substitution in the chalcogenides [18]. The sequence of XRD for the tellurium-rich composition is additionally presented in a public dissertation abstract [19].

Four parameters are used in this comparison: room-temperature symmetry and phase composition; typical transformation temperature; high-temperature symmetry and reversibility; and potential transport properties implications. Obtained temperatures from different techniques cannot be considered equal to one another. XRD identifies crystal structure change while DTA observes heat effect. Kinetics, heating rate, sample treatment, volatiles, and nonstoichiometry could result in discrepancies between the temperatures presented. This problem is especially critical when comparing XRD transformation at 558 K and DTA transformation around 800 K in Cu4Se1.5Te0.5 [16], [17]. Synthesis is literature- and source-based. It is not a review or meta-analysis.

3. Results and discussion

3.1. Cu_2Se from low symmetry to a superionic cubic phase

The temperature-driven transformation of Cu2Se is used as the reference for comparison. In the corresponding author's X-ray diffraction study performed at high temperatures, it was suggested that the room-temperature crystal structure corresponds to the orthorhombic form of the substance with the space group $P222_1$, and a transition to a cubic form with the space group $F\bar{4}3m$ occurs at 407 K [11]. The transition temperature is in agreement with other published data that fall within the range of 400-414 K [3], [4], [5], [6]. In the course of the transition, the selenium lattice remains intact, while copper cations populate a variety of sites.

A combination of higher symmetry on an average crystalline scale and dynamic disorder at the local scale is a hallmark of superionic thermoelectrics. A decreased phonon mean free path can lower κL even when the concentration and mobility of carriers are still strongly dependent on copper vacancies. Nonetheless, high zT in and of itself does not guarantee technological stability. Copper migration, compositional modifications at electrode boundaries, and oxidation may constrain long-term stability when the material is operated under electrical current and a temperature gradient [5], [6].

3.2. Ag_2S and AgCuS in two cation mobility regimes

At low temperatures, Ag2S is a semiconductor that crystallizes with the acanthite structure (monoclinic system) and has a space group of $P2_1/c$. At a temperature above about 450 K, Ag2S crystallizes in the higher symmetry argentite structure and shows superionic conductivity [7], [8], [20]. The first-principles calculations by the corresponding author have shown that Ag2S with a monoclinic structure ($P2_1/c$) is a semiconductor, while its higher symmetry could make it semimetallic [13]

For AgCuS, the conversion of the orthorhombic Cmcm structure at room temperature to the cubic $Fm\bar{3}m$ structure at 930 K is marked by a DTA endotherm with a peak at 938 K [12]. It can be seen from its higher transition temperature compared to Ag2S that it has a different enthalpy and entropy relationship; however, it cannot show whether the migration energy is higher than that of Ag2S.

3.3. AgCuSe and mixed cation systems

AgCuSe is both a distinct ternary compound and an important intermediate phase in the Ag–Cu–Se phase equilibria. The high-temperature face-centered cubic (fcc) modification of $Ag_{1.5}Cu_{0.5}Se$ reversibly decomposes into Ag_2Se + AgCuSe below 488 K, whereas $Ag_{0.4}Cu_{1.6}Se$ reversibly decomposes into Cu_2Se + AgCuSe below 540 K [14]. These observations identify AgCuSe as a chemical bridge between silver-rich and copper-rich compositions.

3.4. Phase boundary control by anion substitution in Cu–Se–Te

Substitution of tellurium for selenium leads to the alteration of anion mass, ionic radius, bond polarizability, and lattice anharmonicity. According to the high-temperature XRD analysis, the low-temperature $R\bar{3}m$ phase of Cu4Se1.5Te0.5 exhibits a reversible transformation into the cubic phase with the lattice constant a ~ 5.899 Å [17] at 558 K. Endothermic effects appear at 413 and 800 K, while the exothermic effect is detected at 725 K for Cu4Se1.5Te0.5, and endothermic effects are registered at 410, 465, and 800 K for Cu4Te1.5Se0.5 [16]. Signals around 410 and 465 K could relate to adsorbed water or surface phenomena. The issue of whether the effect at 800 K is associated with a phase transition, structural rearrangement, or other processes is to be solved via a joint XRD-DSC-TGA analysis. The published dissertation abstract states that decomposition of Cu4Te1.5Se0.5 occurs at ~ 770 K into the hexagonal Cu2(SeTe)0.5 and cubic Cu2Te phases, and the cubic phase appears at 850 K [19].

The discrepancy between the XRD and DTA temperatures is supposed to be investigated as a possible sign of a multistage process instead of a contradiction. One possible scenario is that local or partial structural rearrangement begins at lower temperature, whereas a bulk transformation or a thermally more pronounced event occurs at higher temperature. Testing this hypothesis requires simultaneous high-temperature XRD–DSC, temperature-dependent Raman spectroscopy, and electrical and thermal transport measurements on the same sample.

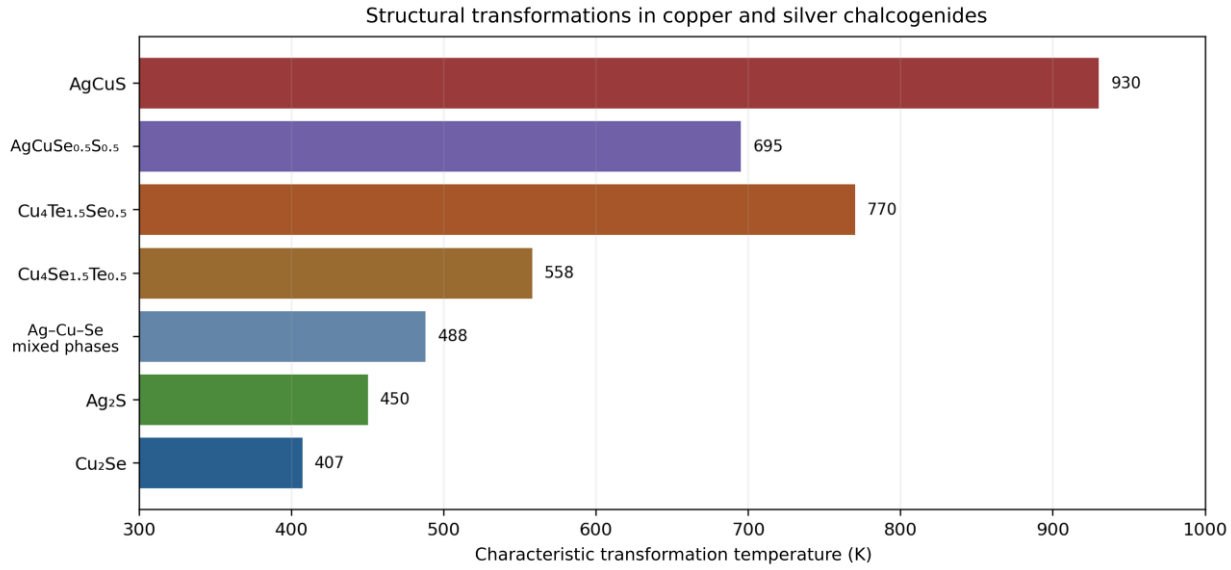


Figure 1. Comparison of characteristic structural transformation temperatures in copper and silver chalcogenides based on published data. For Ag–Cu–Se, 488 K denotes the reversible boundary $Ag_{1.5}Cu_{0.5}Se \rightleftharpoons Ag_2Se$ + AgCuSe; for $Cu_4Te_{1.5}Se_{0.5}$, 770 K denotes the onset of phase separation observed by high-temperature XRD. DTA peak temperatures and XRD phase boundaries are methodologically distinct and should not be treated as the same physical quantity [11], [12], [13], [14], [15], [16], [17], [19], [20].

3.5. A theoretical framework for phase stability, cation dynamics, and transport

The following phenomenological framework is proposed for the systems compared here. Composition, temperature, and defects alter phase free energies, cation site occupancies, and hopping kinetics, which influence electronic and thermal transport through distinct channels. High average symmetry can coexist with dynamic disorder, but the observation of a cubic phase by XRD does not by itself prove superionic conduction. The framework presents no new DFT, ab initio molecular dynamics (AIMD), or experimental results. Its purpose is to connect published observations with testable thermodynamic and kinetic relationships.

3.5.1. Free energy and disordering

At constant pressure and fixed overall composition, the free-energy difference between the high-temperature phase H and the low-temperature phase L is written as

$$\Delta G(T,x) = G_H - G_L = \Delta H(T,x) - T\Delta S(T,x) \quad (1)$$

Here, x is the substitution fraction, and ΔH and ΔS are the enthalpy and entropy differences expressed using the same molar normalization. At an equilibrium boundary, ΔG = 0. For a first-order transition, if ΔH and ΔS are approximately constant near the transition, $T_t \approx \Delta H/\Delta S$; this relation does not automatically apply to a continuous transition. Entropy includes configurational, vibrational, and electronic contributions. Differences between heating and cooling boundaries can reflect nucleation and kinetic delay in addition to the equilibrium transition temperature.

$$S_{conf} = -R \Sigma_s \nu_s \Sigma_i y_{is} \ln y_{is}, \quad \Sigma_i y_{is} = 1$$

In this expression, νs represents the number of sites of kind s per mole of formula units, while yis represents the fraction of occupancy of component i on those sites, vacancies being considered a different kind of component whenever needed. The above expression is based on independent and ideally mixed sites, without considering short-range interactions. The entropy resulting from the mixing of Cu and Ag and the entropy resulting from the redistribution of cations on further sites cannot be counted twice as the same effect. (2)

3.5.2. Mixing and phase separation

$$\Delta G_{mix} = \Omega x(1-x) + RT[x \ln x + (1-x)\ln(1-x)] \quad (3)$$

Ω is the molar interaction parameter in the symmetric binary regular solution approximation. The stability of a homogeneous system is assured only if $\partial^2G/\partial x^2 > 0$; negative $\partial^2G/\partial x^2$ suggests spinodal decomposition instability. Two-phase equilibrium occurs by the common tangent method. At a constant, positive Ω, the theory predicts a critical temperature of Tc = Ω/(2R). Figure 2b conceptually illustrates the preference for a two-phase state at low temperature and the dominance of mixing entropy at higher temperature. Real Ag–Cu–Se and Cu–Se–Te systems are multicomponent. Calculating their phase boundaries requires a separate Gibbs-energy description for each phase, stoichiometric constraints, and mass balance. Since Ω is not fitted here, the model does not yield new material-specific phase-boundary temperatures.

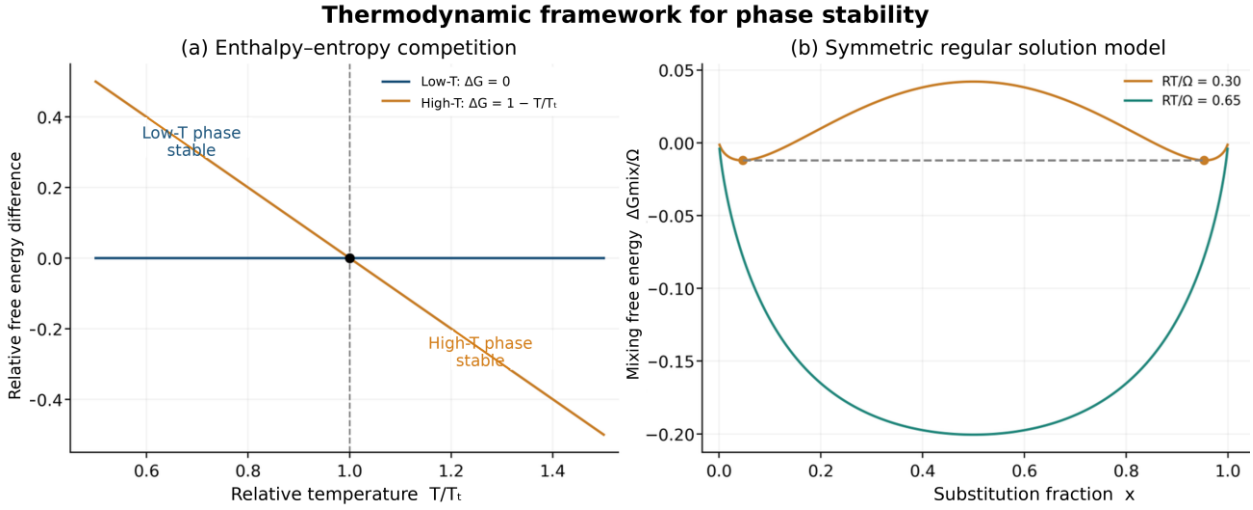


Figure 2. Conceptual thermodynamic framework. (a) $\Delta G/\Delta H = 1 - T/T_t$ for constant ΔH and ΔS, with the low-temperature phase used as the reference. (b) Dimensionless mixing-free-energy curves, $\Delta G_{mix}/\Omega$, for a symmetric regular solution with $\Omega > 0$; the dashed line is the common tangent to the low-temperature curve. The dimensionless parameters are illustrative and are not fitted to experimental data.

3.5.3. Diffusion and mixed conduction

$$D^*(T) = D_0 \exp[-\frac{E_a}{k_B T}], \quad \sigma_{ion} = \frac{n_i q_i^2 D_\sigma}{k_B T} \tag{4}$$

D* is the tracer self-diffusion coefficient, D_0 is the pre-exponential factor, E_a is the effective activation energy, n_i is the volumetric concentration of mobile ions, q_i is the ionic charge, and D_σ is the conductivity diffusion coefficient. The values of D* and Dσ can be considered equal only under uncorrelated conditions; correlations are measured using the Haven ratio HR = D*/Dσ. When the concentration of vacancies is a function of temperature, then Ea can be different from the activation energy of a single jump.

Arrhenius fitting should be restricted to a single phase and comparable defect regimes.

$$\sigma_{tot} = \sigma_{el} + \sigma_{ion}, \quad t_{ion} = \frac{\sigma_{ion}}{\sigma_{tot}} \tag{5}$$

The above decomposition relies on a linear response of a homogeneous material subjected to suitable boundary conditions. In the case of ion-blocking electrodes, the long-time direct current response will differ from the transient and alternating current response. Therefore, it becomes imperative that the conductivities be separated using impedance techniques, selection of suitable electrodes, and polarization studies. The flux of ions depends on the concentration gradient, electric field, and temperature gradient. DFT calculations with the NEB approach and AIMD calculations are two such complementary methods.

3.5.4. Phonon and electronic transport

$$\kappa = \kappa_L + \kappa_{el}, \quad \kappa_L \approx \frac{C_V v_s \ell}{3}, \quad \kappa_{el} \approx L\sigma_{el}T \tag{6}$$

The heat capacity per unit volume is denoted by CV, the characteristic sound velocity is vs, and the phonon mean free path is ℓ. The kinetic relation holds true only as long as the quasiparticle theory for phonons is applicable; its applicability in the strongly anharmonic superionic state needs to be determined independently. The Wiedemann–Franz separation demands that the appropriate value for L be selected, taking into account the nature of the band structure and the scattering regime. Equation (6) will have to be modified in case of bipolar or other transport processes. The variations in mass, strain, interface effects, and anharmonicity affect κL [1], [2]. Nonetheless, neutron scattering data for Cu2Se do not justify the hypothesis that ion hopping destroys transverse phonons completely. [21].

$$\sigma_{el} \approx ne\mu, \quad zT_{el} = \frac{{S_{el}}^2 \sigma_{el} T}{\kappa_L + \kappa_{el}}$$

Under a single dominant carrier assumption, n is the carrier density, μ is carrier mobility, and e is the elementary charge. Sel represents the Seebeck coefficient at the steady state. Structural fluctuations may change band edges and the carrier-phonon interaction [4]. Nevertheless, information on Sel, σel, and κ must be measured under identical temperature and phase conditions. The presence of heat-capacity anomalies, latent heat, and transient temperature fields near a phase transition point may impact measurements. The direct substitution of measured total electrical conductivity and transient thermoelectric voltage into Equation (7) thus needs to be justified for the mixed conductor. Figure 3 summarizes independent approaches to verify the approach. (7)

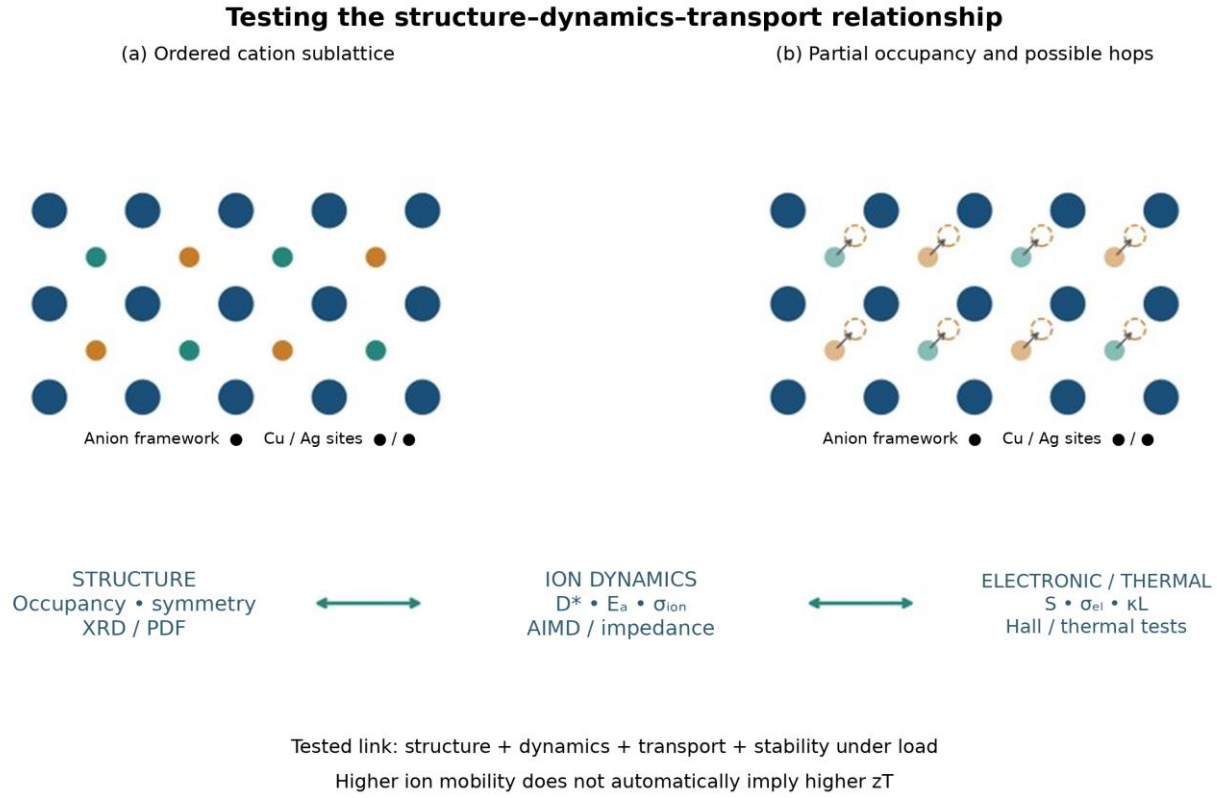


Figure 3. Conceptual diagram of the structure–dynamics–transport relationship. Blue circles denote the anion framework, orange and green circles denote cation sites, and dashed outlines indicate alternative sites. Arrows represent possible hops. The geometry does not depict the unit cell, site occupancies, or migration pathways of a specific compound. PDF denotes the atomic pair distribution function. The lower part shows the combined validation of structural, dynamic, and functional measurements.

3.5.5. Testable predictions and limitations

First, if the entropy advantage of the high-temperature phase is a principal driving force, changes in site occupancies should be consistent in direction with the calorimetric entropy change. Such agreement is not conclusive because vibrational contributions are also present. Second, if Cu↔Ag substitution restricts ion motion, D* or σ_{ion} should decrease, or the fitted E_a should increase, at the same temperature and in comparable phase and defect states. The opposite outcome would not support the migration-restriction hypothesis.

Third, if a secondary phase enhances phonon scattering, κ_L should decrease after accounting for density and electronic heat transport. A proposed energy-filtering effect requires that an increase in S_{el} cannot be explained solely by a change in carrier concentration and must be supported by interfacial-barrier and mobility data. Fourth, if the events at 558 and 800 K belong to a single multistage process, the temperature evolution of phase fractions should correlate with thermal effects in the same sample. Mass loss or the appearance of new phases would require alternative explanations.

These available data do not allow for dependable quantification of values of ΔH, ΔS, Ω, Ea, D0, or HR. The model does not offer, thus, a fitting predictive calculation. The significance of the proposed model lies in establishing connections between structural features and certain measurable parameters of thermodynamic stability and conductivity.

Table 1. Comparative summary of structural transformations in copper and silver chalcogenides.

System	Low-temperature state	Characteristic T (K)	High-temperature outcome	Functional implications
Cu_2Se	Orthorhombic $P222_1$	407	Cubic $F\bar{4}3m$	Superionic Cu sublattice; low κ_L; stability assessment required
Ag_2S	Monoclinic $P2_1/c$	≈450	Cubic argentite	Ductility and near-room-temperature thermoelectric relevance
AgCuS	Orthorhombic Cmcm	930 (XRD); 938 (DTA)	Cubic $Fm\bar{3}m$	Collective cation disorder at high temperature
Ag–Cu–Se	Multiphase	488–540	fcc composition field	Phase and interface engineering through intermediate AgCuSe
$AgCuSe_{0.5}S_{0.5}$	$Cu_{1.96}S$ + AgCuSe	695	Single fcc phase	Phase-boundary tuning by anion substitution
$Cu_4Se_{1.5}Te_{0.5}$	$R\bar{3}m$	558 (XRD); 800 (DTA)	Cubic phase / thermal event	Possible multistage transformation
$Cu_4Te_{1.5}Se_{0.5}$ [22]	Trigonal/multiphase	770–850 (XRD)	Phase separation → cubic phase	More complex kinetics in the Te-rich composition

Note: XRD phase boundaries, decomposition onsets, and DTA peak temperatures describe different observables. fcc denotes face-centered cubic.

4. Future research directions

What follows will be the determination of the time-, composition-, and load-dependent behavior of the transformation phenomena rather than the identification of additional isolated transition temperatures. The primary concern should be the joint analysis of XRD-DSC and transport properties on the same material at high temperature. It would prove whether there is any coincidence in the timing for the beginning of structural change, thermal effects, and anomalous Seebeck or conductivity response. Special attention should be paid to the transient behavior of the Seebeck coefficient [4].

The second objective will be to develop a composition-temperature-phase map for cation substitution in Cu ↔ Ag along with anion substitution in S ↔ Se ↔ Te. The goal here would be to ensure that the transition takes place slightly below the required operating window, with a single phase maintaining symmetry being used throughout operation and minimal decomposition taking place with thermal cycling. The third objective will be testing of the operando stability by measuring the migration of Cu/Ag cations near electrodes in a temperature gradient and with DC current using scanning electron microscopy with EDS or WDS, micro-XRD, and impedance spectroscopy.

Hypothesis: Suitable amounts of mixed cations and mixed anions could inhibit phononic energy transfer due to mass fluctuation and strain effects. Coherent or nanoscale AgCuSe-like phases could act as energy filters; the presence of silver ions could limit the diffusion of copper. The above-mentioned benefits can be considered useful in technological applications only when stability and durability under electrical loading are proven.

5. Conclusion

The main takeaway is that both the structural, thermal, and electronic aspects of the phase transitions need to be measured simultaneously, instead of relying on an isolated value of zT to evaluate performance. For the

optimization of this material class, there must be a compromise between nearness to the phase transition point and stability during operation. Such a comparison can be carried out rationally using simultaneous measurement of XRD-DSC-transport, composition analysis, and migration studies under operando conditions. This is made possible by the thermodynamic and kinetic framework that we have outlined. The figures shown are not new experimental or first-principles calculations.

The key finding is the importance of studying the structural, thermal, and electronic contributions to phase transitions in tandem, rather than assuming high zT implies good performance. Optimizing this class of materials entails the delicate balancing act of being near a phase boundary while also being operationally stable. A combination of XRD-DSC-transport measurements, compositional analysis, and operando ion migration studies forms the rationale behind the proposed approach for assessing tunable superionic chalcogenides. The suggested thermodynamic and kinetic model allows this to be evaluated via quantitative metrics on free energy, site occupancy, ion diffusion, and electron transport. The example figures shown here are not new data or first-principles results.

Acknowledgments
The authors thank Dr. Sakin Jabarov (Doctor of Sciences in Physics) for his assistance in preparing this manuscript.

Funding information
This research did not receive any specific grant from funding agencies in the public, commercial, or not-for-profit sectors.

Conflict of interest statement
The authors declare no conflicts of interest.

Data availability
This review uses previously published findings identified in the reference list. No new experimental dataset is reported. Figures 2 and 3 are conceptual illustrations, and their parameters are not fitted to experimental data.

References

[1] Liu H, Shi X, Xu F, Zhang L, Zhang W, Chen L, Li Q, Uher C, Day T, Snyder GJ. Copper ion liquid like thermoelectrics. Nature materials. 2012 May;11(5):422-5. https://doi.org/10.1038/nmat3273

[2] He J, Tritt TM. Advances in thermoelectric materials research: Looking back and moving forward. Science. 2017 Sep 29;357(6358):eaak9997. https://doi.org/10.1126/science.aak9997

[3] K, Choi S, Hirata K, Adachi M, Kiyama M, Matsuura T, Yamamoto Y, Matsunami M, Takeuchi T. Discovery of colossal Seebeck effect in metallic Cu2Se. Nature communications. 2019 Jan 8;10(1):72. https://doi.org/10.1038/s41467-018-07877-5

[4] Zhao K, Yue Z, Wuliji H, Chen H, Deng T, Lei J, Qiu P, Chen L, Shi X. Modeling critical thermoelectric transports driven by band broadening and phonon softening. Nature Communications. 2024 Jan 26;15(1):776. https://doi.org/10.1038/s41467-024-45093-6

[5] Ying P, Jian Q, Gong Y, Song T, Yang Y, Geng Y, Huang J, Sun R, Chen C, Shen T, Li Y. Matrix plainification leads to high thermoelectric performance in plastic Cu2Se/SnSe composites. Nature Communications. 2025 Apr 7;16(1):3305. https://doi.org/10.1038/s41467-025-58484-0

[6] Nieroda P, Rudnik M, Mitoraj-Królikowska M, Drożdż E, Kozień D, Leszczyński J, Koleżyński A. Investigating the Stability of Cu2Se Superionic Thermoelectric Material in Air Atmosphere. Materials. 2025 Sep 4;18(17):4152. https://doi.org/10.3390/ma18174152

[7] Zhou WX, Wu D, Xie G, Chen KQ, Zhang G. α-Ag2S: A ductile thermoelectric material with high ZT. ACS omega. 2020 Mar 10;5(11):5796. https://doi.org/10.1021/acsomega.9b03929

[8] [Simonnin P, Sassi M, Gilbert B, Charlet L, Rosso KM. Phase transition and liquid-like superionic conduction in Ag2S. The Journal of Physical Chemistry C. 2020 Apr 14;124(18):10150-8. https://doi.org/10.1021/acs.jpcc.0c00260
[9] Zhu M, Shi XL, Wu H, Liu Q, Chen ZG. Advances in Ag2S-based thermoelectrics for wearable electronics: progress and perspective. Chemical Engineering Journal. 2023 Oct 1;473:145236. https://doi.org/10.1016/j.cej.2023.146194
[10] Lyu JM, Zhang L, Yang YL, Zhu JF, Shi XL, Chen ZG. Ag2Se-Based thermoelectric materials and devices: progress, challenges, and perspectives. Energy & Environmental Science. 2026 May 26;19(10):3134-83. https://doi.org/10.1039/D6EE01371F
[11] Dashdemirov AO, Aliyev YI, Bashirov RJ, Aliyeva NA, Rustamova LV. Structural aspects of the thermal properties of the Cu2Se. International Journal of Modern Physics B. 2024 Apr 20;38(10):2450150. https://doi.org/10.1142/S0217979224501509
[12] Aliyev YI, Asadov YG, Ilyasli TM, Mammadov FM, Naghiyev TG, Ismayilova ZA, Mirzayev MN, Jabarov SH. Structural aspects of thermal properties of AgCuS compound. Modern Physics Letters B. 2020 Feb 20;34(05):2050066. https://doi.org/10.1142/S0217984920500669
[13] Aliyev YI, Ismayilova NA, Novruzov RF, Dashdamirov AO, Huseynov HJ, Jabarov SH, Ayubov AA. Electron structure and density of states' calculations of Ag2S and Ag2Se crystals from first-principle. Modern Physics Letters B. 2019 Jul 30;33(21):1950242. https://doi.org/10.1142/S0217984919502427
[14] Aliyev YI, Asadov YG, Dashdemirov AO, Aliyeva RD, Naghiyev TG, Jabarov SH. Polymorphic transformations and thermal expansion of some modifications in Ag 1. 5 Cu 0. 5 Se and Ag 0. 4 Cu 1. 6 Se. International Journal of Modern Physics B. 2019 Sep 20;33(23):1950271. https://doi.org/10.1142/S0217979219502710
[15] Aliyev YI, Asadov YG, Aliyeva RD, Jabarov SH. Polymorphic transformations and thermal expansion in AgCuSe0. 5 (S, Te) 0.5 crystals. Semiconductors. 2017 Jun;51(6):732-9. https://doi.org/10.1134/s1063782617060045
[16] Aliyeva NA, Aliyev YI, Abiyev AS. Study of thermal properties of Cu4Se1. 5Te0. 5 and Cu4Te1. 5Se0. 5 compounds by differential thermal analysis. Advanced Physical Research. 2022;4(2):94-9. https://jomardpublishing.com/UploadFiles/Files/journals/APR/V4N2/Aliyeva_et_al.pdf
[17] Gasimova NA, Amiraslanov IR, Aliyev YI, Guseinov GG. Structure and Phase Transitions of Cu 4 Se 1.5 Te 0.5. InAIP Conference Proceedings 2011 Dec 26 (Vol. 1400, No. 1, pp. 476-479). American Institute of Physics. https://doi.org/10.1063/1.3663166
[18] Asadov YG, Aliyev YI, Babaev AG. Polymorphic transformations in Cu2Se, Ag2Se, AgCuSe and the role of partial cation-cation and anion-anion replacement in stabilizing their modifications. Physics of Particles and Nuclei. 2015 May;46(3):452-74. https://doi.org/10.1134/s106377961503003x
[19] Əliyeva NA. $Cu_4X_{2-m}Y_m$ tərkibli birləşmə və bərk məhlulların kristal quruluşu və quruluş faza keçidləri (X, Y = S, Se, Te; m = 0.0; 0.25; 0.50; 0.75) [fəlsəfə doktoru dissertasiyasının avtoreferatı]. 2021. https://aak.gov.az/upload/dissertasion/fizika/avtoreferat_ing_.pdf
[20] Sadovnikov SI, Kostenko MG, Gusev AI, Lukoyanov AV. Low-temperature predicted structures of Ag2S (Silver Sulfide). Nanomaterials. 2023 Sep 25;13(19):2638. https://doi.org/10.3390/nano13192638
[21] Voneshen DJ, Walker HC, Refson K, Goff JP. Hopping time scales and the phonon-liquid electron-crystal picture in thermoelectric copper selenide. Physical review letters. 2017 Apr 7;118(14):145901. https://doi.org/10.1103/physrevlett.118.145901

Journal of Nanotechnology and Innovative Materials

Research Article

Dependence of electrical resistance of polypropylene–mineral filler composites on temperature and ionizing radiation

Durdana F. Rustamova[1] ✉, **Sayyara A. Nabieva** [2] ✉ **, and Medine F. Nabili** ✉

[1]Department of Mechanics and Mathematics, School of Advanced Technologies and Innovation Engineering, Western Caspian University, Ahmad Rajabli 17A, III Parallel, AZ1001 Baku, Azerbaijan
[2] Institute of Physics, Ministry of Science and Education, 131 H. Javid Avenue, AZ1143 Baku, Azerbaijan
[3] First Chayli Secondary School named after Kamil Samadov, Shamakhi, Azerbaijan.

Received: 27.08.2026 Accepted: 01.10.2026 Published: 12.10.2026
https://doi.org/10.54414/RGGS8282

Copyright: © 2026 by the authors. Licensee: Journal of Nanotechnology and Innovative Materials, Western Caspian University, Baku, Azerbaijan. This article is an open-access article distributed under the terms and conditions of the Creative Commons Attribution 4.0 International License (CC BY 4.0).

Abstract

The article studies the changes in the electrical properties of composite materials based on polypropylene (PP) modified with varying amounts of α-Al_2O_3 and mica under the influence of temperature and ionizing radiation. In the studies, along with the original polypropylene, composites containing 20 and 40 wt.% α-Al_2O_3, as well as 20 and 40 wt.% mica, were compared. The temperature dependence of the specific resistance was investigated in the temperature range of 298÷480 K in the coordinates lgρ=f(T), and the changes in the electrical resistance after irradiation of the samples at doses of 50 kGy and 80 kGy were analyzed. It was found that in all the studied samples, an increase in temperature is accompanied by a decrease in specific resistance. This behavior is associated with the thermal activation of charge carriers in the polymer matrix and the strengthening of the temperature dependence of electrical conductivity. The inclusion of mineral fillers significantly increases the sensitivity of the electrical resistance of composites to temperature changes. In particular, in samples modified with mica, a more intensive decrease in resistivity is observed as the temperature increases. Increasing the radiation dose causes additional changes in the electrical properties of the composites, which can be explained by radiation-induced structural changes and the formation of local energy levels at the polymer-filler interface.

Keywords: polypropylene, α-Al_2O_3, mica, polymer composite, resistivity, electrical conductivity, temperature dependence, ionizing radiation, radiation modification

1. Introduction

Polymer composite materials are widely used in modern electrical engineering, radio engineering, the cable industry, instrument manufacturing, and the development of radiation-resistant structural materials. The functional properties of these materials are determined not only by the nature of the polymer matrix but also by the type, concentration, and dispersity of the mineral fillers incorporated into it, as well as by the polymer–filler interfacial interaction [1], [2], [3].

Polypropylene (PP) is a thermoplastic polymer characterized by high electrical resistivity, low dielectric loss, reasonably high mechanical strength, and good processability. However, changes at the molecular level can occur in the structure of PP under the influence of rising temperatures and ionizing radiation [4], [5], [6], [7]. These changes affect the movement of charge carriers, the distribution of local energy levels, and, consequently, the electrical conductivity of the material.

The addition of mineral fillers to a polymer enables the targeted modification of the composite's electrical properties. α-Al_2O_3 is of particular interest as an oxide material with high electrical resistance, while mica is notable as a mineral filler distinguished by its layered structure and superior thermal and electrical insulation properties [8], [9], [10].

In such systems, the transport of electric charge depends not only on processes occurring within the bulk of the polymer matrix but also on those taking place at the interface between the polymer and filler phases. Therefore, studying the electrical resistance of the composite under temperature and irradiation conditions is of great importance for evaluating its structure and functional properties [11]. The aim of this work is to determine the effect of mineral filler concentration and ionizing radiation dose on the temperature dependence of the electrical resistivity of PP/α-Al_2O_3 and PP/mica composites.

2. Experimental Procedure

Composites based on a polypropylene matrix were used as the object of study. α-Al_2O_3 and mica were used as mineral fillers in the preparation of the composites [12].

The following compositions were considered for comparison:

- ilkin PP; initial PP
- PP + 20% α-Al_2O_3;
- PP + 40% α-Al_2O_3;
- PP + 20% mica;
- PP + 40% mica.

The electrical properties of the samples were investigated under various temperature conditions. As shown in the graphs, the temperature range was approximately 298÷480 K. The decimal logarithm of resistivity for evaluating the temperature dependence of electrical resistance:

$$lg\rho = f(T)$$

It is presented in the form of. Here, ρ is the electrical resistivity (Ω·m), and T is the absolute temperature (K). Radiation doses of 50 and 80 kGy were used to determine the effect of exposing the samples to ionizing radiation. The obtained results were compared with the initial PP sample, and the effect of the type and concentration of the mineral filler was evaluated separately [13-14].

Analysis of the results:

Electrical resistance of PP/α-Al_2O_3 and PP/mica composites after 50 kGy irradiation.

The lgρ=f(T) dependence for samples irradiated at a dose of 50 kGy is shown in Figure 1.

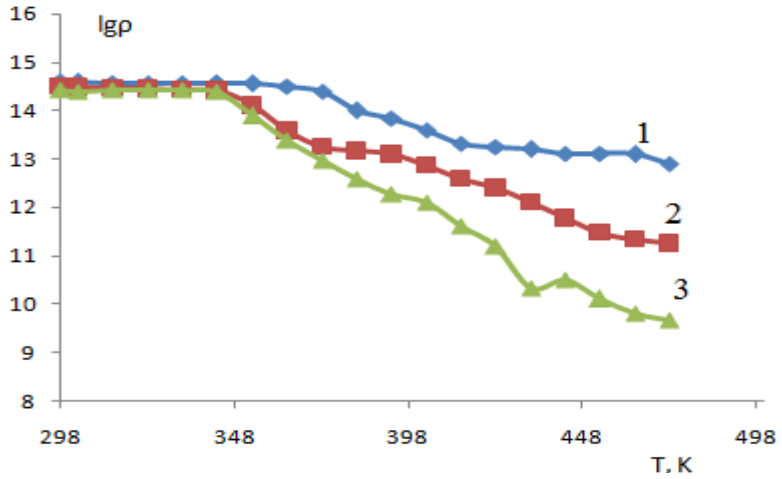


Figure 1. Temperature dependence of resistivity after 50 kGy irradiation, lgρ=f(T): 1 – pristine PP; 2 – PP + 20% α-Al_2O_3; 3 – PP + 20% mica.

As can be seen from Figure 1, lgρ decreases with increasing temperature in all the samples studied. However, the rate of this decrease varies depending on the composition of the samples. In the initial PP sample, the decrease in lgρ as the temperature rises from 298 K to approximately 480 K is relatively slight. In the initial

sample, the retention of a high resistivity value can be attributed to the preservation of the polypropylene matrix's high electrical insulation capability.

When 20% α-Al_2O_3 is added to PP, the temperature dependence of the resistivity becomes more pronounced. As the temperature rises, log ρ decreases from a level of approximately 14,4÷14,5 to 11,2÷11,3.

In the composite with 20% mica added, however, this change is more pronounced. As the temperature rises, lgρ decreases from a level of approximately 14,4 to a level of 9,6÷9,7. Thus, at the same filler concentration, the mica-modified PP sample exhibits higher sensitivity in terms of the change in specific resistance in response to temperature [15], [16].

This result can be attributed to the thermal activation of charge carriers within the polymer matrix and at the polymer–mineral interface. As the temperature rises, the increase in the kinetic energy of charge carriers facilitates their passage over local potential barriers; consequently, electrical conductivity increases while resistivity decreases.

Effect of α-Al_2O_3 concentration

To more clearly evaluate the effect of the α-Al_2O_3 concentration, the results for the composite containing 40% α-Al_2O_3 are presented in Figure 2.

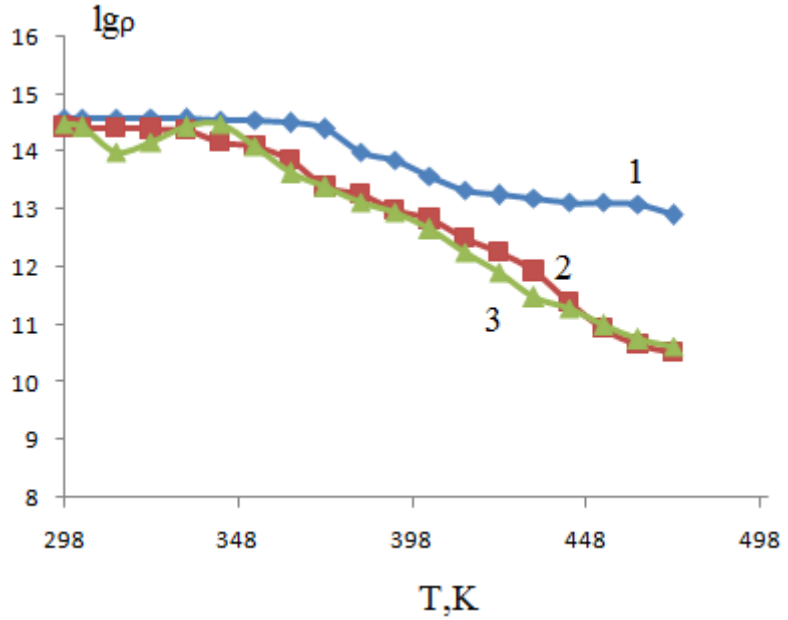


Figure 2. Temperature dependence of resistivity, lgρ=f(T), after 50 kGy irradiation: 1 – pristine PP; 2 – PP + 40% α-Al_2O_3; 3 – PP + 20% mica.

Figure 2 compares the temperature dependencies of virgin PP and composites containing 40% α-Al_2O_3 and 20% mica. With the incorporation of 40% α-Al_2O_3, the decrease in resistivity with rising temperature becomes more pronounced compared to the sample containing 20% α-Al_2O_3. This phenomenon can be explained by the expansion of the polymer–filler interfacial area resulting from the increased filler concentration, and by the formation of additional local energy levels within the composite's microstructure that influence the movement of charge carriers.

As is known, α-Al_2O_3 is a material with high electrical resistance. It is impossible to explain the effect of such a material—characterized by high electrical resistance—solely based on the principle of "increasing interphase conductivity." The principle of "enhancing interphase conductivity" in composites relates to the processes occurring within the system comprising the polymer matrix, mineral particles, and the interphase boundaries between them. Thus, it is based on the interaction at their interphase boundary [17]. Therefore, increasing the number of α-Al_2O_3 particles alters the temperature dependence of the new composite's electrical properties. As a result, a change in the temperature dependence can lead to an increase in the material's temperature sensitivity.

Processes occurring in the electrical properties of composites under 80 kGy irradiation

The results obtained for the composite after an irradiation dose of 80 kGy are shown graphically in Figure 3.

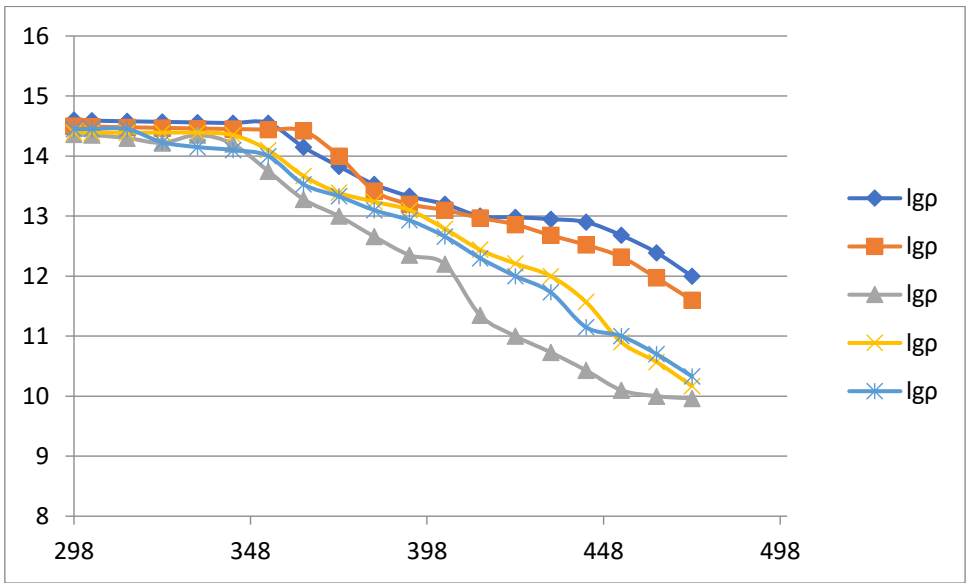


Figure 3. Temperature dependence of resistivity after 80 kGy irradiation, lgρ=f(T): 1 – pristine PP; 2 – PP + 20% α-Al_2O_3; 3 – PP + 20% mica; 4 – PP + 40% α-Al_2O_3; 5 – PP + 40% mica.

The temperature dependence of the electrical resistance of five composite samples with different compositions is shown in Figure 3. At the same time, the temperature dependence of the composite samples' electrical resistance is presented in the form of a comparative graph. The initial polypropylene sample exhibits higher lgρ values across all specified temperature ranges. Within the specified temperature range (450–470 K), the resistivity of polypropylene remains around 13 units. The obtained results confirm that polypropylene possesses high electrical insulation properties. After the incorporation of nanoparticles, the resistivity of the resulting composites decreases more rapidly with increasing temperature. A sudden increase in the specific resistance of the composite was observed in the composite containing 20% mica. In the samples examined, the value of resistivity approaches the level of approximately 10 units at very high temperatures. However, in composites containing 40% α-Al_2O_3 and 40% mica, a significant decrease in resistivity with increasing temperature is observed. Thus, by varying the concentration and composition of the nanoparticles, it is possible to significantly influence the temperature-electrical characteristics of the resulting composite [18].

The obtained composite sample was subsequently subjected to a radiation dose of 80 kGy. The results obtained and the changes observed in the graphs aroused considerable interest. So, it turns out that radiation can have a beneficial effect on the molecular structure of the polymer. Thus, it confirms the possibility of the formation of radical centers, structural defects, and new local energy states in the chain of the high-molecular-weight polymer as a result of 80 kGy of radioactive radiation. The radical centers that have formed can participate in the capture and release of charge carriers.

Now, let us look at the comparison of all composite systems after 50 kGy irradiation

The temperature dependencies of all the investigated composites mentioned above were determined following 50 kGy irradiation and are presented graphically in Figure 4.

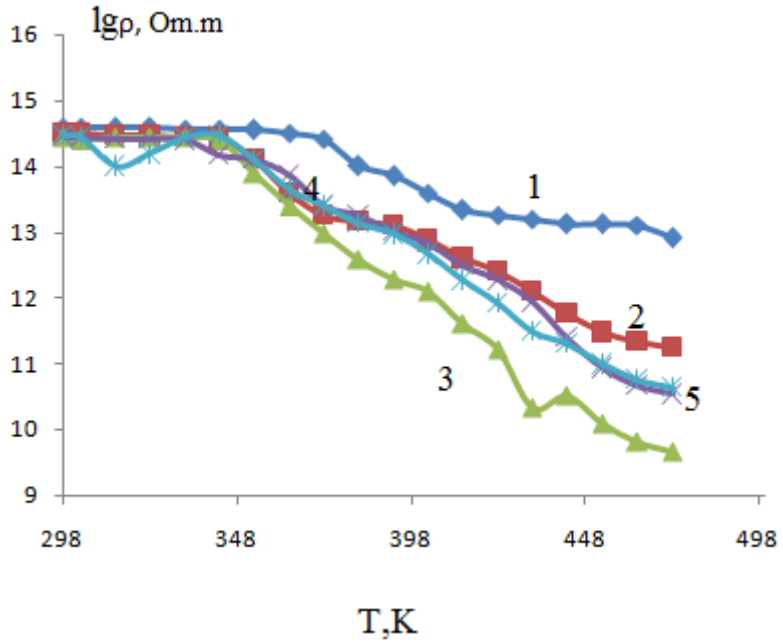


Figure 4. Temperature dependence of resistivity after 50 kGy irradiation, lgρ=f(T): 1 – pristine PP; 2 – PP + 20% α-Al_2O_3; 3 – PP + 20% mica; 4 – PP + 40% α-Al_2O_3; 5 – PP + 40% mica.

Figure 4 shows that the general trend for all samples is a decrease in resistivity with rising temperature. At the same time, the slope of the curves depends significantly on the composition of the composite. The initial PP maintains the highest electrical resistance. In this sample, lgρ gradually decreases as the temperature rises, reaching a value of approximately 13 units in the high-temperature range. The addition of α-Al_2O_3 and mica intensifies the effect of rising temperature on electrical resistance. In particular, the curve for the composite containing 20% mica shows a steeper downward trend.

The graphs also show that, in the high-temperature range, the resistivity values of the filled composites tend to converge. This can be attributed to the dominance of thermal activation processes involving charge carriers in composites of varying compositions under the influence of temperature.

Physical explanation of temperature dependence.

A thermally activated conduction model can be applied to analyze the temperature dependence of specific resistance in polymer composites:

$$\rho = \rho_0 \exp\left(\frac{E_a}{kT}\right),$$

Here, ρ_0 is a constant depending on the material's structure, E_a is the effective activation energy, k is the Boltzmann constant, and T is the absolute temperature.
As a result of taking the logarithm of this expression:

$$\ln \rho = \ln \rho_0 + \frac{E_a}{kT}$$

or for the common logarithm:

$$lg\rho = lg\rho_0 + \frac{E_a}{2.303kT}$$

is obtained.

This relationship indicates that as the thermal activation of charge carriers intensifies, the rise in temperature leads to a decrease in resistivity. In the investigated PP-based composites, the polymer–filler interface is presumed to exert a significant influence on this process in addition to other factors. The generation

of local electric potentials on the surface of mineral particles and in the zone of their contact with the polymer matrix can alter the trajectories of charge carriers.

Combined effect of radiation and filler concentration

An important feature of the obtained results is that the electrical properties of the composite are determined not only by temperature but also by the radiation dose and the concentration of the mineral filler.

Under the influence of ionizing radiation, the following structural processes may occur in PP:

1. formation of radical centers in polymer macromolecules;
2. development of chain scission or cross-linking processes;
3. formation of local energy levels;
4. formation of charge-trapping centers at the polymer–filler interface;
5. Change in the movement mechanism of the load carriers.

The direction and intensity of these processes depend on both the radiation dose and the structure of the composite. The addition of a mineral filler introduces additional interphase boundaries into the system. Therefore, the change in electrical properties in the samples with 20% and 40% filler content differs significantly from that of the virgin PP.

In mica-based composites specifically, the more rapid decrease of lgρ with rising temperature can be attributed to the influence of the material's layered structure and the local electric fields generated at the polymer–mineral interface on charge transport processes. However, to precisely confirm this mechanism, it is advisable to employ dielectric spectroscopy, thermally stimulated current measurements, or a separate calculation of the activation energy.

3. Conclusion

The following key results were obtained during the studies mentioned in the article:

First of all, it should be noted that for each of the PP, PP/α-Al_2O_3, and PP/mica composites, the value of specific resistance decreases as the temperature rises. This indicates that as the temperature rises, there is a significant increase in the number of charge carriers activated by the temperature. For this indicator, the value of the specific resistance remains constant in the initial PP sample, regardless of the increase in the temperature range. As is known, the electrical insulation properties of polypropylene material are very high. However, the addition of α-Al_2O_3 to this material alters the temperature dependence of the electrical resistivity in the new composite. At the end of the study, we increased the filler concentration from 20% to 40%. Increasing the concentration reduces the value of lgρ, as does increasing the temperature.

Unlike α-Al_2O_3, in composite samples containing mica-based filler, the value of resistivity changes more sharply as the temperature decreases. This characteristic can be attributed to the layered structure of the mica particles and the charge transport processes occurring at the polymer–filler interface.

Irradiation doses of 50 kGy and 80 kGy have a noticeable effect on the electrical properties of the composites. The effect of irradiation may be attributed to the formation of structural defects and local energy states within the polymer matrix.

The obtained results indicate that the electrical resistance of α-Al_2O_3- and mica-filled PP composites is a function of their composition, temperature, and radiation dose. Among the systems studied, pristine PP retains its high electrical insulation capability better, whereas mineral-filled composites exhibit greater electrical sensitivity to temperature changes. To control the electrical properties of PP/mineral filler systems, not only the type of filler but also the filler concentration, radiation dose, and temperature regime must be considered together. Research results indicate that the temperature dispersion of the electrical resistance of PP-based composites is determined by the interaction of localized energy states formed at the polymer-mineral interface, alongside thermally activated charge transport processes within the polymer matrix. The incorporation of α-Al_2O_3 and mica fillers alters the microstructure of the composite, thereby affecting the temperature coefficient of electrical resistance. Irradiation further complicates this structure-functional relationship, creating

conditions for the formation of new charge-trapping and charge-transport centers within the polymer's molecular structure.

In this regard, PP/α-Al_2O_3 and PP/mica composites can be considered promising systems for the development of functional insulating materials suitable for use under conditions where electrical and radiation effects coexist.

Author Contributions

The author contributed to the conception, design, analysis, interpretation, and preparation of the manuscript and approved the final version.

Funding

No funding was received for this research.

Conflicts of Interest

The author declares no conflict of interest.

Acknowledgment

Not applicable.

References

[1] Liu W, Cheng L, Li S. Review of electrical properties for polypropylene based nanocomposite. Composites communications. 2018 Dec 1;10:221-5. https://doi.org/10.1016/j.coco.2018.10.007

[2] Vila F, Dhima P, Mandija F. The influence of temperature on the electrical resistivity of the cellular polypropylene and the effect of activation energy. SpringerPlus. 2013 Sep 18;2(1):472. https://doi.org/10.1186/2193-1801-2-472

[3] Chand N., Sharma J. Effect of nanoalumina particles on dielectric behavior of polypropylene // *Journal of Nanostructured Polymers and Nanocomposites*. – 2011. – Vol. 7, No. 4.

[4] Farzaneh S, Tcharkhtchi A. Viscoelastic properties of polypropylene reinforced with mica in Tα and Tαc transition zones. International Journal of Polymer Science. 2011;2011(1):427095. https://doi.org/10.1155/2011/427095

[5] Mittal P, Naresh S, Luthra P, Singh A, Dhaliwal JS, Kapur GS. Polypropylene composites reinforced with hybrid inorganic fillers: Morphological, mechanical, and rheological properties. Journal of Thermoplastic Composite Materials. 2019 Jun;32(6):848-64 https://doi.org/10.1177/0892705718785674

[6] Xie Z, Liu D, Xiao Y, Wang K, Zhang Q, Wu K, Fu Q. The effect of filler permittivity on the dielectric properties of polymer-based composites. Composites Science and Technology. 2022 May 3;222:109342. https://doi.org/10.1016/j.compscitech.2022.109342

[7] Abdel-Hamid HM. Effect of electron beam irradiation on polypropylene films—dielectric and FT-IR studies. Solid-state electronics. 2005 Jul 1;49(7):1163-7. https://doi.org/10.1016/j.sse.2005.03.025

[8] Suljovrujic E, Stojanovic Z, Dudic D, Milicevic D. Radiation, thermo-oxidative and storage induced changes in microstructure, crystallinity and dielectric properties of (un) oriented isotactic polypropylene. Polymer Degradation and Stability. 2021 Jun 1;188:109564. https://doi.org/10.1016/j.polymdegradstab.2021.109564

[9] Suljovrujic E, Trifunovic S, Milicevic D. The influence of gamma radiation on the dielectric relaxation behaviour of isotactic polypropylene: The α relaxation. Polymer degradation and stability. 2010 Feb 1;95(2):164-71. https://doi.org/10.1016/j.polymdegradstab.2009.11.034

[10] Suljovrujic E. Gel production, oxidative degradation and dielectric properties of isotactic polypropylene irradiated under various atmospheres. Polymer degradation and stability. 2009 Apr 1;94(4):521-6. https://doi.org/10.1016/j.polymdegradstab.2009.01.029
[11] Mathakari NL, Bhoraskar VN, Dhole SD. MeV energy electron beam induced damage in isotactic polypropylene. Nuclear Instruments and Methods in Physics Research Section B: Beam Interactions with Materials and Atoms. 2008 Jun 1;266(12-13):3075-80. https://doi.org/10.1016/j.nimb.2008.03.165
[12] Liu B, Gao Y, Guo C, Li J, Chen Y, Gao J, Du B. Effect of gamma-ray irradiation on electrical conductivity of polypropylene composite for nuclear cable insulation. High Voltage. 2025 Apr;10(2):470-9. https://doi.org/10.1049/hve2.70002
[13] Suraci SV, Fabiani D. Radiation-Induced Degradation in Polymeric Materials: Alterations in Physical–Chemical Properties and Their Effects on Electrical Performance of Insulation Systems. High Voltage. 2026 Feb;11(1):150-69. https://doi.org/10.1049/hve2.70071
[14] Zhang L, Chen Y, Wang Z, Lu Z, Xing Z, Guo S, Du H, Du BX, Xiao M. Long-Term Thermal Stability of Electron-Beam-Irradiation-Crosslinked Polypropylene Films for Power Capacitors. Electrical Materials and Applications. 2026 Jan;3(1):e70031. https://doi.org/10.1049/ema3.70031
[15] Bao Z, Du X, Ding S, Chen J, Dai Z, Liu C, Wang Y, Yin Y, Li X. Improved working temperature and capacitive energy density of biaxially oriented polypropylene films with alumina coating layers. ACS Applied Energy Materials. 2022 Mar 2;5(3):3119-28. https://doi.org/10.1021/acsaem.1c03735
[16] Lee CY, Chang CW. Dielectric constant enhancement with low dielectric loss growth in graphene oxide/mica/polypropylene composites. Journal of composites science. 2021 Feb 8;5(2):52. https://doi.org/10.3390/jcs5020052
[17] Chen H, Wang Y, Zhang W, Nan Y, Yue X, Zhang Y, Fan H. Effect of Al2O3 and BN compounding on thermal and mechanical properties of PP composites. Materials Today Communications. 2023 Dec 1;37:107300. https://doi.org/10.1016/j.mtcomm.2023.107300
[18] Li SK, Li WP, Shi XN. Simulation and optimization of thermal conductivity and dielectric properties of alumina/polypropylene composites. Insulating Materials. 2025;58(1):20-8.

Journal of Nanotechnology and Innovative Materials

Research Article

Nanoengineered Material Architecture for Improved Durability and Sealing of Bidirectional Two-Way Ball Valves in Waxy Particle-Laden Oil Pipelines

Tatyana Huseynova

Department of Industrial Engineering, Azerbaijan State Oil and Industry University, Baku, Azerbaijan

Received: 05.08.2026 Accepted: 26.09.2026 Published: 12.10.2026
https://doi.org/10.54414/PQOZ1595

Copyright: © 2026 by the authors. Licensee: Journal of Nanotechnology and Innovative Materials, Western Caspian University, Baku, Azerbaijan. This article is an open-access article distributed under the terms and conditions of the Creative Commons Attribution 4.0 International License (CC BY 4.0).

Abstract

Two-way ball valves used in oil and gas pipelines are exposed to a coupled damage system rather than to a single wear mechanism. Local jets during throttling promote cavitation and particle erosion; repeated opening and closing produce adhesive and abrasive wear at the ball seat interface; elastic and viscoelastic deformation alters bidirectional contact pressure; and wax accumulation can increase actuation torque or prevent complete seating. This paper develops a functionally zoned nanoengineered material architecture for a trunnion-mounted two-port ball valve that must isolate pressure from either direction. The architecture does not assume that one nanomaterial can protect every component. Instead, each damage zone is assigned a candidate system and a separate verification route. A dense polished micro nano structured WC–10Co–4Cr coating is proposed as the lead option for the ball sealing band and metallic scraper ring. Duplex nitriding with diamond-like carbon and CrN or CrCN thin films are retained as comparators where a thin low-friction surface is preferable. Graphene nanoplatelet PEEK and hBN PEEK are proposed for controlled screening as primary seat materials, while graphene-modified FKM is considered for the secondary elastomeric seal. A graphene oxide phytic acid film is included only as an exploratory antiwax treatment for protected noncontact flow surfaces. Two noninterchangeable validation envelopes are defined: a field screening line with an 89 mm bore, 0.6 to 1.2 MPa pressure, 50 to 60 °C temperature, 250 m³ per day flow, 2 to 5 percent wax and 132 mg per litre solids; and a DN500 PN100 structural qualification valve with a differential pressure up to 10 MPa. The proposed methodology couples transient CFD, nonlinear contact FEA, coating and polymer coupon tests, wax deposition experiments, and bidirectional valve cycling. Published coupon and valve data motivate the candidate materials, but no unmeasured valve-level performance is claimed. The principal contribution is a falsifiable selection framework that connects hydraulic damage maps and seat contact pressure to material zoning and qualification decisions.

Keywords: ball valve, nanocomposite WC–CoCr, PEEK fluoroelastomer, cavitation erosion, wax deposition, bidirectional sealing

Highlights

- A damage-driven five-zone nanoengineered architecture is proposed for a bidirectional two-way ball valve
- Micro nano WC–10Co–4Cr is selected as the lead hard coating for the ball sealing band and scraper ring
- Graphene PEEK and graphene FKM are treated as screening candidates that require creep aging and leakage qualification
- An antiwax graphene oxide film is restricted to protected noncontact surfaces and is not placed on the sealing band
- Field screening and DN500 PN100 structural qualification conditions are maintained as separate evidence envelopes

1 Introduction

A two-way ball valve is a two-port shutoff device in which a bored spherical obturator rotates between open and closed positions. In the present study, the term bidirectional describes the isolation requirement: the

closed valve must retain pressure when either pipeline side is pressurized. This distinction is important because hydraulic symmetry does not guarantee mechanical symmetry. Seat springs, pressure-energized cavities, support ring stiffness, machining tolerances, and friction can create different contact pressure fields for the two pressure directions. Pipeline valve design and qualification are governed at system level by API Specification 6D and its ISO supplement ISO 14313, while the present material study adds a damage-focused layer to those requirements [1], [2].

The dissertation problem addressed here is the improvement of two-way ball valve construction for oil and gas pipelines. Earlier stages of the work identified two coupled design objectives. The first is hydraulic: the port and cavity geometry should suppress unnecessary separation, recirculation, local velocity amplification, cavitation susceptibility, and transient pressure loading. The second is tribological and structural: the seat support system should maintain an adequate but not excessive contact pressure, limit concentrated stress, and preserve sealing after repeated cycling. Large ball valve simulations show that closure angle strongly reorganizes the jet and wake, while finite element investigations of bidirectional seats identify the support ring and geometric discontinuities as critical stress zones [3], [4], [5]. Consequently, geometry, preload, and surface engineering must be optimized together.

Conventional material selection often treats the valve as a uniform corrosion and wear problem. That approach is inadequate for a waxy particle-laden service. The ball sealing band experiences high Hertzian-type contact, sliding, and third-body abrasion. The scraper ring encounters deposits and entrained solids. The PEEK primary seat is sensitive to temperature-dependent modulus, creep, transfer film formation, and damage at its leading edge. The FKM secondary seal must resist swelling, gas decompression, and compression set. Protected bore surfaces may accumulate wax but carry little sealing contact. These zones require different combinations of hardness, toughness, low friction, chemical stability, compliance, and surface energy.

Nanoengineered materials can change these combinations through a refined carbide distribution, nanoscale multilayers, solid lubricant platelets, or tortuous diffusion paths. Their use is nevertheless not automatically beneficial. A hard coating with inadequate toughness can crack; a thin film can detach from an insufficiently supported substrate; graphene agglomeration can create leak paths or reduce polymer elongation; and an antiwax film can be removed by particles. A recent high-pressure ball valve failure investigation is especially instructive: coating spallation generated hard debris that intensified third body abrasion, whereas a redesigned seat combined with nitriding and a diamond-like carbon surface endured substantially more cycles in that specific test programme [6]. This evidence supports an interface system approach rather than a catalogue-based choice of fashionable materials.

The objective of this paper is therefore to formulate a research-ready nanoengineered architecture for the dissertation valve, rank the candidate systems, define their permitted locations and establish a validation sequence. The paper is deliberately written as a design and experimental framework. Literature values are used to justify screening decisions, but they are not transferred directly into predicted valve life or leakage. The hypotheses are intended to be tested under the actual contact pressures, fluid composition, temperature, and cycling history of the valve.

2 Valve Architecture and Operating Envelopes

2.1 Reference construction

The reference construction is a trunnion mounted full bore valve with two independently loaded seats. Each side uses a metallic scraper element, a PEEK primary sealing member, and an FKM O-ring as the secondary seal. The trunnion arrangement transfers pressure-induced ball force to the bearings and body instead of relying on seat support alone. For bidirectional isolation, both seat assemblies must tolerate the high-pressure and low-pressure roles. The nanomaterial concept preserves this architecture and changes only selected surfaces or formulations, which makes comparison with the qualified baseline possible.

Figure 1 shows the proposed functional zoning. WC–10Co–4Cr is placed on the metallic sealing and scraping zones because they require a thick load-bearing barrier against abrasion and cavitation. The primary polymer seat and secondary elastomer remain compliant elements and are modified through low-concentration nanofillers rather than through brittle surface layers. The antiwax coating is physically separated from the sealing band. DLC and CrN-based systems are comparators, not additional layers automatically stacked over

WC–CoCr. This prevents an unsupported coating hierarchy and permits adhesion failure to be evaluated independently.

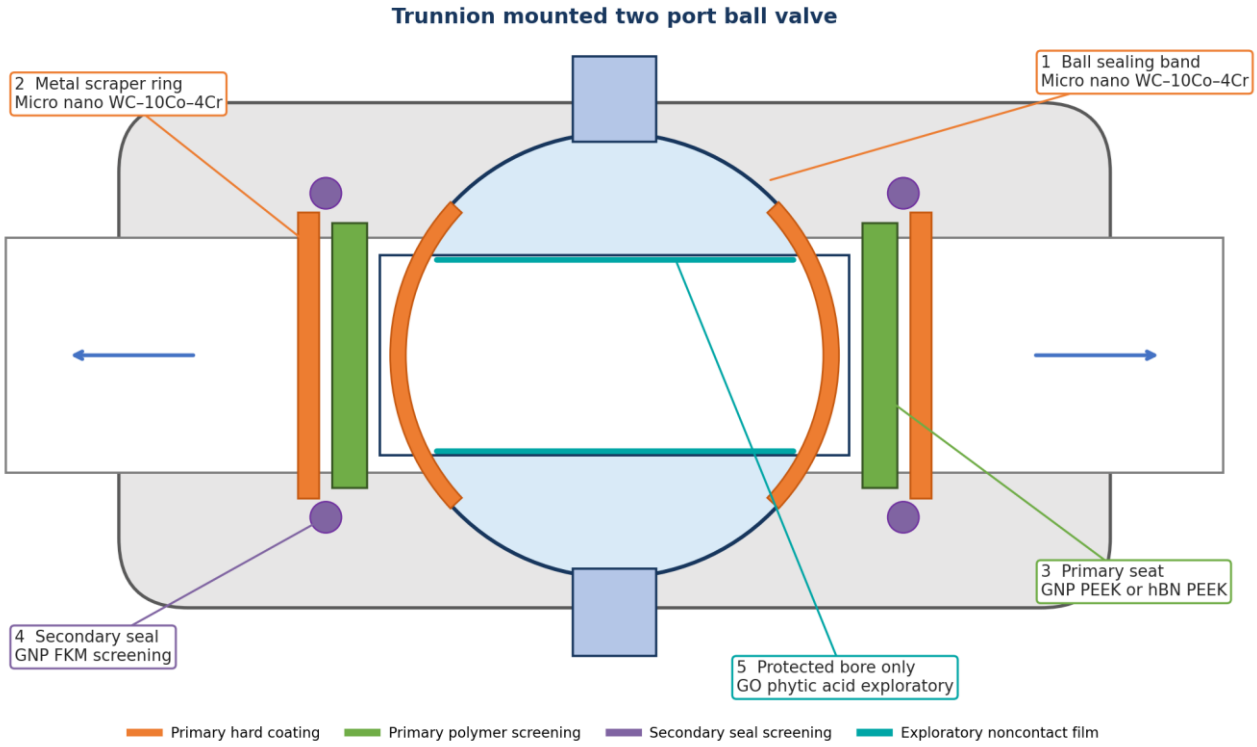


Figure 1 Functionally zoned material architecture for the reference two-way ball valve.

2.2 Separate validation envelopes

Two sets of operating information have been developed during the dissertation and must not be merged into one artificial duty point. Envelope A is a representative produced fluid line used to screen hydraulic behaviour, wax deposition and particle effects. Envelope B is the structural and sealing qualification case for a large valve. The 10 MPa differential pressure of Envelope B must not be assigned to the 89 mm line unless a future project specification explicitly does so. Table 1 preserves this separation.

Table 1 Noninterchangeable operating envelopes used in the proposed research programme.

Parameter	Envelope A	Envelope B
Purpose	Field and flow screening	Structural and sealing qualification
Nominal size	Pipe internal diameter assumed as 89 mm for preliminary calculation	DN500 trunnion-mounted ball valve
Pressure	0.6 to 1.2 MPa line pressure	PN100 class with differential pressure up to 10 MPa
Temperature	50 to 60 °C	To be applied at the specified design and test temperatures
Volumetric flow	250 m³ per day	Qualification flow to be defined by the valve test rig
Fluid density	Approximately 880 kg per m³	Test medium density defined for each hydraulic case
Wax content	2 to 5 percent by the stated field basis	Not automatically transferred to structural pressure tests
Entrained solids	132 mg per litre	Dedicated erosion concentration and size distribution required

Parameter	Envelope A	Envelope B
Seat package	Used to select representative fluids and deposits	Metal scraper, PEEK primary seat, FKM secondary O-ring
Open bore velocity	Approximately 0.465 m per second when 89 mm is the flowing diameter	Not inferred from Envelope A
Open item	Previously supplied oil and water viscosity values require confirmation of units and test temperature	Allowable stresses, leakage class and cycle count require project specification

For Envelope A, converting 250 m³ per day gives a flow rate of approximately 0.00289 m³ per second. Division by the area of an 89 mm circular bore gives an average full open velocity near 0.465 m per second. This average does not exclude damaging local flow. During partial closure, the effective flow area contracts sharply and the jet velocity can become many times greater than the pipe average. Cavitation assessment must therefore use the local pressure and velocity fields rather than a single full bore number.

3 Coupled Failure Mechanisms and Quantitative Indicators

3.1 Hydraulic loss, cavitation, and particle erosion

The pressure loss coefficient provides a geometry-normalized comparison of port shapes and opening angles. With a consistent reference velocity and density, it is defined by Equation 1. A lower value in the fully open position is desirable, but minimizing loss alone is insufficient because a narrow high-speed jet can shift damage to the seat edge or body cavity.

$$K = \frac{\Delta p}{\frac{1}{2}\rho U^2} \quad (1)$$

Cavitation risk is screened using the local cavitation number in Equation 2, where the reference pressure must be stated, and the vapour pressure must correspond to fluid composition and temperature. Multiphase produced fluids require sensitivity analysis because dissolved gas and light hydrocarbons change inception behaviour. A CFD cavitation model should be used to rank designs, followed by an erosion test; it should not be treated as an exact life predictor.

$$\sigma = \frac{p_{\mathrm{ref}} - p_v}{\frac{1}{2}\rho U^2} \quad (2)$$

Particle erosion depends on impact velocity, incidence angle, particle size and shape, concentration, and the target material response. In a closing valve, the highest velocity does not necessarily coincide with the highest erosion because the impact direction and residence time differ around the upstream seat, ball edge, and downstream cavity. A Lagrangian particle model can identify candidate hot spots, but its erosion coefficients must be calibrated with representative solids.

3.2 Contact pressure wear and leakage

A bidirectional seat must maintain a continuous contact band under pressure applied from either side. Li et al. found that high stress developed around the seat support ring and sharp corners in a large fully welded ball valve, and that the effective contact region changed at low pressure [3]. The useful design variable is therefore not only peak contact pressure but its minimum value, circumferential variation, and position relative to the fluid boundary. Equation 3 defines a coefficient of variation for the nodal contact pressure values within the intended sealing band.

$$CV_p = \frac{\mathrm{SD}(p_c)}{\mathrm{mean}(p_c)} \quad (3)$$

The seal design must satisfy both sides of Equation 4. The minimum local pressure must exceed the pressure-assisted sealing requirement with an appropriate project safety factor, while the maximum pressure must remain below the temperature- and medium-dependent allowable contact stress of the seat system. Excess preload can reduce leakage initially but increases torque, polymer creep, and coating damage.

$$p_{c,\min} \geq S_p \Delta p \quad ; \quad p_{c,\max} \leq p_{\mathrm{allow}}(T, \mathrm{medium}) \quad (4)$$

Wear results should be normalized by load and sliding distance only when the wear mechanism and contact geometry make that comparison meaningful. The specific wear rate in Equation 5 is suitable for coupon screening, while valve-level assessment should use loss of sealing geometry, leakage, and torque.

$$k_s = \frac{V_w}{F_N s} \quad (5)$$

3.3 Wax deposition and incomplete seating

Wax affects the valve in three ways. It changes the effective roughness and flow area, increases the force required to scrape the ball, and can become trapped at the seat interface. Laboratory studies demonstrate that surface roughness and alloy type can alter wax deposit thickness and mass, but the direction and magnitude depend on thermal conditions and oil composition [7],[8]. The antiwax problem must therefore be tested under controlled wall temperature, bulk temperature, shear rate, cooling history, and water fraction. A low adhesion flow surface is valuable only if it remains attached and does not contaminate the seal.

Table 2 Damage zones, candidate material systems and principal qualification risks.

Valve zone	Dominant damage	Candidate system	Selection rationale	Main risk to disprove
Ball sealing band	Sliding contact, particles, local cavitation, corrosion	Polished micro nano WC–10Co–4Cr by HVOF or fine feedstock HVAF	Dense load-bearing carbide network and documented valve coating practice [9], [10],[11], [12].	Residual stress, carbide dissolution, pores, edge cracking, finish-induced leakage
Ball sealing band comparator	Low friction sliding and repeated cycling	Nitrided substrate plus DLC as one duplex system	Ball valve cycle evidence and low friction potential [6], [13].	Thin film support adhesion pinholes debris after spallation
Thin film comparator	Adhesive wear and corrosion-assisted cavitation	CrN or CrCN	Hard protective film with measurable cavitation response [14].	Brittle cracking, substrate deformation, coating thickness sensitivity
Metal scraper ring	Deposit cutting, particle abrasion, edge loading	Micro nano WC–10Co–4Cr with a controlled edge radius	Hardness plus fracture toughness and established thermal spray processing [9], [10], [11], [12].	Chipping at sharp edge, excessive counterface wear
Primary PEEK seat	Creep, transfer film, abrasion, thermal expansion	Low-loading GNP PEEK as lead screen; hBN PEEK or WS_2 PEEK as comparators	Graphene and solid lubricant fillers can modify friction, wear, and thermal transport [15], [16], [17].	Agglomeration reduced ductility; leakage paths altered creep and recovery
Secondary FKM O-ring	Swelling, compression set, tear, permeation, gas decompression	Dispersed graphene nanoplatelet FKM	Graphene-filled FKM studies report improved mechanical and barrier related performance [18], [19].	Poor dispersion, hardening, reduced elongation, unverified rapid gas decompression resistance

Valve zone	Dominant damage	Candidate system	Selection rationale	Main risk to disprove
Protected bore and cavity	Wax nucleation and adhesion	GO phytic acid film as exploratory treatment	Strong coupon-level wax inhibition reported in water containing waxy oil [20].	Abrasion durability adhesion water fraction dependence chemical stability
Stem and trunnion journals	Fretting boundary lubrication corrosion	DLC or CrN-based thin film after substrate hardening	Low friction comparator for supported contacts [13], [14].	Edge delamination and dimensional tolerance change

4 Candidate Nanoengineered Material Systems

4.1 Micro nano WC CoCr for metallic sealing zones

WC–CoCr is already used as a wear-resistant valve coating, so the research question is not whether the generic chemistry is hard. It is whether a controlled micro-nano or fine feedstock structure can provide the required combination of density, toughness, surface finish, and residual stress on the actual ball and scraper geometry. Bobzin et al. investigated fine feedstock HVAF coatings for valves with the aim of reducing post-processing. Their work used porosity and as-sprayed roughness as key process outputs and showed that powder route and spray parameters strongly affect electrochemical and mechanical performance [9]. This is directly relevant because grinding a large spherical surface is costly and can expose pores or introduce waviness.

Ding et al. compared micro nano and conventional WC–10Co–4Cr coatings in a sodium chloride cavitation test. The micro-nano coating had low reported porosity, and its steady cavitation erosion rate was about one-half of the conventional coating in that coupon test [10]. Hong et al. likewise studied a near nanostructured HVOF WC–10Co–4Cr coating in saline cavitation [11]. Huang et al. examined slurry erosion of a micro-nano WC–CoCr coating in NaCl medium [12]. Together, these studies justify prioritizing the micro-nano carbide system when cavitation and solids coexist, but they do not establish a valve service life. The coating must be sprayed on the actual substrate and heat-treatment conditions, then finished to a leakage-compatible surface and tested in rolling sliding seat contact.

Two process routes should be compared. HVOF is the reference route with the most direct micro-nano cavitation evidence. HVAF with fine feedstock is a near-net-shape route intended to reduce oxide formation and post-processing. The decision should be based on a multi-response window: porosity, carbide retention, hardness, fracture toughness, bond strength, residual stress, achievable spherical roughness, and leakage after cycling. A very high hardness result should not override visible edge cracking or low adhesion.

4.2 DLC and chromium nitride-based comparators

Diamond-like carbon offers low friction and chemical inertness but is usually much thinner than a thermally sprayed carbide coating. Cheng and Jiang found that DLC improved the cavitation erosion response of stainless steel, while delamination was governed by adhesion and coating defects [13]. For a valve, this means that DLC is most credible on a hard, well-supported substrate and in a contact that does not plastically deform. The 2026 ball valve investigation by Zhang et al. reinforces the point: their improved combination of substrate nitriding, DLC, and a modified seat geometry survived at least 7500 cycles without visible leakage under their stated high-pressure test, whereas the original coating system failed much earlier [6]. The result is promising but inseparable from the geometry and substrate changes.

CrN and CrCN are retained as comparators because they provide a metallic nitride-based alternative with different toughness and thermal stability. Cavitation research on CrN and CrCN indicates that hardness alone is not the best predictor; the H^3 over E^2 index, cracking response, and adhesion must be considered [14]. In this programme, DLC and CrN-based films should first be tested on small spherical or ring specimens manufactured from the actual ball and journal substrate. They should not be deposited over WC–CoCr without a separately engineered interlayer and adhesion study.

4.3 Graphene and solid lubricant modified PEEK

PEEK is attractive for the primary seat because it combines temperature capability, chemical resistance, and sufficient compliance for a polymer-assisted seal. Its weakness is not a single low material property but the interaction of creep, thermal expansion, edge stress, and abrasive wear. Graphene nanoplatelets can

improve stiffness, thermal transport, and tribological behaviour when they are dispersed and bonded effectively. Puértolas et al. studied the mechanical and tribological properties of graphene nanoplatelet PEEK composites and showed that filler loading changes both reinforcement and frictional response [15]. Kalin et al. compared graphene-, WS_2-, and carbon nanotube-filled PEEK, demonstrating that nanofiller type and test conditions determine the wear mechanism [16].

The lead screening family should therefore be neat PEEK and PEEK with 0.5, 1.0, and 2.0 mass percent graphene nanoplatelets. These levels are proposed design of experiment factors, not claimed optima. A separate hBN PEEK family should be studied because hBN can act as a solid lubricant and a thermal conductor without electrical conductivity. A hybrid carbon fibre and hBN literature system has shown low friction and wear in laboratory testing [17], but introducing fibres can make seat machining, anisotropy, and edge integrity more complex. It is preferable to qualify one filler family at a time before considering a hybrid.

Selection must include compression creep and recovery under the contact pressure histories obtained from FEA. A formulation that gives low pin-on-disk wear but develops excessive permanent set can lose the sealing band after pressure removal. Conversely, a stiffer formulation may reduce extrusion but require higher manufacturing precision and spring preload. The decisive test is bidirectional leakage after thermal aging and cycling, supported by profilometry and microscopy of the seat edge and transfer film.

4.4 Graphene-modified FKM for the secondary seal

The FKM O-ring is a secondary barrier and should not be used to compensate for inadequate primary seat contact. Graphene nanoplatelets can create a tortuous permeation path and reinforce an elastomer at modest loading. Liu et al. developed fluoroelastomer graphene nanocomposites for sealing applications, while Wei et al. studied graphene oxide-integrated fluoroelastomer after high-temperature petroleum oil exposure [18], [19]. These studies support screening but do not replace service qualification because filler dispersion, cure system, hardness, and oil composition can change swelling and compression set.

A practical formulation matrix is neat FKM plus 1, 3, and 5 parts graphene nanoplatelets per hundred parts rubber. The exact range should be adjusted after mixing torque and dispersion microscopy. Tensile strength, elongation, tear resistance, hardness, compression set, volume swell, decompression damage, and permeation should be measured before any valve assembly test. Where explosive or rapid gas decompression is credible, the compound and its manufacturing route should be qualified under the applicable project requirements, including NORSOK M 710 when specified [21].

4.5 Graphene oxide phytic acid film for protected antiwax surfaces

Tan et al. reported a one-step functionalized graphene oxide phytic acid coating with high wax inhibition in their waxy oil transportation experiment [20]. The proposed mechanism relied on a hydrated superhydrophilic and underwater oleophobic interface. That mechanism makes the water fraction a controlling variable. It may be valuable for a produced fluid that contains an aqueous phase, but it may not operate in dry oil and may be vulnerable to abrasive solids.

For this reason, the film is classified as exploratory and restricted to protected portions of the bore or cavity where contact stress is negligible. It is explicitly excluded from the ball seat sealing band, the scraper edge, and any surface that can shed particles directly into the interface. A cold finger or flow loop test should compare coated and uncoated substrates at 2 and 5 percent wax, multiple water fractions, and the stated solids concentration. Adhesion and surface chemistry must be remeasured after the erosion exposure.

5 Proposed Functionally Zoned Valve Design

The first prototype should use the smallest number of simultaneous material changes that can still test the zoning concept. The recommended lead configuration is a polished micro nano WC–10Co–4Cr coating on the ball sealing bands and metallic scraper surfaces, a low-loading graphene nanoplatelet PEEK primary seat selected from coupon and creep tests, and an FKM secondary seal selected from neat and graphene-modified compounds. The GO phytic acid film should be omitted from the first pressure qualification valve unless it has already passed a separate adhesion and particle erosion gate. This sequencing isolates causes when leakage or torque changes.

The hard coating should terminate outside the sharpest geometric transition and include a controlled edge radius. Coating allowance must be included in the ball diameter, seat interference, and final lapping plan. The seat support ring should be locally stiffened or radiused if FEA identifies the same stress concentration reported in large valve research [3]. Spring preload should be adjustable in the research prototype so that material effects can be separated from contact pressure. The scraper should remove deposits without forcing debris beneath the primary seat; a relief path or capture cavity should be included downstream of the scraper edge.

Material zoning is linked to the flow field. CFD hot spots on the downstream seat edge should be compared with the physical coating boundary. If a predicted cavitation or particle impact zone crosses from the coated ball to an unprotected substrate, the termination should move, or the geometry should be altered. Likewise, a low-velocity recirculation region that retains wax may justify a drainage or flushing feature before an antiwax surface treatment is considered. The material is therefore the last element of a chain that begins with port geometry and cavity management.

6 Integrated CFD FEA and Materials Selection Framework

6.1 Hydraulic model

The CFD programme should include fully open flow and a set of closing angles that resolve the rapid area contraction region. A practical sequence is 0, 15, 30, 45, 60, 75 and 82 degrees from fully open, with additional angles around the onset of the highest pressure gradient. Steady simulations can screen geometry, but transient closure is required to evaluate pressure waves and time-dependent vapour volume. The model should report pressure loss, minimum static pressure, cavitation volume fraction, wall shear stress, recirculation residence time, and particle impact statistics. Mesh independence must be demonstrated for both global pressure loss and local seat edge velocity.

The field envelope should be run at 50 and 60 °C with fluid property sensitivity. The earlier viscosity entries cannot be used until their units and reference temperatures are confirmed. A credible range should therefore be defined from laboratory rheometry of the oil water wax mixture. Particle size distribution, density, and angularity should also be measured rather than represented only by the concentration of 132 mg per litre. For cavitation, vapour pressure and dissolved gas assumptions should be documented.

6.2 Structural contact model

The nonlinear FEA model should include the ball, both seat rings, primary PEEK components, support rings, springs or preload elements, body stiffness and frictional contacts. Load steps should reproduce assembly preload, pressure from the left, depressurization, pressure from the right, and thermal stabilization. Outputs include minimum and maximum sealing band pressure, its circumferential coefficient of variation, seat deformation, support ring stress, ball displacement, and predicted actuation torque. Temperature-dependent elastic and viscoelastic properties are required for PEEK, while hyperelastic and time-dependent data are required for FKM if the O-ring is represented directly.

A wear update can be implemented after the contact model is validated. Archard-type wear may be used as a comparative numerical law, but its coefficient must be fitted to the same material pair, lubricant, and solids condition as the valve. Geometry should be updated in increments and the contact analysis repeated. The most useful output is the change in continuous sealing width and minimum pressure, not a visually impressive wear contour.

6.3 Evidence gates

Figure 2 organizes the evidence sequence. Each gate can reject a candidate before the next more expensive test. Coupon results provide constitutive data and failure modes; subcomponent tests reproduce curved contacts and edges; prototype testing measures bidirectional leakage and torque; qualification verifies compliance with the applicable valve standard. A material that fails adhesion or creep should not be rescued by proceeding directly to a full valve test.

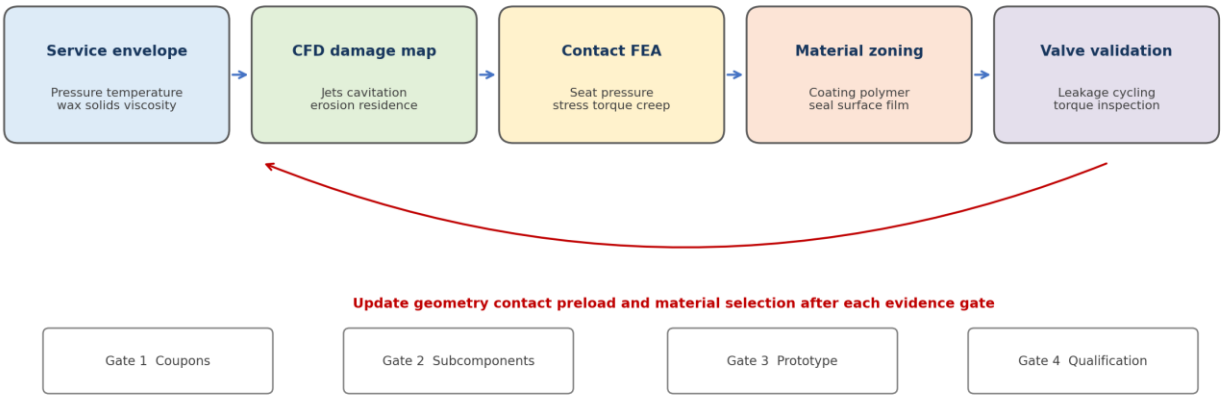


Figure 2 Integrated simulation material selection and evidence gate workflow.

7 Experimental Validation Programme

7.1 Specimen matrix and characterization

Table 3 gives a minimum screening matrix. Replicate count should be set through a power analysis after pilot scatter is known. All coated specimens should be manufactured in more than one spray batch so that the experiment does not confuse a material effect with one batch. Polymer plaques and machined seat segments should be conditioned under the same thermal history as the valve components.

Table 3 Proposed screening matrix with baselines and decision outputs

Component family	Candidate levels	Mandatory baseline	Primary outputs
Ball and scraper coating	Conventional WC–10Co–4Cr micro-nano HVOF fine feedstock HVAF	Qualified production coating or uncoated hardened substrate	Porosity, phases, hardness, toughness, adhesion, residual stress, roughness, cavitation, and slurry loss
Thin film comparator	Nitrided plus DLC CrN CrCN	Nitrided substrate without film	Scratch adhesion, pinholes, friction, edge delamination, cavitation damage
Primary seat	PEEK with 0, 0.5, 1.0, 2.0 mass percent GNP	Production grade neat PEEK	Dispersion modulus, creep recovery, thermal expansion, friction wear, leakage
Primary seat comparator	Neat PEEK and selected hBN or WS_2 PEEK levels	Same neat PEEK batch	Friction wear thermal conductivity machining integrity sealing recovery
Secondary seal	FKM with 0, 1, 3, 5 phr GNP	Qualified production FKM	Dispersion, cure, tensile tear, swelling, compression set, permeation, decompression damage
Antiwax surface	Bare alloy GO phytic acid film	Production bore finish	Contact angle, adhesion, deposit mass and thickness, particle erosion retention

Metallic coatings should be characterized by cross-sectional SEM and EDS, X-ray diffraction, image-based porosity, microhardness or nanoindentation, surface profilometry, and an adhesion method appropriate to coating thickness. Fracture toughness or an indentation crack resistance proxy should supplement hardness. The finished spherical surface must be measured for roughness, waviness, and roundness because a low coupon roughness does not guarantee a continuous sealing band on a large ball.

Polymer and elastomer nanocomposites require dispersion mapping. Optical or electron microscopy, Raman mapping where appropriate, density and thermal analysis should be related to mechanical performance.

PEEK tests should include compressive creep and recovery at 50 and 60 °C under FEA-derived pressure levels. FKM tests should include oil and brine aging, compression set, volume and mass change, hardness change, and microscopy after decompression.

7.2 Tribology cavitation and wax tests

The metallic coating tribometer should reproduce the coated ball against a seat or scraper counterface with representative contact pressure and small-amplitude sliding. Tests are required in base oil, oil with the representative aqueous phase, and oil with 132 mg per litre solids. Friction, wear volume, coating penetration, counterface wear, and debris morphology should be recorded. A test that reports only the wear of the coating can select a coating that destroys the softer seat.

Cavitation screening should begin with ASTM G32 vibratory testing and may be complemented by ASTM G134 cavitating jet testing [22], [23]. These standardized tests rank material resistance under controlled conditions; a valve flow loop is then required to reproduce the hydrodynamic jet, pressure recovery, and particle interaction. Mass loss, volume loss, incubation time and damage morphology should be compared at fixed intervals. Coating failure at the edge or substrate interface is a rejection event even when average mass loss is low.

Wax testing should use a cold finger or temperature-controlled flow loop with the actual or compositionally matched oil. At minimum, 2 and 5 percent wax levels should be crossed with water fraction and surface condition. Deposit mass, thickness, removal force, and residual film chemistry should be recorded. Surface roughness must be controlled because it independently changes wax deposition [7]. The coated specimen should then receive a solids erosion exposure, and the wax test should be repeated to determine whether the antiwax function survives.

7.3 Seat segment and full valve testing

A curved seat segment rig should bridge flat coupons and the DN500 valve. It should reproduce the ball radius, coating finish, seat edge, spring load, temperature, and contaminant exposure. The rig can measure breakaway friction, running friction, leak rate across a short sealing arc, and wear scar evolution. High-speed imaging or acoustic emission may help identify debris generation or coating cracking, but inspection after fixed cycle blocks remains essential.

The full valve sequence should include shell and seat tests, low- and high-pressure bidirectional leakage, torque measurement, thermal stabilization, repeated opening and closing, and periodic leakage checks. The direction of pressure should alternate in a defined sequence so that one seat is not always the upstream seat. After testing, the valve should be disassembled for surface profilometry, microscopy, and dimensional inspection. Fugitive emission performance of the stem sealing system should be tested to ISO 15848- 1 if it is within project scope [24]. Final acceptance remains subject to API 6D and ISO 14313 requirements and to the purchaser specification [1], [2].

Table 4 Decision metrics for progressing from screening to valve qualification

Gate	Progression criterion	Action if not met
Coating integrity	No through-coating cracks, edge chipping, or interface delamination after the specified test block	Reject candidate or modify substrate preparation thickness and edge geometry
Coating surface	Porosity and roughness match or improve the qualified baseline after finishing; spherical form remains within seal tolerance	Reprocess and repeat leakage-relevant surface characterization
Seat contact	Continuous sealing band in both pressure directions; Equation 4 satisfied; contact variation reduced relative to baseline	Adjust support stiffness, spring preload, seat profile or polymer grade
Polymer durability	Creep recovery and wear preserve sealing geometry after thermal and fluid aging	Reject filler level or redesign load path
Elastomer durability	Swelling, compression set elongation, and decompression damage remain within project compound limits	Return to neat FKM or change compound and cure system
Wax control	Deposit and removal force improve against a roughness-matched control after erosion exposure	Keep as exploratory and exclude from prototype

Gate	Progression criterion	Action if not met
Valve function	Bidirectional leakage complies with the specified standard; no progressive torque instability or damaging debris	Identify hydraulic contact or material cause before further cycling

8 Expected Scientific Contribution and Limitations

The proposed scientific contribution is the coupling of a hydraulic damage map with a bidirectional contact pressure map and a functionally zoned nanomaterial selection. Existing studies usually evaluate one coating, one polymer composite, or one valve geometry. The present framework makes the location of a material part of the hypothesis. It predicts that a thick dense carbide coating is more suitable for exposed metallic sealing and scraping zones, a low concentration nanocomposite is more suitable for a compliant primary seat, and a hydrated antiwax film is only credible on a protected noncontact zone. The framework can be falsified if the mapped damage does not coincide with observed failure, if the selected material worsens the counterface, or if valve leakage does not track contact pressure retention.

Several limitations are explicit. First, the literature data were generated on different substrates, fluids, loads, and specimen geometries; their numerical improvements cannot be converted directly into valve life. Second, the field viscosity data require unit confirmation, and the produced fluid particle distribution and water fraction are not yet defined. Third, nanoparticle health and handling controls must be included during compounding, spraying, machining, and waste collection. Fourth, large ball coating scale-up may introduce thickness gradients and residual stresses absent from coupons. Fifth, qualification of a modified seat compound or coating can require manufacturing process control beyond the laboratory formulation.

The design also involves trade-offs. A harder ball coating may increase PEEK wear; a stiffer graphene PEEK seat may reduce extrusion but increase leakage sensitivity to shape error; a lower friction surface may change the self-energizing behaviour of the seat; and a hydrophilic antiwax coating may increase corrosion risk at a defect. These interactions justify the evidence gate sequence and the retention of a conventional qualified baseline in every test campaign.

9 Conclusions

- The valve should be treated as a set of damage zones rather than as one material selection problem. Geometry and contact pressure remain the first design controls, while nanomaterials are used to protect the residual critical zones.
- A polished micro nano WC–10Co–4Cr coating applied by an optimized HVOF or fine feedstock HVAF route is the lead candidate for the ball sealing band and metallic scraper. Nitriding plus DLC and CrN or CrCN should be tested as alternative thin film systems, not automatically stacked over the carbide coating.
- Graphene nanoplatelet PEEK is the lead primary seat screening family, with hBN PEEK or WS_2 PEEK as controlled comparators. Selection must be based on creep recovery and valve leakage as well as friction and wear.
- Graphene-modified FKM is a credible secondary seal research candidate, but oil aging, compression set, dispersion, and rapid gas decompression performance must be established for the actual compound.
- The GO phytic acid antiwax film is exploratory and should be restricted to protected noncontact surfaces until its water fraction dependence, adhesion, and particle erosion durability are proven.
- The 89 mm field screening line and the DN500 PN100 structural valve are separate validation envelopes. The integrated CFD FEA coupon subcomponent and valve programme provides a defensible route from literature evidence to qualified construction without claiming unmeasured performance.

Declarations

Data availability: No new experimental dataset is reported in this design framework. The operating envelopes are project inputs and the cited numerical results remain attributable to the original publications.
Conflict of interest: The author declares no conflict of interest related to this manuscript.

References

[1] International Organization for Standardization. Oil and gas industries including lower carbon energy – Pipeline transportation systems – Pipeline valves. ISO 14313:2025. Geneva: ISO; 2025.
[2] American Petroleum Institute. Specification for valves. 25th ed. API Specification 6D. Washington (DC): American Petroleum Institute; 2021.
[3] LI Q, LI L, CHENG L, YU C, HAN C. Research on two-way sealing performance of fully welded large-caliber ball valve. Journal of Xihua University (Natural Science Edition). 2022 Nov 1;41(6):61-7.
[4] Ivancu LI, Popescu D. Investigation of the fluid flow in a large ball valve designed for natural gas pipelines. Applied Sciences. 2023 Mar 27;13(7):4247. https://doi.org/10.3390/app13074247
[5] Kang HL, Park HJ, Han SH. Investigation of the flow characteristics for cylinder-in-ball valve due to a change in the opening rate. Applied Sciences. 2022 Sep 6;12(18):8930. https://doi.org/10.3390/app12188930
[6] Zhang L, Deng Y, Liu Y, Liu X, Jiang X, Wu D, Wang Z. Failure analysis and wear-life prediction of a deep sea high-pressure ball valve under repeated opening-closing cycles. Engineering Failure Analysis. 2026 Jun 11:111114. https://doi.org/10.1016/j.engfailanal.2026.111114
[7] Burmaster D, Kainer A, Lu Y. Effects of surface roughness on wax deposition. Geoenergy Science and Engineering. 2023 Dec 1;231:212383. https://doi.org/10.1016/j.geoen.2023.212383
[8] Burmaster D, Chaudhry I, Lu Y. Experimental investigation of wax deposition on multiple steel alloys. Geoenergy Science and Engineering. 2024 Aug 1;239:212966. https://doi.org/10.1016/j.geoen.2024.212966
[9] Bobzin K, Heinemann H, Burbaum E, Schulz M. Development of near net shaped coatings for reduced postprocessing costs in valves. Journal of Thermal Spray Technology. 2023 Mar;32(2):681-92. https://doi.org/10.1007/s11666-023-01539-9
[10] Ding X, Cheng XD, Yuan CQ, Shi J, Ding ZX. Structure of micro-nano WC-10Co4Cr coating and cavitation erosion resistance in NaCl solution. Chinese Journal of Mechanical Engineering. 2017 Sep;30(5):1239-47. https://doi.org/10.1007/s10033-017-0162-9
[11] Hong S, Wu Y, Zhang J, Zheng Y, Qin Y, Lin J. Ultrasonic cavitation erosion of high-velocity oxygen-fuel (HVOF) sprayed near-nanostructured WC–10Co–4Cr coating in NaCl solution. Ultrasonics Sonochemistry.2015 Sep 1;26:87-92. https://doi.org/10.1016/j.ultsonch.2015.01.012
[12] Huang Y, Ding X, Yuan CQ, Yu ZK, Ding ZX. Slurry erosion behaviour and mechanism of HVOF sprayed micro-nano structured WC-CoCr coatings in NaCl medium. Tribology International. 2020 Aug 1;148:106315. https://doi.org/10.1016/j.triboint.2020.106315
[13] Cheng F, Jiang S. Cavitation erosion resistance of diamond-like carbon coating on stainless steel. Applied Surface Science. 2014 Feb 15;292:16-26. https://doi.org/10.1016/j.apsusc.2013.11.044
[14] Krella A, Marchewicz A. Effect of mechanical properties of CrN/CrCN coatings and uncoated 1.402 stainless steel on the evolution of degradation and surface roughness in cavitation erosion. Tribology International. 2023 Jan 1;177:107991. https://doi.org/10.1016/j.triboint.2022.107991
[15] Puértolas JA, Castro M, Morris JA, Ríos R, Ansón-Casaos A. Tribological and mechanical properties of graphene nanoplatelet/PEEK composites. Carbon. 2019 Jan 1;141:107-22. https://doi.org/10.1016/j.carbon.2018.09.036
[16] Kalin M, Zalaznik M, Novak S. Wear and friction behaviour of poly-ether-ether-ketone (PEEK) filled with graphene, WS2 and CNT nanoparticles. Wear. 2015 May 1;332:855-62. https://doi.org/10.1016/j.wear.2014.12.036
[17] Yang F, Li J, Han S, Ma N, Li Q, Liu D, Sui G. Wear resistant PEEK composites with great mechanical properties and high thermal conductivity synergized with carbon fibers and h-BN nanosheets. Polymers for Advanced Technologies. 2023 Jul;34(7):2224-34. https://doi.org/10.1002/pat.6043

[18] Liu M, Cataldi P, Young RJ, Papageorgiou DG, Kinloch IA. High-performance fluoroelastomer-graphene nanocomposites for advanced sealing applications. Composites Science and Technology. 2021 Jan 20;202:108592. https://doi.org/10.1016/j.compscitech.2020.108592
[19] Wei J, Jacob S, Qiu J. Graphene oxide-integrated high-temperature durable fluoroelastomer for petroleum oil sealing. Composites science and technology. 2014 Feb 24;92:126-33. https://doi.org/10.1016/j.compscitech.2013.12.010
[20] Tan SL, Von Lau E, Majumder M, Luo R, Wu G. Facile one-step functionalised graphene oxide-phytic acid coating towards effective wax inhibition in waxy oil transportation. Fuel. 2024 Dec 1;377:132829. https://doi.org/10.1016/j.fuel.2024.132829
[21] Standards Norway. NORSOK M-710:2014/AC:2019. Qualification of non-metallic materials and manufacturers – Polymers. Lysaker: Standards Norway; 2019.
[22] ASTM International. Standard test method for cavitation erosion using vibratory apparatus. ASTM G32-16(2021)e1. West Conshohocken (PA): ASTM International; 2021.
[23] ASTM International. Standard test method for erosion of solid materials by cavitating liquid jet. ASTM G134-17. West Conshohocken (PA): ASTM International; 2017.
[24] International Organization for Standardization. Industrial valves – Measurement, test and qualification procedures for fugitive emissions – Part 1: Classification system and qualification procedures for type testing of valves. ISO 15848-1:2015. Geneva: ISO; 2015.

Journal of Nanotechnology and Innovative Materials

Research Article

Conceptual Architecture of a Multi-Sensor Real-Time Monitoring System for Biomechanical Analysis of Intramuscular Injections

Elnare F.Firdus [1] and Atakishi T.Tarlan

[1] Department of Mechanics and Mathematics, School of Advanced Technologies and Innovation Engineering, Western Caspian University, Baku, Azerbaijan
[2]PhD student specializing in Medical Technology, Azerbaijan State Oil and Industry University,

Received: 20.08.2026 Accepted: 30.09.2026 Published: 12.10.2026
https://doi.org/10.54414/XFKW2059

Copyright: © 2026 by the authors. Licensee: Journal of Nanotechnology and Innovative Materials, Western Caspian University, Baku, Azerbaijan. This article is an open-access article distributed under the terms and conditions of the Creative Commons Attribution 4.0 International License (CC BY 4.0).

Abstract

This article presents the conceptual architecture of a multi-sensor, real-time monitoring system designed for the biomechanical assessment of the intramuscular (IM) injection technique. The proposed system utilizes an inertial measurement unit (IMU) to determine the needle's orientation in conjunction with a Time-of-Flight (ToF) distance sensor to estimate linear displacement. Sensor data are acquired by a central microcontroller and analyzed using geometric, filtering, and adaptive processing models. Letting θ denote the angle between the needle axis and the skin surface, the needle's penetration component perpendicular to the skin surface is defined as follows: $d = L \sin(\theta)$, where L represents the measured linear displacement of the needle. The calculated perpendicular penetration depth is interpreted relative to the effective tissue thickness. In this case, the penetration depth is indicated relative to the effective tissue thickness, which represents the distance from the skin surface to the beginning of the muscle layer. The proposed architecture comprises four functional layers: data acquisition, data processing and modeling, biomechanical analysis, and integrated assessment. The system is designed to quantitatively evaluate the needle insertion direction, penetration depth, trajectory stability, and temporal and velocity characteristics, as well as—when an additional spatial reference system is employed—anatomical topographic deviations. The research is conceptual in nature, and determining the system's actual measurement accuracy, reliability, and educational effectiveness requires the development of a physical prototype, calibration, and experimental validation.

Keywords: multi-sensor system; sensor fusion; real-time monitoring; biomechanical analysis; penetration model; intramuscular injection; objective skill assessment

1. Introduction

Intramuscular (IM) injection is a widely used procedure. Performing the procedure safely and effectively depends on the correct selection of the injection site, the length of the needle, the accuracy of the insertion angle, individual anatomical characteristics, and adherence to aseptic principles [1], [2], [3], [4],[5],[6].

Existing scientific literature highlights the importance of considering the injection site, needle length, subcutaneous tissue thickness, and the patient's anthropometric characteristics for the safe administration of intramuscular injections [3]. In particular, increased subcutaneous tissue thickness can prevent a standard-length needle from reaching the muscle layer, potentially resulting in the unintended deposition of the injection into the subcutaneous tissue [7].

In practical training, the assessment of injection technique is often based on observer feedback, checklists, and general performance indicators. While simulation-based medical training enables the repeated practice and structured assessment of a procedure in a safe environment, the real-time, quantitative monitoring of specific biomechanical parameters requires additional engineering solutions [8], [9], [10]. Objective assessment of technical skills demonstrates that reliability can be enhanced by evaluating measurable indicators during the performance of procedures, rather than relying solely on subjective observation [11]. In this context, the development of biomedical measurement systems capable of quantitatively recording the spatial and temporal parameters of needle manipulation is considered a promising engineering approach for the objective assessment of procedural skills.

Inertial sensors are widely used to assess motion and orientation. Combining data from gyroscopes, accelerometers, and—when necessary—magnetometers through sensor fusion enables the calculation of spatial orientation [12], [13]. Evaluating orientation data alongside parameters such as linear displacement, stability, penetration depth, and timing in penetration-based procedures—such as needle insertion—offers a promising approach for establishing objective training metrics. Measuring user movement and needle-tissue interaction within haptic and computer-aided needle insertion simulators demonstrates the technical potential of this field [14], [15]. Integrating IMUs and distance sensors into a unified measurement system can provide the technical foundation for the synchronous recording and subsequent digital processing of various biomechanical indicators of the procedure.

The aim of this study is to formulate the conceptual architecture, data flow, preliminary mathematical evaluation model, and future experimental validation framework for a multi-sensor biomedical measurement system—based on an IMU, a ToF distance sensor, and a microcontroller—designed to monitor the biomechanical indicators of IM injection technique in real time. The proposed system is intended for the quantitative assessment of the needle's spatial orientation, linear displacement, penetration depth, and movement stability, as well as the procedure's temporal parameters. The present work does not provide experimental results and should be regarded as an engineering framework for future stages of prototyping, calibration, and experimental validation.

2. Related Research and Problem Statement

International guidelines on injection safety establish a clinical-methodological framework for the proper selection of the injection site, adherence to aseptic practices, and the assurance of safety during the procedure [1], [2]. Furthermore, the scientific literature contains reviews and clinical recommendations that systematize various aspects of intramuscular (IM) injection techniques [3], [4], [5], [6]. These studies emphasize the importance of injection site selection, needle length, the patient's anatomical characteristics, and the injection technique itself.

However, the primary objective of these sources is not the real-time, sensor-based biomechanical monitoring of the injection procedure. Consequently, recording the needle's spatial orientation, linear displacement, movement stability, and procedural timing parameters within a unified biomedical measurement system remains a distinct engineering challenge.

Simulation technologies are widely used in medical education to create controlled and safe environments, facilitate repeated practice of procedures, and enable the structured assessment of skills [8], [9], [10]. Objective technical skill assessment systems demonstrate that it is possible to evaluate the performance of training participants using standardized criteria. Research on haptic technologies and needle-insertion simulation highlights the importance—for training systems—of measuring needle movement, user manipulations, and performance parameters during the procedure [14], [15].

The simultaneous recording and integration of various biomechanical parameters into a unified assessment model require the implementation of additional sensor and data-processing solutions.

Inertial measurement units and MARG sensor systems are widely used to determine motion and spatial orientation. For orientation calculation, quaternion-based extended Kalman filters and other sensor fusion methods enable the combination of data from accelerometers, gyroscopes, and—where necessary—magnetometers [12], [13].

In existing studies, the relationship p between tissue thickness and needle length is of particular importance. Increased subcutaneous tissue thickness can result in the needle failing to reach the muscle layer [7], [16], [17]. [18], [19], [20], [21]. Various imaging and anatomical studies of the gluteal and deltoid regions demonstrate the necessity of considering individual anatomical variability when selecting needle length [7], [16], [17], [18], [19], [20], [21].

In this context, the research gap is defined as follows: there is a need for a multisensor biomedical assessment architecture for IM injection training that integrates needle insertion angle, linear displacement, penetration depth, movement stability, and procedural timing metrics into a unified data stream; supports real-time monitoring; and allows for subsequent experimental validation.

3. Conceptual Methodology of the Research

The research is based on a conceptual engineering design approach. Key biomechanical variables targeted for assessment have been identified, and a functional data flow—following the sequence of sensing, processing, analysis, and output—has been established. To combine individual measurement metrics into a unified assessment indicator, a conceptual performance score model based on normalization and weighted integration has been proposed.

The primary input variables for the conceptual model include the needle's spatial orientation, linear displacement, penetration depth, movement stability, and temporal motion characteristics. These parameters are intended to be calculated using data obtained from IMU and ToF sensors.

To ensure measurement reliability, the following procedures must be carried out during the prototyping and experimental validation stages: sensor calibration, selection of sampling frequency, inter-sensor time synchronization, determination of filtering and sensor fusion parameters, and comparison of results with reference measurement methods.

Integrating a measurement or tracking mechanism into the system—one that establishes an additional spatial reference point—is required to assess the needle's deviation from the anatomical target. Therefore, in the current conceptual model, deviation from the anatomical target is treated not as a primary parameter measured directly, but as an additional assessment indicator envisaged for a future stage of the system's development.

Table 1. Functional comparison of the proposed conceptual system with existing approaches.

Criterion	Clinical standard approach	Traditional simulation	IMU-based measurement	Proposed system
Objective measurement	Limited	Limited/partial	Yes	Included
Real-time monitoring	Usually no	Platform-dependent	Yes	Included
Penetration/displacement	Clinical recommendation	Platform-dependent	Not directly	ToF-based measurement included
Orientation	Clinical recommendation	Platform-dependent	Yes	IMU-based assessment included
Stability	Not directly measured	Platform-dependent	Calculable	Assessment based on RMS/variation included
Multi-parameter integration	No	Platform-dependent	Usually limited	Composite score model proposed

The comparison presented in Table 1 reflects the intended engineering capabilities of the proposed system rather than its experimentally verified advantages.

4. Conceptual Architecture of the Multi-Sensor Monitoring System

4.1. System architecture

The proposed conceptual system architecture consists of four functional components:

I . Acquisition of raw data regarding the needle's spatial orientation, linear displacement, and temporal movement dynamics from IMU and ToF sensors;

II . Processing, calibration, and filtering of sensor data via a central microcontroller, along with the application of sensor fusion methods where necessary;

III . Calculation of the needle's orientation, linear displacement, penetration depth, movement stability, and temporal parameters based on the processed data. Assessment of positional deviation is possible only if an additional anatomical reference or tracking mechanism is integrated into the system;

IV Normalization of individual biomechanical parameters and their aggregation into a unified conceptual performance score based on a weighted integration model. The weights and decision boundaries of the scoring model are conceptual in nature at this stage, and their validity must be determined during the subsequent experimental validation phase.

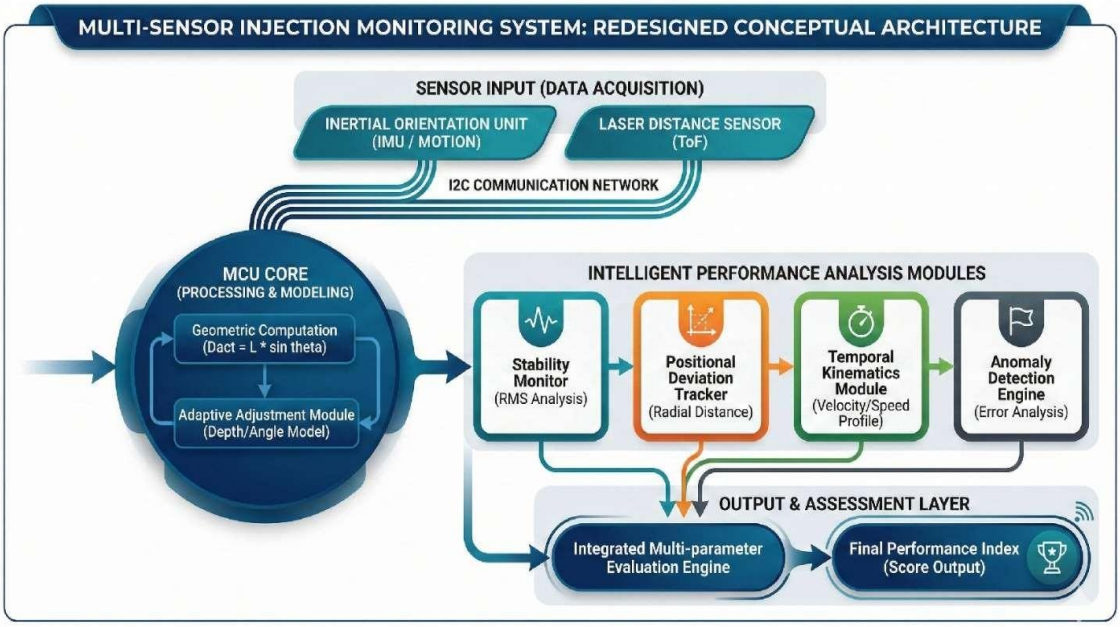


Figure 1. Conceptual diagram of a multi-sensor system for IM injection monitoring architecture and data flow.

4.1.1. Inertial measurement unit

The Inertial measurement unit is designed to evaluate the spatial orientation and movement dynamics of the needle. A three-axis gyroscope measures the needle's angular velocity along three coordinate axes, while a three-axis accelerometer measures the linear acceleration and specific force components. The joint processing of these data forms the basis for the assessment of needle motion characteristics and spatial orientation.

Accelerometer and gyroscope data are supposed to be combined through sensor fusion methods for a more stable and reliable assessment of orientation [12], [13]. Integration of magnetometer data, if necessary, can allow orientation estimation to be provided with additional information. The choice of specific IMU module, such as MPU6050 or BNO055, is not finalized at the current conceptual stage.

Sensor selection should be determined during the prototyping phase, taking into account measurement range, sampling frequency, measurement accuracy, calibration requirements, data interface, computing resource requirements, and the possibility of mechanical integration with the needle.

4.1.2. ToF displacement sensor and hardware interface

In the conceptual prototype, the application of the VL53L1X type Time-of-Flight distance sensor is considered for the evaluation of the linear displacement of the needle. The sensor supports the I²C digital communication interface and is designed by the manufacturer to perform measurements at different distance ranges [22].

It is methodologically incorrect to consider the measurement accuracy of the sensor as a constant value for all working conditions. Distance measurement error may depend on factors such as optical properties of the target surface, measurement distance, sensor configuration, measurement time, and ambient lighting [22].

Therefore, the actual measurement error, repeatability, and measurement stability of the VL53L1X sensor in the intended working distance range in the injection simulator should be determined experimentally during the prototyping stage. To assess the reliability of the sensor readings, the obtained distance should be compared with a suitable reference measurement system, and a calibration procedure should be performed.

The use of a microcontroller included in the STM32 family can be considered as the central data collection and processing unit of the system. Data acquisition from IMU and ToF sensors can be arranged through the I²C interface, depending on the technical capabilities of the sensors. SPI and other compatible digital communication interfaces can be used when high-speed data exchange, logging, and integration of additional peripherals are required. The selection of a specific microcontroller model is not finalized at the current conceptual stage.

Computational performance, sampling frequency, memory capacity, peripheral interfaces, power consumption, and data transfer rate should be taken into account during MCU selection [23].

4.2. Adaptive penetration model

Let the measured linear displacement of the needle be L, and the angle formed by the needle axis with the skin surface be denoted by θ. In this case, the displacement of the needle in the direction normal to the skin surface:

$$d = L \sin(\theta)$$

expressed in

the form Here:

d — needle insertion depth calculated perpendicular to the skin surface;

L — length of needle displacement beneath the skin; θ — angle between the needle's central axis and the skin surface.

The choice of angle and the direction of orientation are predetermined in the software, during calibration,

and in experimental protocols, and must be kept constant (Figure 2).

Studies have shown that the thickness of the skin and subcutaneous tissue influences the needle's

penetration into the muscle layer [7], [16], [17], [18], [19], [20], [21], [24]. Let skin thickness be denoted by

h_s, and subcutaneous tissue

thickness by $h_s c$. In the simplified model, the thickness of the tissue from the skin surface to the surface of

the muscle layer is calculated as follows:

$h_t = h_s + h_s c$ can be expressed a (Figure 2).

In this case, the initial geometric estimate:

$d \leq h_t$ — that the geometric limit to reach the muscle layer is not met, and when $d > h_t$ — it may indicate that the geometric limit has been exceeded to reach the muscle layer.

This approach is consistent with the relationship between subcutaneous tissue thickness and actual muscle reach reported in the literature [7], [16], [17], [18], [19], [20], [21].

However, this classification does not prove that the needle tip is in a safe and optimal position within the muscle. The model only evaluates whether the penetration component calculated in the direction normal to the skin surface exceeds a predefined tissue thickness threshold. The proposed threshold model is a conceptual mathematical approach for the preliminary quantitative estimation of the penetration index in the injection simulator.

In real-world application, skin and subcutaneous tissue thickness, tissue deformation, actual needle trajectory, muscle thickness, patient gender, body mass, body mass index, and individual anatomical variability should be taken into account [7], [16], [17], [18], [19], [20], [21]. The effective tissue thickness must be determined using a reliable external reference measurement method, and the proposed model must be experimentally validated by comparing it with reference measurements during the prototyping stage.

The geometry of the needle's insertion relative to the skin surface is shown in Figure 2. Here, L represents the measured linear displacement of the needle, θ the angle between the needle axis and the skin surface, d the component of the needle's displacement perpendicular to the skin surface, h_s is the skin thickness, h_sc is the subcutaneous muscle thickness, and h_t is the thickness of the properly transmitted tissue.

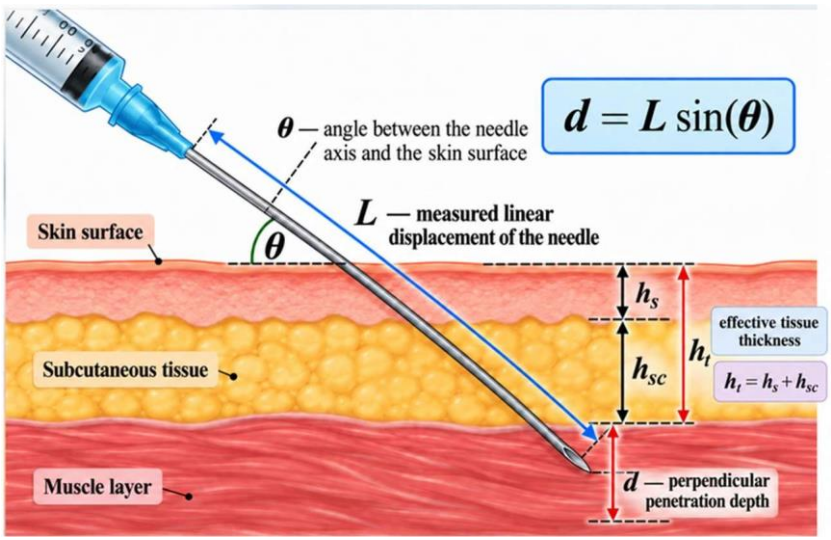


Figure 2. Needle insertion geometry, tissue thickness, and calculation of penetration depth perpendicular to the skin surface.

4.3. Anatomical-topographic and stability modules

The anatomo-topographic module is designed to quantitatively assess the position and deviation of the needle insertion point relative to a pre-defined target zone on the simulator. For this purpose, the radial distance of the insertion point from the target zone's reference point, or the positional difference within a two-dimensional or three-dimensional coordinate system, can be calculated.

Operation of the module requires the pre-definition and calibration of a local coordinate system, reference points, and target zone boundaries on the simulator. If the coordinates of the entry point are denoted as (x_i, y_i) and the coordinates of the target zone's reference point as (x_t, y_t), the expressions for calculating radial deviation in two-dimensional (1) and three-dimensional (2) coordinate systems are:

$$r = \sqrt{[(x_i - x_t)^2 + (y_i - y_t)^2]} \quad (1)$$

$$r = \sqrt{[(x_i - x_t)^2 + (y_i - y_t)^2 + (z_i - z_t)^2]} \quad (2)$$

Calculating this metric requires integrating an additional position-tracking or reference mechanism into the system to determine the coordinates of the entry point. An IMU and a one-dimensional ToF distance sensor alone are insufficient to fully determine these coordinates.

The stability module involves assessing the variation of the needle's selected orientation or position parameter relative to its average value over a specific time window. However, the specific orientation or position parameter, time window, and threshold values that provide the most informative data for assessing procedural stability must be determined during the experimental validation phase.

4.4. Time-dependent velocity module

The duration of needle insertion and withdrawal phases, the variation of linear displacement over time, movement speed, and velocity profile variability can be evaluated as additional biomechanical indicators characterizing the dynamic properties of the procedure. The obtained velocity profile can be used to characterize the duration of insertion and withdrawal phases, average and maximum speeds, and the temporal variability of movement speed.

The clinical and educational significance of the optimal target velocity range and the threshold values adopted for velocity profile assessment must be substantiated based on future experimental data.

4.5.Integrated assessment mechanism

To combine biomechanical indicators—which possess diverse physical units and measurement ranges—into a unified assessment score, the process involves first normalizing each parameter to a dimensionless 0–1 interval. Comparing the results obtained by combining biomechanical parameters into an integrated performance score with expert assessments and structured technical skill assessment methods can be used for construct validation [11].

5. Experimental Validation Plan

In the subsequent development phase of the proposed system, a physical prototype must be constructed, and the metrological characteristics of the sensor measurements must be experimentally determined. To validate linear displacement and angular measurements, pre-determined geometric positions, precision calibration devices, or suitable reference measurement systems may be employed.

Metrics such as mean error (bias), mean absolute error (MAE), root mean square error (RMSE), and Bland-Altman analysis can be used to evaluate the measurement between the sensor and the skin [25], [26]. Appropriate reliability indicators should be used to assess the reliability of repeated measurements, depending on the study design. Cronbach’s alpha, an indicator of internal consistency, should be applied only in cases where multiple items or indicators are theoretically and methodologically justified as components of the same latent construct.

Methodological approaches from existing haptic and computer-assisted needle insertion systems may be utilized when evaluating needle insertion and needle-tissue interaction under simulation conditions [14], [15]. The current work covers the conceptual engineering design phase, and no experimental studies involving human participants have been conducted. Therefore, the presented approaches should not be interpreted as results validating the system's clinical efficacy, diagnostic value, or actual measurement accuracy.

6. Limitations

The primary limitation of the study is that it is confined to the conceptual engineering design phase. Although the selection of sensor technologies and system architecture is justified based on existing technical specifications and intended measurement requirements, the current stage has not involved measurements on a physical prototype, experimental sample testing, comparative testing against a reference measurement system, or statistical validation.

Another significant limitation is that the conversion of the distance measured by the ToF sensor into the needle's actual axial displacement depends on the mechanical placement of the sensor and the geometry of the reference surface.

Finally, the target values for the proposed normalization functions, the acceptable deviation limits, and the weighting coefficients for the integrated performance score have not been experimentally determined at this stage. The scientific justification of these parameters and the constructive validation of the scoring model should be the subject of future prototyping and experimental research.

7. Conclusion

This study presents the conceptual architecture of a multi-sensor system designed for the multi-parameter biomechanical assessment and real-time monitoring of the intramuscular injection technique. The significant impact of the needle actually reaching the muscle layer has been extensively demonstrated in previous studies [7], [16], [17], [18], [19], [20], [21], [24]. Therefore, explicitly accounting for effective tissue thickness in the proposed penetration model is considered a key component of the biomechanical assessment. The proposed approach involves normalizing sensor and biomechanical indicators— which possess different physical units—and combining them into a conceptually integrated performance score.

A validation framework has been established to evaluate the system's measurement reliability; this framework encompasses sensor calibration, comparison with reference measurement systems, calculation of error metrics, and statistical assessment of intermethod agreement [25], [26]. The primary scientific outcome of this work is not a finished clinical device, an experimentally verified measurement system, or a validated performance metric, but rather a multi-sensor system model that can be physically realized and experimentally tested in subsequent stages.

Therefore, at this stage, no definitive conclusions are drawn regarding the system's measurement accuracy, reliability, or advantages in a training context. The next research phase envisages the development of a physical prototype, the calibration of IMU and ToF sensors, the comparison of linear displacement and orientation measurements against reference systems, the quantitative assessment of measurement errors and repeatability, and the analysis of inter-sensor time synchronization and system latency.

Author Contributions

All authors reviewed, edited, and approved the manuscript.

Conflict of Interest

The authors declare no conflicts of interest.

Funding

This research received no external funding

Acknowledgment

The authors declare no acknowledgments

References

[1] World Health Organization. WHO best practices for injections and related procedures toolkit. Geneva: World Health Organization; 2010. Report No.: WHO/EHT/10.02.

[2] Centers for Disease Control and Prevention. General best practices for immunization: vaccine administration [Internet]. Atlanta (GA): CDC; 2024

[3] Nicoll LH, Hesby A. Intramuscular injection: an integrative research review and guideline for evidence-based practice. Appl Nurs Res. 2002;15(3):149–162. https://doi.org/10.1053/apnr.2002.34142 , PMID:12173166.

[4] Cocoman A, Murray J. Intramuscular injections: a review of best practice for mental health nurses. J Psychiatr Ment Health Nurs. 2008;15(5):424–434. https://doi.org/10.1111/j.1365-2850.2007.01236.x , PMID:18454829.

[5] Wynaden D, Landsborough I, Chapman R, McGowan S, Lapsley J, Finn M. Establishing best practice guidelines for administration of intramuscular injections in the adult: a systematic review of the literature. Contemp Nurse. 2005;20(2):267–277. https://doi.org/10.5172/conu.20.2.267 , PMID:16393108.

[6] Ogston-Tuck S. Intramuscular injection technique: an evidence-based approach. Nurs Stand. 2014;29(4):52–59. https://doi.org/10.7748/ns.29.4.52.e9183 , PMID:25249123.

[7] Zaybak A, Yapucu Güneş Ü, Tamsel S, Khorshid L, Eşer I. Does obesity prevent the needle from reaching muscle in intramuscular injections? J Adv Nurs. 2007;58(6):552–556. https://doi.org/10.1111/j.1365-2648.2007.04264.x , PMID:17484745.

[8] Motola I, Devine LA, Chung HS, Sullivan JE, Issenberg SB. Simulation in healthcare education: a best evidence practical guide. AMEE Guide No. 82. Medical teacher. 2013 Oct 1;35(10):e1511-30. https://doi.org/10.3109/0142159x.2013.818632 , PMID:23941678.

[9] Lateef F. Simulation-based learning: Just like the real thing. Journal of emergencies, trauma and shock. 2010 Oct;3(4):348. https://doi.org/10.4103/0974-2700.70743 , PMID:21063557.

[10] Lioce L, Lopreiato J, Downing D, Chang TP, Robertson JM, Anderson M, Diaz DA, Spain AE, editors. Healthcare simulation dictionary. 2nd ed. Rockville (MD): Agency for Healthcare Research and Quality; 2020. AHRQ Publication No. 20-0019. https://doi.org/doi:10.23970/simulationv2.

[11] Tolsgaard MG, Ringsted C, Dreisler E, Klemmensen A, Loft A, Sorensen JL, Ottesen B, Tabor A. Reliable and valid assessment of ultrasound operator competence in obstetrics and gynecology. Ultrasound Obstet Gynecol. 2014;43(4):437–443. https://doi.org/10.1002/uog.13198 , PMID:23996613.

[12] Sabatini AM. Quaternion-based extended Kalman filter for determining orientation by inertial and magnetic sensing. IEEE transactions on Biomedical Engineering. 2006 Jul 31;53(7):1346-56. https://doi.org/10.1109/tbme.2006.875664 , PMID:16830938.

[13] Marins JL, Yun X, Bachmann ER, McGhee RB, Zyda MJ. An extended Kalman filter for quaternion-based orientation estimation using MARG sensors. In: Proceedings of the IEEE/RSJ International Conference on Intelligent Robots and Systems (IROS); 2001. p. 2003–2011. https://doi.org/10.1109/iros.2001.976367

[14] Coles TR, Meglan D, John NW. The role of haptics in medical training simulators: a survey of the state of the art. IEEE Trans Haptics. 2011;4(1):51–66. https://doi.org/10.1109/toh.2010.19

[15] Gerovich O, Marayong P, Okamura AM. The effect of visual and haptic feedback on computer-assisted needle insertion. Comput Aided Surg. 2004;9(6):243–249.

https://doi.org/10.1080/10929080500190441
[16] Burbridge BE. Computed tomographic measurement of gluteal subcutaneous fat thickness in reference to failure of gluteal intramuscular injections. Can Assoc Radiol J. 2007;58(2):72–75. PMID:17521050.
[17] Joo G, Sohng KY. Gluteal subcutaneous fat thickness measured by computed tomography as an estimate of proper gluteal intramuscular injections in Korean adults. J Korean Acad Nurs. 2010;40(2):247–254. https://doi.org/10.4040/jkan.2010.40.2.247 , PMID:20453571.
[18] Dayananda L, Belaval VV, Raina A, Chandana R. Intended intramuscular gluteal injections: are they truly intramuscular? J Postgrad Med. 2014;60(2):175–178. https://doi.org/10.4103/0022-3859.132334 , PMID:24823517.
[19] Elgellaie A, Ashcroft E, Larkin TA. Effects of thickness of muscle and subcutaneous fat on efficacy of gluteal intramuscular injection sites. Br J Nurs. 2018;27(6):300–305. https://doi.org/10.12968/bjon.2018.27.6.300 , PMID:29561673.
[20] Kim YS, Nam YS, Kim DI. Evaluating the effectiveness of gluteal intramuscular injection sites: a cadaveric study. Anat Cell Biol. 2022;55(1):48–54. https://doi.org/10.5115/acb.21.223 . PMID:35115416.
[21] Poland GA, Borrud A, Jacobson RM, McDermott K, Wollan PC, Brakke D, Charboneau JW. Determination of deltoid fat pad thickness: implications for needle length in adult immunization. JAMA. 1997;277(21):1709–1711. https://doi.org/10.1001/jama.1997.03540450065037 , PMID:9169899.
[22] STMicroelectronics. VL53L1X: a new generation, long distance ranging time-of-flight sensor based on ST's FlightSense technology [Internet]. Geneva: STMicroelectronics; 2024 Aug 29
[23] STMicroelectronics. STM32L47xxx, STM32L48xxx, STM32L49xxx and STM32L4Axxx advanced Arm-based 32-bit MCUs [Internet]. Geneva: STMicroelectronics; 2026 May 29
[24] Gulnar E, Ordu Y, Biyik Bayram S, Çalışkan N. Gluteal muscle and subcutaneous tissue thicknesses in adults: a systematic review and meta-analysis. J Res Nurs. 2023;28(3):181–196. https://doi.org/10.1177/17449871231155769 . PMID:37332320.
[25] Bland JM, Altman DG. Statistical methods for assessing agreement between two methods of clinical measurement. Lancet. 1986;1(8476):307–310. https://doi.org/10.1016/s0140-6736(86)90837-8 , PMID:2868172.
[26] Bland JM, Altman DG. Measuring agreement in method comparison studies. Stat Methods Med Res. 1999;8(2):135–160. https://doi.org/10.1191/096228099673819272 , PMID:10501650.

Journal of Nanotechnology and Innovative Materials

Research Article

Investigation of the Thermal and Dielectric Properties of $MnFe_2O_4$ Nanoparticles

Aynure F. Gochuyeva [1] ✉

[1]Department of Mechanics and Mathematics, School of Advanced Technologies and Innovation Engineering, Western Caspian University, Baku, Azerbaijan

Received: 27.06.2026 Accepted: 26.07.2026 Published: 12.10.2026
https://doi.org/10.54414/AUEG1934

Copyright: © 2026 by the authors. Licensee: Journal of Nanotechnology and Innovative Materials, Western Caspian University, Baku, Azerbaijan. This article is an open-access article distributed under the terms and conditions of the Creative Commons Attribution 4.0 International License (CC BY 4.0).

Abstract

This work investigates the thermal characteristics and dielectric response of manganese ferrite ($MnFe_2O_4$) nanoparticles under varying temperatures and γ-irradiation conditions. Commercial nanopowder with a nominal particle size of 60 nanometers and a stated purity of 98.5% was used. Differential scanning calorimetry (DSC) was employed to characterize the thermal response of the material within the temperature interval from −100 to 550 °C. In addition, temperature-dependent capacitance measurements were performed on pressed specimens to assess their dielectric response. The results obtained from untreated samples were subsequently evaluated against those recorded for specimens exposed to γ-radiation for different periods. The analysis considered the combined influence of temperature and irradiation exposure on the measured dielectric response. The observed variations may be associated with temperature-dependent polarization processes and changes in charge-carrier transport, while irradiation-related effects may influence localized electrical states within the material. The results contribute to the understanding of the thermal and dielectric characteristics of $MnFe_2O_4$ and may support further evaluation of its suitability for electronic components operating in environments involving temperature fluctuations and radiation exposure.

Keywords: $MnFe_2O_4$; manganese ferrite; nanoparticles; dielectric properties; electrical capacitance; differential scanning calorimetry (DSC); γ-irradiation

1. Introduction

$MnFe_2O_4$ is a ferrimagnetic material belonging to the spinel ferrite family whose thermal and electrical characteristics make it relevant to the study of functional materials. Its response to external conditions depends on several factors, including chemical composition, particle size, temperature, and exposure to ionizing radiation. Understanding these dependencies is important when evaluating the potential use of ferrite-based materials in electronic and dielectric components.

The electrical response of $MnFe_2O_4$ is related to charge transport and polarization processes within the material. Temperature variations can influence these processes by changing the mobility of charge carriers and the contribution of different polarization mechanisms. Consequently, measurable electrical parameters, including capacitance, may change with temperature. Investigating these variations can help clarify the dielectric response of manganese ferrite under different operating conditions.

Temperature-dependent dielectric measurements are particularly useful for assessing the suitability of materials for electronic applications. Measurements performed over a range of temperatures provide information that cannot be obtained from room-temperature data alone. Depending on the material and measurement conditions, thermal activation may influence charge transport, electrical conductivity, and polarization behavior. These effects should be considered when interpreting changes in the dielectric characteristics of ferrite-based systems [1], [2], [3].

Another factor that may affect the electrical response of ferrites is exposure to gamma radiation. The interaction of ionizing radiation with a solid can produce electronic excitations and, under appropriate conditions, radiation-induced defects or changes in localized charge states. Such processes may influence the electrical response of a material. However, the magnitude and direction of these changes depend on the composition of the sample, its initial condition, the absorbed radiation dose, and the irradiation conditions. Experimental comparison of irradiated and unirradiated specimens is therefore necessary to establish whether irradiation is associated with measurable changes in electrical capacitance.

Thermal analysis and electrical measurements provide complementary information about material behavior. Differential scanning calorimetry (DSC) makes it possible to examine heat-flow changes over a defined temperature interval, whereas capacitance measurements reveal variations in the electrical response under specified measurement conditions. Although these techniques investigate different physical characteristics, their combined use can provide a broader assessment of $MnFe_2O_4$. It is important, however, to distinguish the thermal behavior measured in nanopowder from the dielectric response of compacted specimens, because sample form and measurement method may influence the observed results.

In the present study, the thermal characteristics of commercial $MnFe_2O_4$ nanopowder were investigated by DSC over the temperature interval of −100 to 550 °C. Separately, the temperature dependence of electrical capacitance was examined using pressed $MnFe_2O_4$ specimens in their unirradiated state and after different periods of gamma irradiation. The study aims to characterize the thermal response of the nanopowder, compare the capacitance behavior of irradiated and unirradiated specimens, and evaluate the changes associated with temperature and irradiation duration. The results are intended to improve the understanding of the thermal and dielectric behavior of manganese ferrite under the investigated experimental conditions.

For this purpose, DSC analysis of the nanoparticles was performed, and the temperature dependence of electrical capacitance was comparatively investigated for unirradiated, 1 h γ-irradiated, and 10 h γ-irradiated samples [4], [5], [6], [7].

2. Experimental Procedure

Commercial manganese ferrite ($MnFe_2O_4$) nanopowder was used in this study. According to the manufacturer's specifications, the material had a nominal particle size of 60 nm and a purity of 98.5%. The powder was used directly for thermal analysis, while compact specimens were prepared for electrical capacitance measurements.

To obtain the specimens for dielectric measurements, the $MnFe_2O_4$ powder was placed in a specially designed mold and compressed to form pellets. The prepared specimens were subsequently used to investigate the temperature dependence of electrical capacitance and to compare the electrical response of unirradiated and γ-irradiated samples. The resulting pressed specimens were subsequently used for the temperature-dependent dielectric measurements. The resulting samples had dimensions of approximately 4 × 15 × 5 mm. Specimen compaction was performed with the aid of a hydraulic pressing system. The prepared samples were subsequently used for electrical measurements.

The thermal behavior of the nanoparticles was investigated using a DSC 204 F1 Phoenix differential scanning calorimeter. Measurements were performed over the temperature range of −100 to 550 °C. During DSC analysis, the response of the sample to temperature variation and the corresponding thermal effects were recorded. This method allows the characterization of thermal processes occurring in the material as a function of temperature.

To investigate the dielectric properties, the electrical capacitance of pressed $MnFe_2O_4$ samples was monitored at different temperatures. Three groups of samples were considered for comparison: an unirradiated sample, a sample irradiated with γ-rays for 1 h, and a sample a specimen exposed to γ-radiation for 1 h and another subjected to the same radiation for 10 h. The irradiation process was used to evaluate possible changes in the electrical parameters induced by γ-radiation.

3. Results and Discussion

3.1. Thermal Behavior of $MnFe_2O_4$ Nanoparticles

The DSC analysis of $MnFe_2O_4$ nanoparticles enabled the thermal behavior of the material to be evaluated over a wide temperature range. The selected temperature interval of −100 to 550 °C allowed thermal effects that may occur both in the low-temperature region and at higher temperatures to be observed.

In analyzing the DSC curve, changes in heat flow as a function of temperature were considered. Local variations observed in the curve may be associated with thermal processes occurring within the material. Changes observed in the low-temperature region may be related to the behavior of adsorbed components or weakly bound species under thermal influence. As the temperature rises, the measured response may additionally reflect variations in the material's energy states and physical transformations taking place within the solid.

The relatively high specific surface area of nanoparticles can increase the contribution of surface-related processes to their thermal behavior. As particle size decreases, the ratio of surface atoms and ions to the total number of atoms increases. Therefore, surface-related thermal processes in nanomaterials may have a different character compared with those in bulk materials.

Another important aspect of the DSC results is the evaluation of the thermal stability of $MnFe_2O_4$ nanoparticles. During practical applications, maintaining the physical properties of a material within a specific temperature range is an important requirement. The observed thermal behavior over the investigated temperature interval should therefore also be considered when interpreting the results of subsequent electrical measurements [4], [7], [8], [9].

It should be noted that it is not appropriate to associate every thermal effect observed in DSC measurements with a single process. The thermal behavior of nanomaterials may be determined by the combined effects of surface phenomena, adsorbed components, defects, and localized changes in the solid phase. Therefore, a more reliable interpretation can be obtained when DSC results are evaluated together with other physical measurements.

3.2. Temperature Dependence of Electrical Capacitance

The variation in capacitance with temperature provides important information about the dielectric characteristics of the investigated material. Measurements were performed for unirradiated and γ-irradiated samples to evaluate the effects of temperature and irradiation.

The thermal variation in capacitance in the unirradiated $MnFe_2O_4$ sample reflects changes in its dielectric response under different thermal conditions. With increasing temperature, charge carriers activated by thermal energy transport and the response of localized charge centers may affect the material's dielectric polarization characteristics. The extent and direction of the capacitance change depend on the relative contributions of these processes and the measurement conditions.

In manganese ferrite, the electrical response may also be associated with charge transfer between localized electronic states and the displacement or redistribution of charges under an applied electric field. Temperature-dependent changes in these processes can affect the effective dielectric properties of the sample. Similar mechanisms have been discussed in studies of ferrite materials. Nevertheless, the specific mechanism responsible for the observed capacitance variation should be established by considering the experimental data and, where available, complementary electrical measurements.

3.3. γ-Radiation-Induced Changes in the Electrical Capacitance

The influence of γ-irradiation on the electrical response of $MnFe_2O_4$ was examined by comparing the capacitance–temperature characteristics of unirradiated specimens with those irradiated for 1 h and 10 h. This comparison makes it possible to assess differences in capacitance associated with irradiation exposure under the investigated conditions.

Gamma radiation can interact with a ferrite material through energy transfer to its electronic system and may influence defect-related states and the distribution of localized charges. Depending on the absorbed dose and the initial condition of the specimen, these effects may modify charge transport and polarization processes,

thereby contributing to changes in electrical capacitance. However, the presence and relative importance of individual mechanisms cannot be established from capacitance measurements alone.

The comparison between the 1 h and 10 h irradiated specimens is particularly relevant for examining the relationship between irradiation duration and dielectric response. A longer exposure does not necessarily produce a proportional change in capacitance, because the response may depend on the absorbed dose, radiation-induced changes, and the characteristics of the material before irradiation. Therefore, the experimental capacitance values should be considered alongside the irradiation conditions when interpreting the observed differences.

The capacitance–temperature curves also provide information about how the electrical response of the specimens varies under thermal conditions following irradiation. Temperature may affect charge transport and polarization, while irradiation may modify the conditions under which these processes occur. Consequently, differences between the curves of unirradiated and irradiated samples should be interpreted in terms of their combined dependence on temperature and irradiation history [7].

Measurements over a range of temperatures offer a broader basis for comparing the dielectric response than measurements performed at a single temperature. In the present study, this approach was used to examine the electrical capacitance of $MnFe_2O_4$ specimens subjected to different irradiation durations. The results may help clarify the sensitivity of the material's electrical response to external influences and provide a basis for further investigation of its potential use in electronic components exposed to varying thermal and radiation conditions.

3.4. Correlation Between Thermal and Dielectric Results

DSC and electrical capacitance measurements provide complementary information about $MnFe_2O_4$, as they characterize different aspects of its physical behavior. DSC records heat-flow changes during temperature variation, whereas capacitance measurements describe the electrical response of the specimens under the applied measurement conditions. Considering these results together allows the thermal characteristics of the nanopowder to be discussed alongside the dielectric behavior of the compacted samples.

Temperature may influence several processes in ferrite materials, including thermally activated charge transport and polarization. However, the relationship between the DSC response and the measured capacitance should be interpreted cautiously, since the two techniques examine different physical quantities and the measurements were performed on samples in different physical forms.

Gamma irradiation provides an additional factor for evaluating the electrical response of $MnFe_2O_4$. Differences between unirradiated and irradiated specimens may reflect changes associated with radiation exposure, although capacitance data alone cannot identify the specific microscopic mechanisms responsible. Examining the temperature-dependent electrical response after different irradiation periods therefore provides a basis for assessing the sensitivity of the material to its thermal conditions and irradiation history.

Overall, the combined investigation of thermal and dielectric characteristics contributes to a more comprehensive assessment of $MnFe_2O_4$ under the experimental conditions considered. Additional investigations combining electrical measurements with complementary analytical techniques could clarify the underlying mechanisms of the physical processes contributing to the recorded effects and help establish potential technological uses of the investigated substance [8], [9].

4. **Conclusion**

The thermal and dielectric characteristics of $MnFe_2O_4$ were examined using differential scanning calorimetry and temperature-dependent electrical capacitance measurements. DSC analysis was performed across the investigated interval extending from −100 to 550 °C, while the electrical response of compacted specimens was evaluated for unirradiated samples and samples exposed to γ-radiation for 1 h and 10 h.

The capacitance measurements revealed a temperature-dependent electrical response, indicating that the dielectric behavior of $MnFe_2O_4$ varies under different thermal conditions. Differences between the unirradiated and irradiated specimens further demonstrated the sensitivity of electrical capacitance to irradiation history. These variations may be related to changes in charge transport and polarization, although further measurements are required to establish the underlying mechanisms.

The results provide experimental information on the thermal behavior of $MnFe_2O_4$ nanopowder and the dielectric response of compacted specimens. This information may serve as a basis for further investigations of manganese ferrite for applications involving variable temperatures and radiation exposure.

Author Contributions

All authors reviewed, edited, and approved the manuscript.

Conflict of Interest

The authors declare no conflicts of interest.

Funding

This research received no external funding.

Acknowledgment

The authors declare no acknowledgments.

References

[1] Akhlaghi N, Najafpour-Darzi G. Manganese ferrite (MnFe2O4) Nanoparticles: From synthesis to application-A review. Journal of Industrial and Engineering Chemistry. 2021 Nov 25;103:292-304. https://doi.org/10.1016/j.jiec.2021.07.043

[2] Simon C, Blösser A, Eckardt M, Kurz H, Weber B, Zobel M, Marschall R. Magnetic properties and structural analysis on spinel MnFe2O4 nanoparticles prepared via non-aqueous microwave synthesis. Zeitschrift für anorganische und allgemeine Chemie. 2021 Nov 25;647(22):2061-72. https://doi.org/10.1002/zaac.202100190

[3] Shehata MM, Waly SA, Farid O, Ghazy O, Ali ZI. Effect of γ-rays irradiation on structural and magnetic properties of Cd–Mn nanoferrites synthesized via sol-gel auto-combustion method. Radiation Physics and Chemistry. 2021 Jul 1;184:109429. https://doi.org/10.1016/j.radphyschem.2021.109429

[4] Lokhande RM, Vinayak V, Mukhamale SV, Khirade PP. Gamma radiation shielding characteristics of various spinel ferrite nanocrystals: a combined experimental and theoretical investigation. RSC advances. 2021 Feb 19;11(14):7925-37. https://doi.org/10.1039/d0ra08372k

[5] Srinivasamurthy KM, Manjunatha K, El-Denglawey A, Kubrin SP, Sarychev DA, Mašláň M, Pattar V. Dosimetry induced modifications in structural, magnetic and Mössbauer spectroscopy studies of 60Co γ-irradiated Co0. 5Ni0. 5Fe2O4. Radiation Physics and Chemistry. 2021 Dec 1;189:109781. https://doi.org/10.1016/j.radphyschem.2021.109781

[6] Gong L, Chen G, Lv J, Lu M, Zhang J, Wu X, Wang J. Phase transition-enabled MnFe2O4 nanoparticles modulated by high-pressure with enhanced electrical transport properties. Applied Surface Science. 2021 Nov 1;565:150532. https://doi.org/10.1016/j.apsusc.2021.150532

[7] Benabdellah A, Chaker Y, Fetouhi B, Debdab M, Belarbi EH, Hatti M. Sonochemical synthesis of MnFe2O4 nanoparticles with ionic liquid and their application in magnetic and dielectric polystyrene nanocomposites. International Journal of Materials Research. 2022 Mar 26;113(3):233-42. https://doi.org/10.1515/ijmr-2020-8142

[8] Agami WR. Monitoring the dielectric properties of Mn-ferrite nanoparticles by controlling crystallite size and applying static magnetic field. Ceramics International. 2022 May 15;48(10):13475-83. https://doi.org/10.1016/j.ceramint.2022.01.225

[9] Kumar S, Thakur N. Structural, dielectric, and magnetic properties of reduced graphene oxide-wrapped MnFe2O4 composites synthesized by in-situ sol-gel autocombustion method. Ceramics International. 2022 Feb 15;48(4):4444-55. https://doi.org/10.1016/j.ceramint.2021.10.138

Western Caspian University

Journal of Nanotechnology and Innovative Materials

Vol 2, No 2
October, 2026

Editorial Office Address: 17 A, Ahmad Rajabli Street,

III Parallel, Baku, Azerbaijan

Phone: +994 12 565 39 77

Email: jnim@wcu.edu.az

https://jnim.wcu.edu.az/

Submitted for collection: 12.10.2026

Signed for printing: 15.10.2026

Paper format: 60x84 1/16 17.75